

Eastern Illinois University

## The Keep

---

Masters Theses

Student Theses & Publications


---

Fall 2021

# Synthesis, Characterization and Photophysical Properties of Ytterbium Complexes of Functionalized Porphyrins and Porpholactone

Beibei Liu  
*Eastern Illinois University*

Follow this and additional works at: <https://thekeep.eiu.edu/theses>

 Part of the [Diagnosis Commons](#), and the [Inorganic Chemicals Commons](#)

---

### Recommended Citation

Liu, Beibei, "Synthesis, Characterization and Photophysical Properties of Ytterbium Complexes of Functionalized Porphyrins and Porpholactone" (2021). *Masters Theses*. 4915.  
<https://thekeep.eiu.edu/theses/4915>

This Dissertation/Thesis is brought to you for free and open access by the Student Theses & Publications at The Keep. It has been accepted for inclusion in Masters Theses by an authorized administrator of The Keep. For more information, please contact [tabruns@eiu.edu](mailto:tabruns@eiu.edu).

**Synthesis, Characterization and Photophysical  
Properties of Ytterbium Complexes of Functionalized  
Porphyrins and Porpholactone**

Beibei Liu

Research Advisor: Dr. Hongshan He

Eastern Illinois University

Chemistry and Biochemistry Department

Synthesis, characterization and photophysical properties of ytterbium complexes

of functionalized porphyrins and porpholactone

(TITLE)

BY

Beibei Liu

**THESIS**

SUBMITTED IN PARTIAL FULFILLMENT OF THE REQUIREMENTS  
FOR THE DEGREE OF

Master of Science in Chemistry

IN THE GRADUATE SCHOOL, EASTERN ILLINOIS UNIVERSITY  
CHARLESTON, ILLINOIS

2021

YEAR

I HEREBY RECOMMEND THAT THIS THESIS BE ACCEPTED AS FULFILLING  
THIS PART OF THE GRADUATE DEGREE CITED ABOVE

 12/17/2021  
\_\_\_\_\_  
THESIS COMMITTEE CHAIR                      DATE

Edward M Zecandwell 12/17/21  
\_\_\_\_\_  
DEPARTMENT/SCHOOL CHAIR                      DATE  
OR CHAIR'S DESIGNEE

 12/17/2021  
\_\_\_\_\_  
THESIS COMMITTEE MEMBER                      DATE

Edward M Zecandwell 12/17/21  
\_\_\_\_\_  
THESIS COMMITTEE MEMBER                      DATE

 12/17/2021  
\_\_\_\_\_  
THESIS COMMITTEE MEMBER                      DATE

\_\_\_\_\_  
THESIS COMMITTEE MEMBER                      DATE

# Table of Contents

<b>Table of Contents .....</b>	<b>i</b>
<b>Abstract.....</b>	<b>iii</b>
<b>Acknowledgements .....</b>	<b>iv</b>
<b>List of Figures.....</b>	<b>v</b>
<b>List of Schemes .....</b>	<b>viii</b>
<b>List of Tables .....</b>	<b>ix</b>
<b>Abbreviations .....</b>	<b>x</b>
<b>Chapter 1 Introduction.....</b>	<b>1</b>
<b>1.1 Overview .....</b>	<b>1</b>
<b>1.2 Fundamentals of porphyrins.....</b>	<b>3</b>
1.2.1 Physical and chemical properties of Porphyrins .....	3
1.2.2 Synthesis of porphyrins.....	4
<b>1.3 Functionalization of lanthanide porphyrin complexes .....</b>	<b>10</b>
1.3.1 Photophysical properties and applications of <i>meso</i> -position functionalized lanthanide porphyrin complexes.....	10
1.3.2 Photophysical properties and applications of $\beta$ -position functionalized lanthanide porphyrin complexes.....	27
1.3.3 Near-infrared emission properties of lanthanide porphyrin complexes.....	33
1.3.4 Comparison method for quantum yield calculation.....	35
<b>1.4 Applications of other metalloporphyrin complexes .....</b>	<b>37</b>
1.4.1 Applications in medical and biochemistry fields .....	37
1.4.2 Applications in catalysis .....	39
1.4.3 Applications in solar energy .....	43
<b>1.5 Motivation.....</b>	<b>46</b>
<b>1.6 Objective .....</b>	<b>47</b>
<b>Chapter 2 Experimental .....</b>	<b>48</b>
<b>2.1 General.....</b>	<b>48</b>
2.1.1 Materials .....	48
2.1.2 Instruments.....	49
<b>2.2 Synthesis.....</b>	<b>50</b>
2.2.1 Synthesis of DMPH <sub>2</sub> -BDP ligand and YbDMP-BDP complexes .....	50

2.2.1.1 Preparation of Br-DMPH <sub>2</sub> .....	51
2.2.1.2 Preparation of Br-YbDMP(OAc)(Sol) <sub>2</sub> .....	52
2.2.1.3 Preparation of Br-YbDMP(OAc)(Phen) .....	53
2.2.1.4 Synthesis of YbDMP-BDP .....	54
2.2.1.5 Synthesis of DMPH <sub>2</sub> -BDP .....	55
2.2.2 Synthesis of DMPH <sub>2</sub> -COOH ligand and YbDMP-COOH complexes .....	57
2.2.2.1 Synthesis of YbDMP-COOH.....	58
2.2.2.2 Synthesis of DMPH <sub>2</sub> -COOH .....	59
2.2.3 Synthesis of YbDMP as reference .....	60
2.2.4 Synthesis of TPLH <sub>2</sub> ligand.....	61
<b>2.3 Photophysical measurements .....</b>	<b>63</b>
2.3.1 Stock solutions .....	63
2.3.2 UV-Vis absorption spectra in solution.....	63
2.3.3 Fluorescence emission spectra in solution .....	64
2.3.4 Quantum yields .....	64
<b>Chapter 3 Results and Discussion .....</b>	<b>66</b>
<b>3.1 Characterization .....</b>	<b>66</b>
3.1.1 <sup>1</sup> H NMR spectroscopy.....	66
3.1.1.1 <sup>1</sup> H NMR for DMPH <sub>2</sub> -BDP .....	66
3.1.1.2 <sup>1</sup> H NMR for DMPH <sub>2</sub> -COOH .....	69
3.1.1.3 <sup>1</sup> H NMR for TPLH <sub>2</sub> .....	71
<b>3.2 Optimization of TPLH<sub>2</sub> reaction conditions .....</b>	<b>73</b>
<b>3.3 Photophysical properties .....</b>	<b>75</b>
3.3.1 Absorbance .....	75
3.3.2 Fluorescence emission .....	80
3.3.2.1 Fluorescence emission in visible region .....	80
3.3.2.2 Fluorescence emission in near-infrared region .....	82
3.3.3 Quantum yield measurements.....	84
<b>Chapter 4 Conclusion .....</b>	<b>95</b>
<b>References .....</b>	<b>96</b>

# Abstract

The unique structure and superior properties of lanthanide porphyrins enable them to be used in a broad variety of applications, especially in medical diagnosis fields. This research focuses on modifying the porphyrin ligands in various places, resulting in broader absorption in the red region and strong emission in the near-infrared region for these ytterbium(III) porphyrin complexes. The design, synthesis and characterization for DMPH<sub>2</sub>-BDP, DMPH<sub>2</sub>-COOH, TPLH<sub>2</sub> ligands and YbDMP-BDP, YbDMP-COOH complexes are described. The photophysical properties of these ligands and complexes including their absorbance, fluorescence and quantum yields are also presented. Both the synthesized ligands and complexes exhibit absorption peaks in the far-red region, indicating a novel strategy for the manufacture of lanthanide porphyrin photosensitive probes with red light excitation capability.

# Acknowledgements

I would like to express my gratitude to all professors who educate me and to peers who help me throughout my experience at EIU.

Most of all, I would like to express my sincere gratitude to my advisor Dr. Hongshan He. He is a rigorous and knowledgeable person with a broad vision and profound thoughts, all of which contribute to a positive academic environment for me and improve my studies significantly. I also thank Dr. He for his attentive guidance in the writing, and his advice plays a key role in the completion of the thesis.

I would also like to express my appreciation to Eastern Illinois University, specifically for the Chemistry and Biochemistry department. This is where I spend the majority of my time at school, and everything has a subtle effect on me. And thanks for all the help I received from the department stock room. In addition, I would like to express my sincere thanks to my thesis committee: Dr. Edward Treadwell, Dr. Radu Semeniuc and Dr. Zhiqing Yan for their assistance and guidance during the completion of my thesis and during the courses of my degree.

Finally, I would like to express my heartfelt gratitude to my father, Ningpu Liu, and my mother, Chengyu Bei, for their unwavering support, encouragement, and care throughout my life. As well as my friends, for their concern and camaraderie.

I hope that this thesis paper would not be the end of my academic thinking and that this previous sentence is not just a wishful talking.

# List of Figures

Figure 1.1. Structure of porphin.....	3
Figure 1.2. Alder-Longo method synthetic route.....	5
Figure 1.3. Lindsey method synthetic route.....	6
Figure 1.4. (a) [2+2] synthesis route and (b) [3+1] synthesis route.....	7
Figure 1.5. (a) Three different synthesis methods of ABAB- typed porphyrins; (b) Synthesis of ABCD- typed porphyrin. ....	8
Figure 1.6. Two-step methodology for synthesis of porphyrin. ....	9
Figure 1.7. (a) Reaction scheme of the formation of the Ln-THPP-Si hybrid materials; (b) Electronic absorption spectra of THPP(A), THPP-Si (B), Yb-THPP-Si (C) in DMF solutions. .	11
Figure 1.8. Normalized emission spectra for Ln-THPP-Si, (a) Ln = Nd and (b) Ln = Yb.....	12
Figure 1.9. The synthesis of phen-Ln-THPP-SBA-15 hybrids.....	13
Figure 1.10. Near-infrared emission spectra of (a) phen-Nd-THPP-SBA15 and (b) phen-Nd-PPIX- SBA15 hybrids.....	13
Figure 1.11. Near-infrared emission spectra of (a) phen-Yb-THPP-SBA15 and (b) phen-Yb-PPIX- SBA15 hybrids.....	14
Figure 1.12. Molecular structure of Yb-Rh complex.....	14
Figure 1.13. Emission spectrum of Yb-Rh. ....	15
Figure 1.14. Molecular structure of Yb-N complex and Lig-N and Yb-Rh as the controls. ....	16
Figure 1.15. The in vitro imaging, emission spectra of Yb-N/Lig-N/Yb-Rh in human lung tumor cells HeLa and human normal prostate cells WPMY-1.....	17
Figure 1.16. In vivo tumor inhibition assays of Gd-N.....	18
Figure 1.17. Molecular structures of YbPor-SS and YbPor-L complexes. ....	19
Figure 1.18. (a) Absorption spectra of YbPor-SS and YbPor-L in CH <sub>3</sub> CN/HEPES buffer; (b) Visible and near-infrared emission spectra of YbPor-SS and YbPor-L in CH <sub>3</sub> CN/HEPES buffer. ....	20
Figure 1.19. (a) Changes in absorption spectra of YbPor-L in CH <sub>3</sub> CN/HEPES buffer upon addition of Hg <sup>2+</sup> . Inset: Job's plot between YbPor-L and Hg <sup>2+</sup> ; (b) Dual emission spectra of YbPor-L in CH <sub>3</sub> CN/HEPES buffer upon addition of Hg <sup>2+</sup> ion. ....	21



Figure 1.20. (a) Molecular structures of the Ln(III) complexes; (b) Emission spectra of the ytterbium complexes with various degrees of C-H bond replacement under the same conditions. ....	22
Figure 1.21. Synthesis routes of <i>meso</i> -modification Yb(III) complexes. ....	23
Figure 1.22. Synthetic procedures of the lanthanide complexes. ....	24
Figure 1.23. Fluorescence emission spectra of F-Yb in pH 5.0-9.0 PBS buffer. ....	24
Figure 1.24. Molecular structures of porphyrin-based Yb(III) complexes conjugated to co-photosensitizers BODIPY and bis(BODIPY)phenanthroline. ....	25
Figure 1.25. (a) Absorption spectra of BDP-Phen and Yb(III) complexes in DCM at room temperature; (b) The near-infrared emission spectra of Yb(TPP)(OAc)(BDP-Phen) under various excitation wavelengths. ....	26
Figure 1.26. Molecular structures of (a) LD14, (b) LD31 and (c) AN-4. ....	26
Figure 1.27. Near-infrared emission spectra of Glycosylated ytterbium porpholactone at various concentrations of GOx in Tris·HCl buffer. ....	28
Figure 1.28. Schematic diagram of adjusting the porphyrinic T <sub>1</sub> energy state of porphyrin by changing the number and orientation alteration of $\beta$ -substituent. ....	29
Figure 1.29. Chemistry structures of Yb-up and Yb-down. ....	29
Figure 1.30. (a) Normalized absorption spectra of Yb-up/down; (b) Emission intensities of Yb-up and Yb-down. ....	30
Figure 1.31. Schematic diagram of energy dissipation pathways in Ln complexes and photoacoustic imaging-guided photothermal/photodynamic synergy therapy. ....	31
Figure 1.32. Infrared thermographs of the mice under laser irradiation in the control and YbL@MSN groups. ....	32
Figure 1.33. Three paths to lanthanide fluorescence emission. ....	34
Figure 1.34. Schematic structure of surface-modified UiO-66-TPP-SH and one-pot method TCPP & UiO-66. ....	38
Figure 1.35. Schematic illustration of the study rationale and design. ....	38
Figure 1.36. Synthesis of Hf-DBP NMOF and the schematic description of singlet oxygen generation process. ....	39
Figure 1.37. Schematic description of singlet oxygen generation by DBC-UiO photosensitization with LED light. ....	39
Figure 1.38. Schematic diagram of copper porphyrin electrocatalytic water oxidation. ....	40
Figure 1.39. Schematic diagram of Au electrode surface model system construction. ....	41

Figure 1.40. Molecular structures of symmetrical and unsymmetrical dinuclear cobalt porphyrins. ....	42
Figure 2.1. Preparation of Br-DMPH <sub>2</sub> . ....	51
Figure 2.2. Preparation Br-YbDMP(OAc)(Sol) <sub>2</sub> . ....	52
Figure 2.3. Preparation of Br-YbDMP(OAc)(Phen).....	53
Figure 2.4. Synthesis of YbDMP-BDP.....	54
Figure 2.5. Synthesis of DMPH <sub>2</sub> -BDP. ....	55
Figure 2.6. Synthesis of YbDMP-COOH. ....	58
Figure 2.7. Synthesis of DMPH <sub>2</sub> -COOH.....	59
Figure 2.8. Synthesis of YbDMP.....	60
Figure. 2.9. Synthesis of TPLH <sub>2</sub> . ....	61
Figure 3.1. <sup>1</sup> H NMR spectrum for DMPH <sub>2</sub> -BDP. ....	68
Figure 3.2. <sup>1</sup> H NMR spectrum for DMPH <sub>2</sub> -COOH.....	70
Figure 3.3. <sup>1</sup> H NMR spectrum for TPLH <sub>2</sub> . ....	72
Figure 3.4. Absorption spectra of DMPH <sub>2</sub> -BDP ligand and YbDMP-BDP complex. ....	75
Figure 3.5. Absorption spectra of DMPH <sub>2</sub> -COOH ligand and YbDMP-COOH complex. ....	76
Figure 3.6. Absorption spectra of YbDMP-BDP, YbDMP-COOH and YbDMP complexes. ....	78
Figure 3.7. Absorption spectra of DMPH <sub>2</sub> -COOH and DMPH <sub>2</sub> -BDP ligands.....	79
Figure 3.8. Absorption spectra of TPLH <sub>2</sub> and TPPH <sub>2</sub> ligands.....	80
Figure 3.9. (a) Emission spectra for DMPH <sub>2</sub> -BDP and YbDMP-BDP; (b) Emission spectra for DMPH <sub>2</sub> -COOH and YbDMP-COOH.....	81
Figure 3.10. Emission spectra of TPLH <sub>2</sub> and TPPH <sub>2</sub> . ....	82
Figure 3.11. (a) Emission spectra of YbDMP-BDP; (b) Emission spectra of YbDMP-COOH; excited at various wavelengths. ....	83
Figure 3.12. Jablonski diagram for YbDMP-BDP and YbDMP-COOH complexes. ....	84
Figure 3.13. (a) Absorption spectra for TPPH <sub>2</sub> with gradient concentrations; (b) Emission spectra for TPPH <sub>2</sub> with gradient concentrations. ....	86
Figure 3.14. Integrated fluorescence vs. absorbance graph for TPPH <sub>2</sub> quantum yield determination. ....	87
Figure 3.15. (a) Absorption spectra for DMPH <sub>2</sub> -BDP with gradient concentrations; (b) Emission spectra for DMPH <sub>2</sub> -BDP with gradient concentrations. ....	87

Figure 3.16. Integrated fluorescence vs. absorbance graph for DMPH <sub>2</sub> -BDP quantum yield determination. ....	88
Figure 3.17. (a) Absorption spectra for TPLH <sub>2</sub> with gradient concentrations; (b) Emission spectra for TPLH <sub>2</sub> with gradient concentrations. ....	88
Figure 3.18. Integrated fluorescence vs. absorbance graph for TPLH <sub>2</sub> quantum yield determination. ....	89
Figure 3.19. (a) Absorption spectra for TPPH <sub>2</sub> with gradient concentrations; (b) Emission spectra for TPPH <sub>2</sub> with gradient concentrations. ....	90
Figure 3.20. Integrated fluorescence vs. absorbance graph for TPPH <sub>2</sub> quantum yield determination. ....	90
Figure 3.21. (a) Absorption spectra for DMPH <sub>2</sub> -COOH with gradient concentrations; (b) Emission spectra for DMPH <sub>2</sub> -COOH with gradient concentrations.....	91
Figure 3.22. Integrated fluorescence vs. absorbance graph for TPPH <sub>2</sub> quantum yield determination. ....	92
Figure 3.23. (a) Absorption spectra for YbTPPTpH with gradient concentrations; (b) Emission spectra for YbTPPTpH with gradient concentrations. ....	92
Figure 3.24. Integrated fluorescence vs. absorbance graph for YbTPPTpH quantum yield determination. ....	93
Figure 3.25. (a) Absorption spectra for YbDMP-BDP with gradient concentrations; (b) Emission spectra for YbDMP-BDP with gradient concentrations. ....	93
Figure 3.26. Integrated fluorescence vs. absorbance graph for YbDMP-BDP quantum yield determination. ....	94

## List of Schemes

Scheme 2.1 Synthetic route for DMPH <sub>2</sub> -BDP ligand and YbDMP-BDP complex.....	50
Scheme 2.2. Synthetic route for DMPH <sub>2</sub> -COOH ligand and YbDMP-COOH complex.....	57

## List of Tables

Table 2.1. Summary of chemicals used in preparation of Br-DMPH <sub>2</sub> .	51
Table 2.2. Summary of chemicals used in preparation of Br-YbDMP(OAc)(Sol) <sub>2</sub> .	52
Table 2.3. Summary of chemicals used in preparation of Br-YbDMP(OAc)(Phen).	53
Table 2.4. Summary of chemicals used in preparation of YbDMP-BDP.	54
Table 2.5. Summary of chemicals used in preparation of DMPH <sub>2</sub> -BDP.	55
Table 2.6. Summary of chemicals used in preparation of YbDMP-COOH.	58
Table 2.7. Summary of chemicals used in preparation of DMPH <sub>2</sub> -COOH.	59
Table 2.8. Summary of chemicals used in preparation of YbDMP.	60
Table 2.9. Summary of chemicals used in preparation of TPLH <sub>2</sub> .	61
Table 2.10. Concentrations of stock solutions.	63
Table 2.11. Concentrations of solutions prepared for absorption.	64
Table 3.1. Controlled experiments for TPLH <sub>2</sub> synthesis.	73
Table 3.2. Absorbance and integrated fluorescence of TPPH <sub>2</sub> with gradient concentrations.	86
Table 3.3. Absorbance and integrated fluorescence of DMPH <sub>2</sub> -BDP with gradient concentrations.	87
Table 3.4. Absorbance and integrated fluorescence of TPLH <sub>2</sub> with gradient concentrations.	89
Table 3.5. Absorbance and integrated fluorescence of TPPH <sub>2</sub> with gradient concentrations.	90
Table 3.6. Absorbance and integrated fluorescence of DMPH <sub>2</sub> -COOH with gradient concentrations.	91
Table 3.7. Absorbance and integrated fluorescence of YbTPPTpH with gradient concentrations.	92
Table 3.8. Absorbance and integrated fluorescence of YbDMP-BDP with gradient concentrations.	94

# Abbreviations

1. DCM – dichloromethane
2. DCE – 1,2-dichloroethane
3.  $\text{CDCl}_3$  – chloroform-d
4. DMSO – dimethyl sulfoxide- $\text{d}_6$
5. NMR – nuclear magnetic resonance
6. NIR – near-infrared
7. Ln – lanthanide
8.  $\text{Yb}(\text{OAc})$  – ytterbium (III) acetate
9. Por – porphyrin
10.  $\text{DMPH}_2$  – 5,15-dimesitylporphyrin
11.  $\text{Br-DMPH}_2$  – 5-bromo-10,20-dimesitylporphyrin
12. BDP – 8-(4-ethynylphenyl)-1,3,5,7-tetramethyl-BODIPY
13.  $\text{TPPH}_2$  – 5,10,15,20-tetraphenylporphyrin
14.  $\text{TPLH}_2$  – 5,10,15,20-tetraphenylporpholactone
15. NBS – N-Bromosuccinimide
16.  $\text{Pd}(\text{PPh}_3)_4$  – tetrakis(triphenylphosphine)palladium
17. Oxone® – potassium peroxymonosulfate
18. PE – petroleum ether

# Chapter 1 Introduction

## 1.1 Overview

Fluorescence emission is widely used in imaging for chemistry and biochemistry research. Compared with traditional visible emission from organic probes, the near-infrared (NIR) emission is advantageous in two ways. It has a higher signal-to-noise ratio because of low NIR emission from biological substrates. Meanwhile, the low absorbance of NIR light by biological tissues allows greater penetration and deeper imaging.<sup>1</sup>

One family of promising candidates for NIR emission are lanthanide ions (e.g.  $\text{Yb}^{3+}$ ,  $\text{Er}^{3+}$ ,  $\text{Nd}^{3+}$ ) because their complexes have relatively strong NIR emission, thermal stability and are easy to prepare. Among them,  $\text{Yb}^{3+}$  plays a leading role in lanthanide sensitization.<sup>2,3</sup> However, the lanthanide ions have low absorption coefficients and thus require sensitization using particular chromophores or a coherent light source in order to improve their fluorescence characteristics.<sup>2</sup> Among many chromophores, the porphyrins have excellent lanthanide chelating capacity, and changeable trilinear state that match of the lanthanide ions.<sup>4</sup> Also, porphyrins have high extinction coefficients, which allow for more effective absorption of excitation light.<sup>5</sup> These characteristics enable porphyrin ligands having a superior ability to sensitize lanthanide ions and produce greater NIR emission. Additionally, porphyrins could be modified on several positions to achieve different purposes, including enabling multi-wavelength excitation and improving solubility. For instance, acetylacetonation on the  $\beta$ - position of inner ring of porphyrin led to porpholactone with red-shifted excitation wavelength above 600 nm and increased NIR emission efficiency by 50% - 120% in their complexes.<sup>6</sup>

In view of the growing significance of ytterbium porphyrin complexes in NIR fluorescence emission, this chapter summarizes the photophysical properties of lanthanide functionalized porphyrin and porpholactone complexes in NIR region. Based on this understanding, the major part of this chapter is also devoted to highlighting design, synthesis and modification of porphyrin derivatives and their lanthanide complexes with a special focus on the bioanalytical sensing and imaging applications.

## 1.2 Fundamentals of porphyrins

### 1.2.1 Physical and chemical properties of Porphyrins

The strong light absorption and the adjustability of the excitation wavelength of porphyrins are closely tied with their conjugate structures. Porphyrins are a type of skeletal macrocyclic compounds composed of four pyrrole rings that are connected through methene groups. The core structure of porphyrins is porphin, a highly conjugated heterocyclic molecule with 26 electrons that is often referred to as the porphyrin parent. The structure of porphin is shown in Figure 1.1. Further modifications of porphin are realized by the substitution of hydrogen atoms at eight  $\beta$ - and four *meso*-positions of the four pyrrole rings in the molecular structure, producing a variety of porphyrin derivatives. By convention, positions 2, 3, 7, 8, 12, 13, 17, and 18 are the  $\beta$ - carbons; and positions 5, 10, 15, and 20 refer to *meso*- carbons (details are shown in Figure 1.1).<sup>7,8</sup>

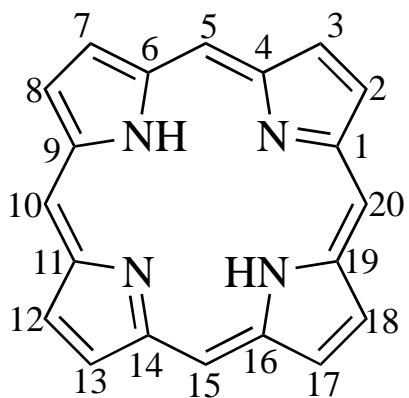


Figure 1.1. Structure of porphin.<sup>7,8</sup>

The modifications of the porphin structure alter the solubility of the resultant porphyrin in water, which is critical for biological applications. Solubility in water and other hydrophilic solvents (e.g. methanol, acetone, acetonitrile, etc.) could be realized by including functional groups like sulfolane, ammonium, and carboxyl groups. On the other hand, tetraphenylporphyrin,



tetra-p-chlorophenylporphyrin, etc., are generally soluble in benzene, dichloromethane, pyridine, N, N-Dimethylformamide (DMF) and other hydrophobic solvents.

Structurally, the porphyrins contain four lone pairs of electrons on the four nitrogen atoms. Two hydrogen atoms on the inner amine groups are easily lost to generate divalent anions. They could easily coordinate to positively charged metal ions to form metal complexes. The metal ions of this kind that have been described include  $\text{Zn}^{2+}$ ,  $\text{Cu}^{2+}$ ,  $\text{Ni}^{2+}$ ,  $\text{Fe}^{2+}$ ,  $\text{Pd}^{2+}$ ,  $\text{Pt}^{2+}$ ,  $\text{Rh}^{3+}$ ,  $\text{Sn}^{4+}$ , and  $\text{Co}^{4+}$ , as well as a few lanthanide ions.<sup>9,10,11,12,13,14,15</sup> Abundant metalloporphyrin complexes exist in nature. For example, heme a, heme b, heme c and cytochrome are coordinated by porphyrin and iron, as well as chlorophyll a and chlorophyll b coordinated by porphyrin and magnesium. They are all metal complexes of porphyrins and play an irreplaceable role in the metabolism of organisms.

### 1.2.2 Synthesis of porphyrins

The first artificial synthesis of porphyrin was achieved by Pual Rothmund in 1936 by refluxing benzaldehyde and pyrrole at 150 °C for 24-48 h.<sup>16</sup> However, this method is low in yield and could only be applied to a restricted number of benzaldehyde compounds, which restrain its applicability. Since then, porphyrins have been synthesized through two main classical methods: the Adler synthesis and Lindsey synthesis.<sup>17, 18</sup> The majority of contemporary synthetic methods have been improved and developed upon these two methods.<sup>19</sup>

Alan Adler et al., based on Rothmund's work, synthesized tetraphenylporphyrin (TPPH<sub>2</sub>) in 1967 by refluxing benzaldehyde and pyrrole in propionic acid at 141 °C for 30 min under air.<sup>20</sup> The synthetic pathway is shown in Figure 1.2. The benzaldehyde could be replaced by benzaldehyde with different substituents, resulting in the synthesis of various TPP substituents with yields of about 10-30%. The main advantages of this synthesis method are the simplicity of

operation, moderate conditions and the possibility of preparing large quantities at higher concentrations. According to the benzaldehyde's variable substituents, it could be utilized to synthesize a variety of functional porphyrins. Even with an ideal synthesis process, there are still drawbacks, such as the difficult by-products separation and the inability to use acid-sensitive benzaldehyde analogs as reactant.

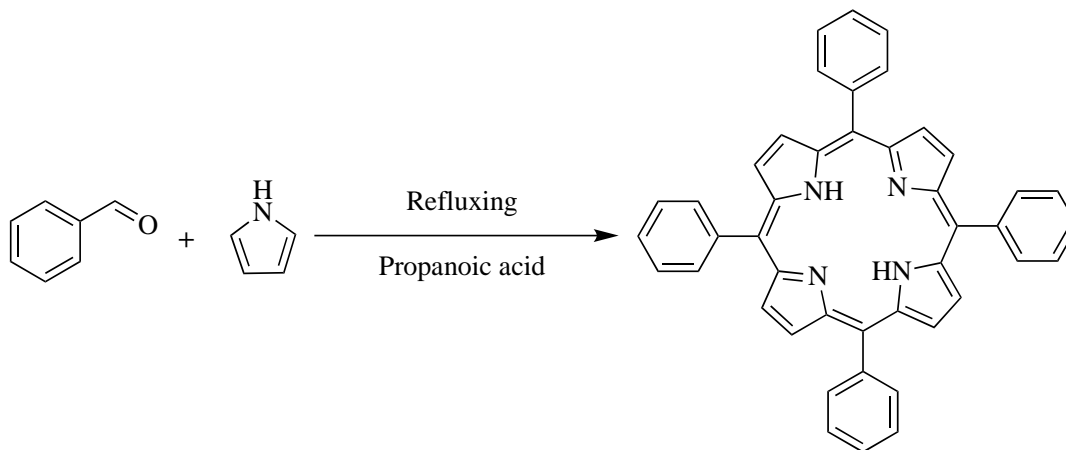


Figure 1.2. Alder-Longo method synthetic route.

Later, Jonathan Lindsey and his collaborators developed a novel method for the production of porphyrins in 1986. The reaction is carried out by adding equimolar quantities of benzaldehyde and pyrrole to re-distilled dichloromethane under a nitrogen atmosphere, with trifluoroacetic acid (TFA) serving as a catalyst. The solution turns red at room temperature, indicating the formation of porphyrinogen (this reaction was reversible),<sup>21</sup> and Figure 1.3 illustrates the synthetic approach. The yield of this synthesis method could reach 30-40%. Purification is straightforward, and acid-sensitive benzaldehydes could be utilized as reactant as well. The disadvantages are that it could only be prepared in dilute solution, is strictly oxygen-free and water-free environment, required lengthy reaction steps and is not easy to prepare in large quantities.

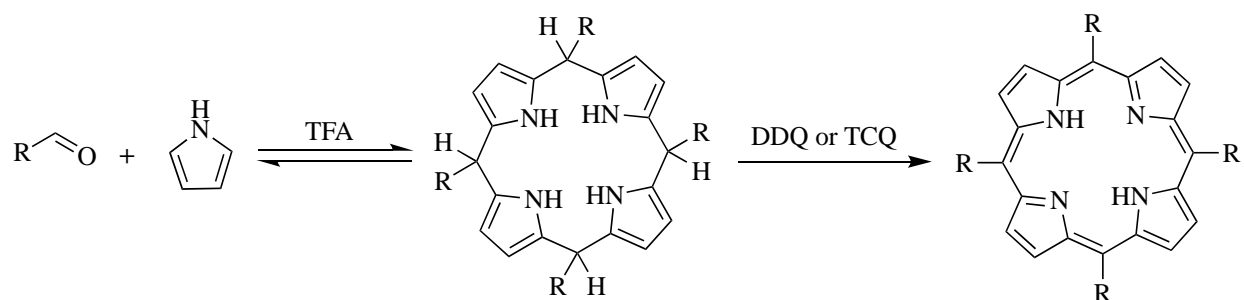


Figure 1.3. Lindsey method synthetic route.

Both Alder et al. and Lindsey et al. obtained porphyrins by mixed condensation synthesis. Mixed condensation is simply a reaction in which aldehydes, pyrroles, catalysts and oxidants are condensed together under certain conditions. The advantage of this method is that the reaction steps are straightforward and easy to perform. However, because aldehydes and pyrroles are condensed into a ring by free combination without target, there are three major drawbacks to this method: low yields of typically between 10-30%, requirement of tedious column chromatography to separate and purify the products, and strict nitrogen protection against oxidation.

Researchers have continuously reported new methods to overcome the aforementioned drawbacks. To relieve the requirement on environmental condition, Cancheng Guo et al. used DMF instead of propionic acid as the solvent and anhydrous  $\text{AlCl}_3$  as the catalyst to achieve a highest yield about 30% without by-product tetraphenyldihydroporphyrin.<sup>22</sup> A balance between lenient requirements on reaction conditions and yields was later realized by the same group using propionic acid and DMSO as mixed solvents at reflux for 2 h and oxygen as oxidant, producing another series of porphyrins with yields greater than 30%.<sup>23</sup> Similarly, Qinbo Wang et al. used mixed solvents containing propionic acid and one or more of benzene, toluene, p-xylene, or cyclohexane, the synthesized porphyrins in yields ranging from 26% to 37%.<sup>24</sup>

Porphyrins with a completely symmetrical molecular structure are formed by the condensation and oxidation of pyrrole without substituents at the corresponding 2,5 positions with formaldehyde (or benzaldehyde). Or the symmetrical porphyrins are generated by self-condensation and oxidation of pyrroles having a methyl (or methylene) at the 2-position (the methyl at the 2-position was employed to generate hypomethyl bridges)<sup>25</sup>. In the case of porphyrins with asymmetric molecular structure, each substituted pyrrole is synthesized separately and then progressively connected into rings.<sup>26</sup> Those methods could be classified as [2+2] and [3+1] synthesis, based on the sequence of the linked rings and intermediates utilized throughout the synthesis process, as pictured in Figure 1.4.

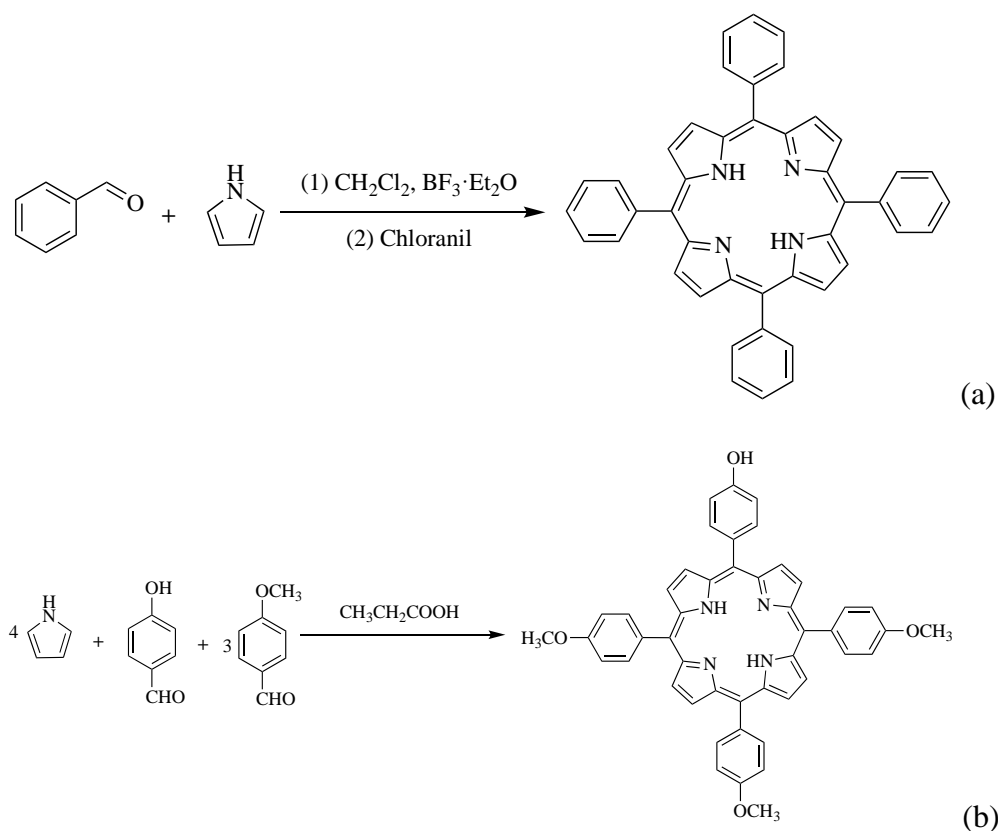


Figure 1.4. (a) [2+2] synthesis route and (b) [3+1] synthesis route.

The total synthesis method refers to the stepwise synthesis of target porphyrins by employing pyrrole and aldehyde as reactants. There are four primary approaches for total

synthesis of asymmetric *meso*-substituted porphyrins. As shown in Figure 1.5(a), the ABAB-typed porphyrins are synthesized in three methods, as follows. First, they are synthesized by condensation of 1:1 molar ratio dipyrromethane with A- functional group and aldehyde with B- functional group, with dichloromethane as solvent, trifluoroacetic acid (TFA) as catalyst, and 2,3-dichloro-5,6-dicyano-1,4-benzoquinone (DDQ) as oxidant.<sup>27</sup> Second, they are synthesized by self-condensation of AB- 1-acyldipyrromethane, with toluene as solvent and the addition of MgBr<sub>2</sub> and 1,8-diazabicyclo[5.4.0]undec-7-ene (DBU), or by Suzuki coupling reaction catalyzed by Pd reagent, in which the appropriate addition of metal ions as catalysts could increase the yield.<sup>28</sup> Third, the ABAB- porphyrins are formed by condensation of AB- 1-hydroxydipyrromethane under acid catalysis and DDQ oxidation, whereas this reaction is prone to acid interference.<sup>29</sup> Fourth, as pictured in Figure 1.5(b), the ABCD- porphyrins are formed by preparation A- dipyrrole first, then followed by ABC- 1,9-diacyl dipyrrole through stepwise acylation reaction and condensation with D- dipyrrole. These four are [2+2] synthesis, which have gained popularity in recent years owing to the high degree of versatility.

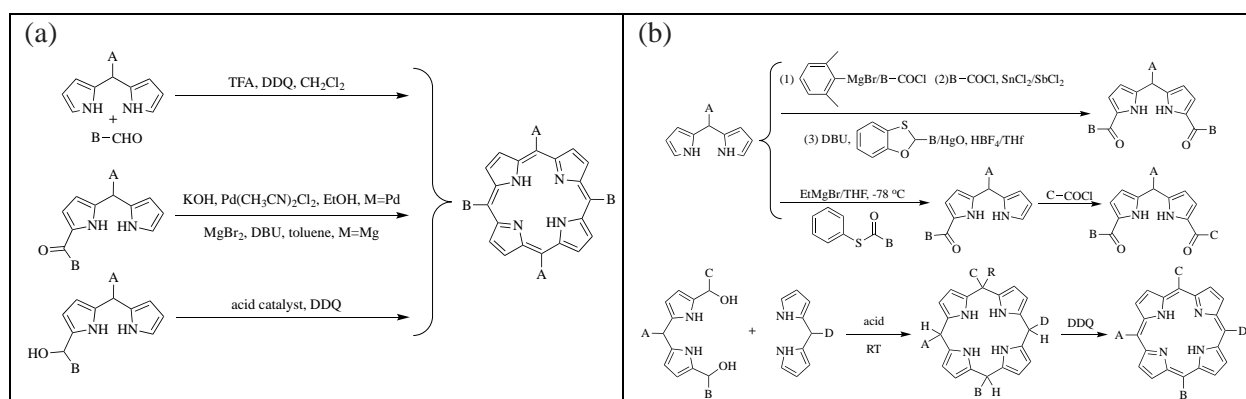


Figure 1.5. (a) Three different synthesis methods of ABAB- typed porphyrins;<sup>27,28,29</sup> (b) Synthesis of ABCD- typed porphyrin.

Inspired by previously published condensation of pyrrole and aldehyde with acid-catalyst in HCl/H<sub>2</sub>O/MeOH solvent systems and the production of oligocondensates,<sup>30</sup> Sanjib Kar's

group released a novel and straightforward two-step methodology for porphyrin synthesis in 2021.<sup>31</sup> As the procedures shown in Figure 1.6, the initial stage of this porphyrin synthesis process is the condensation of pyrrole and aldehyde with HCl as catalyst in the H<sub>2</sub>O-MeOH solvent mixture. In the second stage of the experiment, the precipitate is refluxed for 1-2 hours in reagent-grade DMF, then stirred overnight at room temperature in air. The pure porphyrins are produced and later purified by column chromatography and crystallization. This method eliminates the usage of costly chemicals such as DDQ or chloranil as oxidizing agent, nor does it require large amounts of dry chlorinated solvents.

This new methodology is used to synthesize symmetrical A<sub>4</sub>-porphyrins from aromatic aldehydes with various substituents with a maximum yield of 29% and trans-A<sub>2</sub>B<sub>2</sub>-porphyrins from dipyrromethanes with different substituents in a maximum yield of 40%. Despite that the yield is not a record number, with repeatable yields of 10-40% and high purity, the present method is the most straightforward and cost-effective approach for synthesizing porphyrins on a gram-scale. Meanwhile, this method offers a solution for green synthesis of porphyrins, paving their way to wider applications.

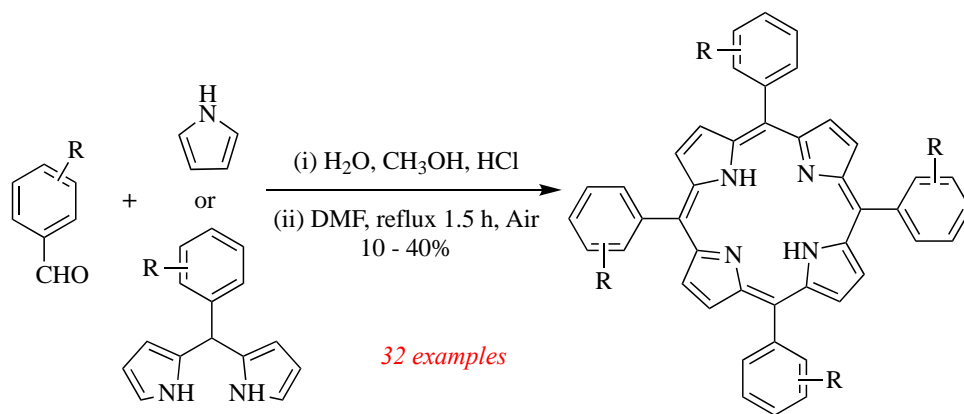


Figure 1.6. Two-step methodology for synthesis of porphyrin.<sup>31</sup>

## 1.3 Functionalization of lanthanide porphyrin complexes

### 1.3.1 Photophysical properties and applications of *meso*-position functionalized lanthanide porphyrin complexes

The unique properties and prospective applications of asymmetric porphyrins attract continuous research interest. The synthesis of asymmetric *meso*-substituted porphyrins is not achieved in one stroke, but rather require careful design and precise reaction in multiple stages. At this stage, the majority of investigations on asymmetric *meso*-substituted porphyrins have concentrated on two or three *meso*-substituted porphyrins, with even fewer studies on four distinct substituents. These studies have led to the identification of some promising *meso*-functionalized lanthanide porphyrins.

In a 2011 study led by Bing Yan, Ln-THPP-Si (Ln = Nd, Yb; THPP = 5,10,15,20-tetra-(p-hydroxy)phenylporphyrin) hybrid materials were synthesized by bonding Ln-THPP with an inorganic silicon network covalently,<sup>32</sup> as shown in Figure 1.7(a). First, the THPP-Si was synthesized as a precursor through the hydrogen transfer reaction between the OH of porphyrin and 3-(triethoxysilyl)-propyl isocyanate (TEPIC) in a sol-gel process. Then, the final product Ln-THPP-Si is formed in hydrolysis and co-condensation with tetraethoxysilane (TEOS) with the presence of lanthanide ions.

This -position substitution gives rise to marked changes in the electronic absorption spectra of Yb-THPP-Si, as shown in Figure 1.7(b). Compared with that for the free porphyrin, there are substantial red shifts of about 9 nm in Soret-band at 428 nm and in the Q-band region. These red shifts originate from the organosilicon precursor alteration at the porphyrin *meso*-position. Additionally, the number of absorption peaks in Q-band region of complex reduces from four to two because of the increased symmetry, in consistent with Gouterman's four-orbit

concept. Lastly, there is a new small wide band at 345 nm observed in the absorption spectra of THPP-Si. The emergence of this band could be ascribed to the production of porphyrin aggregates or to the interaction of silanol and siloxane groups linked to the pore wall of the solid matrix.<sup>32</sup>

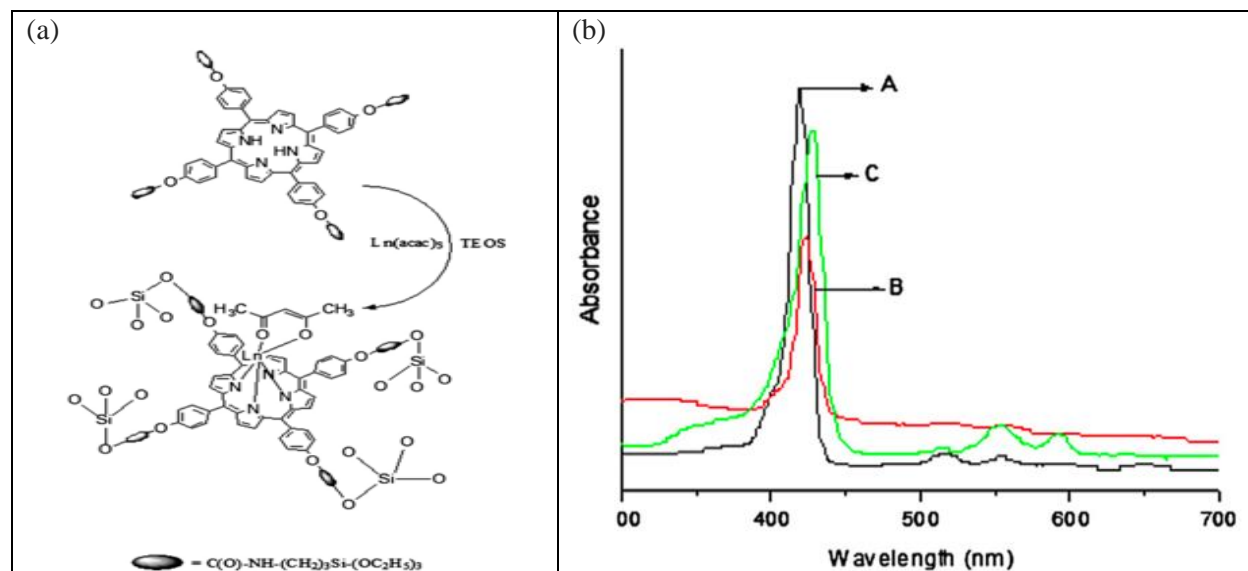


Figure 1.7. (a) Reaction scheme of the formation of the Ln-THPP-Si hybrid materials;<sup>32</sup> (b) Electronic absorption spectra of THPP(A), THPP-Si (B), Yb-THPP-Si (C) in DMF solutions.<sup>32</sup>

Two novel lanthanide porphyrin hybrids, Yb-THPP-Si and Nd-THPP-Si are used as near-infrared photosensitive materials. The normalized NIR emission spectra of Ln-THPP-Si (Ln = Nd and Yb) in Figure 1.8 show characteristic peaks for lanthanide ions. The emission peak of Nd-THPP-Si centered about 1060 nm is ascribed to the  $^4\text{F}_{3/2} - ^4\text{I}_{11/2}$  transition in the  $\text{Nd}^{3+}$  ion. Yb-THPP-Si, on the other hand, demonstrates a peak at 980 nm due to the  $^2\text{F}_{5/2} - ^2\text{F}_{7/2}$  transition of  $\text{Yb}^{3+}$  ions. This process could be used to develop new fluorescent materials utilizing inorganic substrates and lanthanide complexes that display NIR fluorescence.



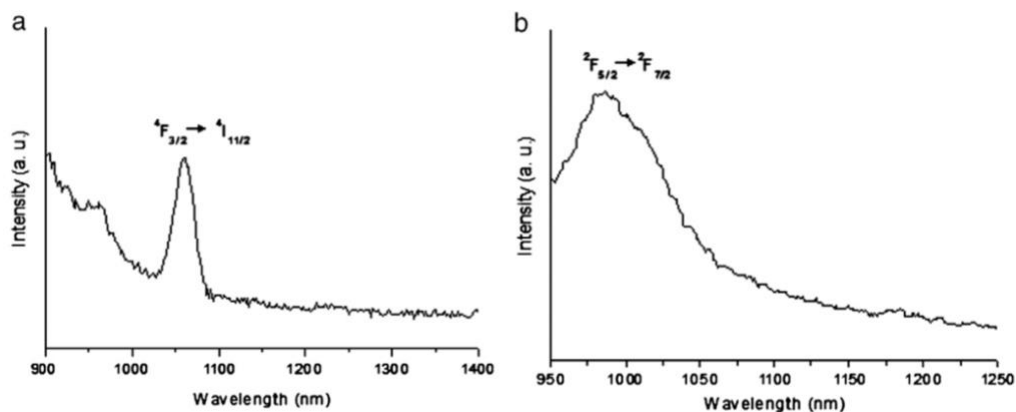


Figure 1.8. Normalized emission spectra for Ln-THPP-Si, (a) Ln = Nd ( $\lambda_{\text{ex}} = 340$  nm) and (b) Ln = Yb ( $\lambda_{\text{ex}} = 390$  nm).<sup>32</sup>

The same group later in 2012 reported the functionalization of phen-Ln-THPP and phen-Ln-PPIX (Ln = Nd<sup>3+</sup>, Yb<sup>3+</sup>) with SBA-15 mesoporous silica network using a similar method.<sup>33</sup> Functionalization of tetra(p-hydroxyphenyl)porphyrin (THPP) and protoporphyrin IX (PPIX) was carried out through tetraethoxysilane (TEOS) condensation method in the presence of Pluronic P123 surfactant. Beside SBA-15, the THPP and PPIX ligands were grafted using the coupling agents 3-(triethoxysilyl)-propyl isocyanate (TEPIC) and 3-aminopropyltriethoxysilane (APTES). Later on, the lanthanide ion (Nd<sup>3+</sup>, Yb<sup>3+</sup>) and 1,10-phenanthroline (phen) were incorporated to form hybrids phen-Ln-THPP-SBA-15 and phen-Ln-PPIX-SBA-15. The synthesis of phen-Ln-THPP-SBA-15 hybrids as an example is shown in Figure 1.9. Both lanthanide hybrids maintain an ordered mesoporous structure, while the surface properties of mesoporous silicates could be modified by organic functionalization of the porphyrin ligands.

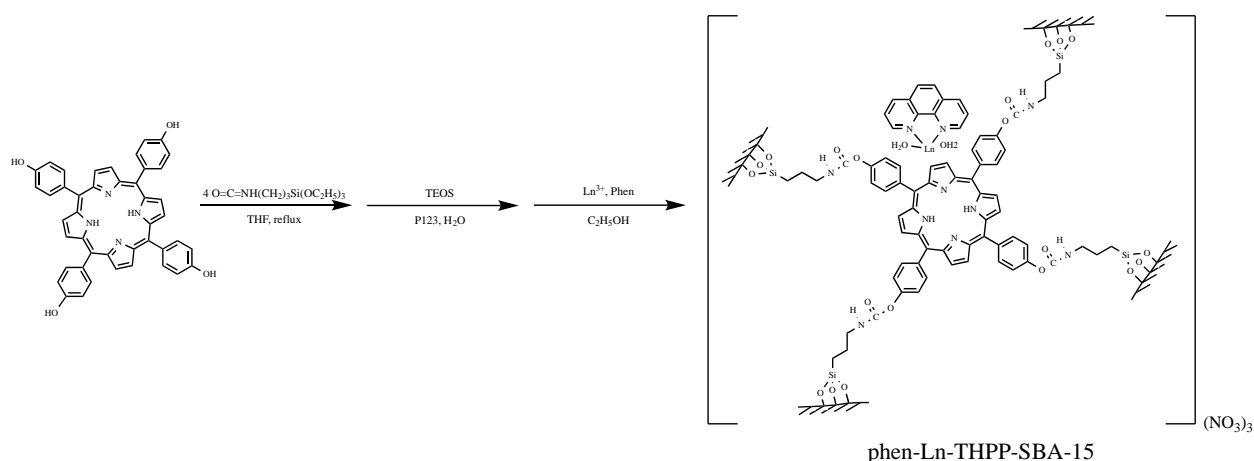


Figure 1.9. The synthesis of phen-Ln-THPP-SBA-15 hybrids.<sup>33</sup>

The emission properties of two  $\text{Nd}^{3+}$  hybrids under excitation about 375 nm are shown in Figure 1.10. The two distinct emission peaks exist at 1058 nm and 1326 nm from phen-Nd-THPP-SBA-15 complex and at 1060 and 1330 nm from phen-Nd-PLXX-SBA-15. Those peaks are characteristic to the  $^4\text{F}_{3/2} - ^4\text{I}_J$  transition of  $\text{Nd}^{3+}$  ion.<sup>34</sup> Similarly, the broad emission peaks centered at 985 nm and 986 nm from phen-Yb-THPP-SBA15 and phen-Yb-PIXX-SBA15 hybrids under the excitation of 400 nm, respectively, are attributed to  $^2\text{F}_{5/2} - ^2\text{F}_{7/2}$  transition of  $\text{Yb}^{3+}$  ions, as shown in Figure 1.11. Further investigation of fluorescence characteristics reveals that the distinctive NIR emission of the complexes is because of intramolecular energy transfer from the modified ligands to lanthanide ions.

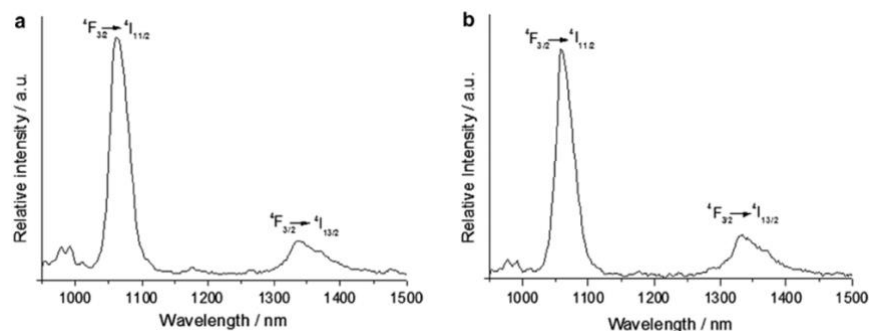


Figure 1.10. Near-infrared emission spectra of (a) phen-Nd-THPP-SBA15 and (b) phen-Nd-PPIX-SBA15 hybrids.<sup>34</sup>

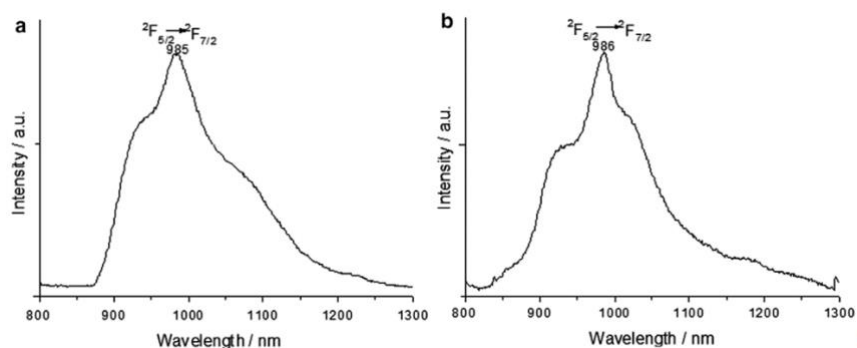


Figure 1.11. Near-infrared emission spectra of (a) phen-Yb-THPP-SBA15 and (b) phen-Yb-PPIX-SBA15 hybrids.<sup>34</sup>

Wai-Ming Kwok's group designed a mitochondria-targeted porphyrinate ytterbium(III) complex Yb-Rh with modified exocyclic ring of the porphyrin ligand to enhance water solubility and NIR luminescence.<sup>35,36</sup> As the molecular structure of Yb-Rh complex shown in Figure 1.12, the Yb(III) ion is capped with Kläui ligands  $[(\eta^5\text{-C}_5\text{H}_5)\text{Co}\{(\text{MeO})_2\text{P}=\text{O}\}_3]$  to prevent Yb(III) ion from being solvolysis. The linkage of Rhodamine B (Rh) in Yb-Rh complex operates as a specific subcellular localization for mitochondria, and the short polyethylene glycol (PEG) chain increases the overall water solubility of the complex.

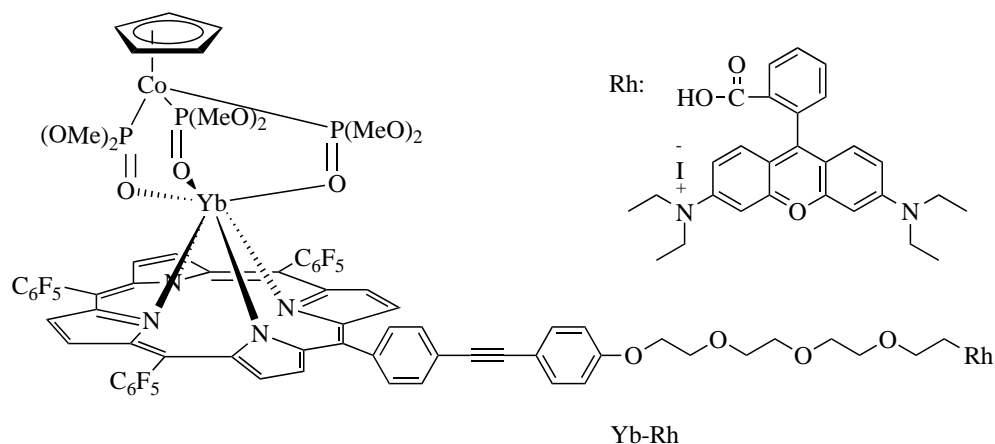


Figure 1.12. Molecular structure of Yb-Rh complex.<sup>35</sup>

As shown in Figure 1.13, the as-synthesized Yb-Rh complex shows intense emissions in the visible range (650 nm) and the NIR range (1060 nm) under excitation at 430 nm. The visible

emission (550-700 nm) is attributed to porphyrin's  $\pi - \pi^*$  transition, while the NIR emission (925-1100 nm) is attributed to  $^5F_{5/2} - ^2F_{7/2}$  transition. Moreover, the NIR emission has a lifetime of 18.1  $\mu$ s and a quantum yield of ca. 2.5%, which had been a record quantum yield in aqueous phase media.

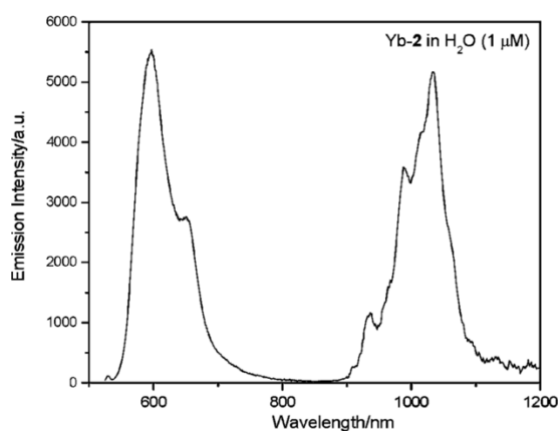


Figure 1.13. Emission spectrum of Yb-Rh ( $\lambda_{\text{ex}} = 430$  nm, 1  $\mu$ M in H<sub>2</sub>O, 298 K).<sup>35</sup>

The Yb-Rh complex has exceptional nonlinear optical characteristics, allowing efficient two-photon excitation with a two-photon absorption cross section of 375 GM when irradiated with an 860 nm femtosecond laser. Before this, no NIR porphyrinate lanthanide complex with two-photon excitation characteristics had been observed.<sup>35</sup> The possibility of being excited under NIR light lends this probe substantial potential in the area of biological imaging. Benefiting from the capping, the Yb-Rh complex well its structure in the bioenvironmental media. In addition, the mitochondrial guidance of rhodamine B enables Yb-Rh to be used in cellular mitochondrial targeting imaging. Lastly, because of energy absorbed by the porphyrin was transferred to and absorbed by the Yb(III) ion, producing a quench of energy transfer prior to the porphyrin ligand and singlet oxygen, the Yb-Rh is free of both phototoxicity and dark toxicity in cells. The experimental results indicate that Yb-Rh is an effective NIR bio-probe for mitochondria and has significant application prospects.

Based on study discussed above, in 2013, Wai-Kwok Wong's group synthesized the Yb-N complex as a fluorescence probe to differentiate tumor cells from normal cells, using the Yb-Rh and Ligand-N compounds as controls.<sup>37</sup> As molecular structures shown in Figure 1.14, the Yb-N complex has a similar structure with Yb-Rh. One *meso*-position in the porphyrin ligand of Yb-N complex is linked with a triethylamine group through a short PEG chain.

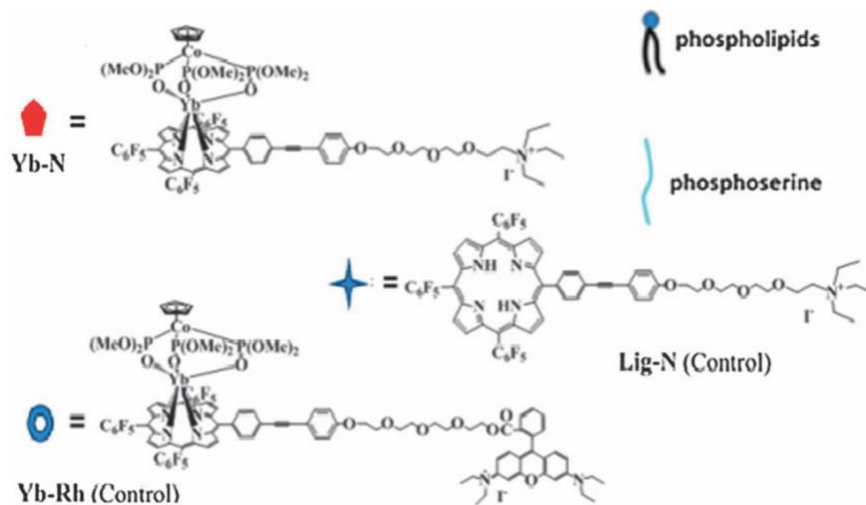


Figure 1.14. Molecular structure of Yb-N complex and Lig-N and Yb-Rh as the controls.<sup>37</sup>

While Yb-N and Yb-Rh complexes both exhibit comparable NIR fluorescence properties, the charge fraction and site resistance of Yb-N complex allow it to recognize the phospholipid anion cell membrane in tumor cells. *In vitro* imaging experiments using five human tumor cells, cervical HeLa, lung A549, nasopharyngeal HK-1, nasopharyngeal HONE-1 and neuroblastoma SK-N-SH, it is only the Yb-N complex shows selectivity for the tumor cell membranes and emits red light in them, but not in normal cells, under the same culture conditions, as pictured in Figure 1.15.

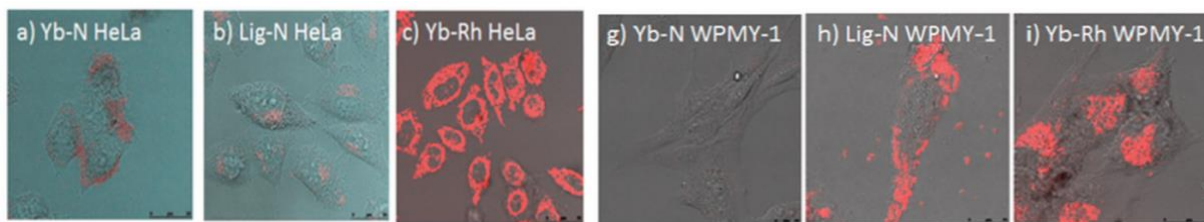


Figure 1.15. The *in vitro* imaging, emission spectra of Yb-N/Lig-N/Yb-Rh in human lung tumor cells HeLa and human normal prostate cells WPMY-1 ( $\lambda_{\text{ex}} = 430 \text{ nm}$ , 1 mM and 3 hours incubation time).<sup>37</sup>

By *in vitro* imaging, the water-soluble phospholipid marker Yb-N distinguished tumor cells from normal cells, giving critical evidence that anionic phospholipids on tumor cells were possible therapeutic targets. Although the Yb-N complex is tightly bound to anionic phospholipid species in solution, which allows the identification of some tumor cells through long-lasting visible to NIR region lanthanide fluorescence. However, this complex has a restriction in that it is incapable of producing  $^1\text{O}_2$ . Appropriate and modest dose of  $^1\text{O}_2$  have been shown to be efficient in eliminating tumor cells (low concentration of 5%). Thus, a new gadolinium porphyrin (Gd-N) complex was synthesized by Wai-Kwok Wong's group in 2014.<sup>38</sup> The Gd-N complex is a prospective PDT agent that exhibited a greater quantum yield of singlet oxygen and characteristic NIR emission upon photoexcitation using Yb-N as a building block.

According to the spectroscopic studies, Yb-N has a single-linear state oxygen quantum yield of 0%, whereas Gd-N has this quantum yield of 51%. This result is achieved because of greater energy gap between the porphyrin and Gd ion comparing to porphyrin and Yb ion. In Yb-N complex, the most energy absorbed by porphyrin is efficiently transferred to the ytterbium through the heavy atom effect, which exclusively provides the distinctive f-f emission. In contrast to Yb-N complex, roughly half of the energy absorbed by porphyrin is used to make  $^1\text{O}_2$ , while the rest is used to generate NIR emission in Gd-N complex, which is contributed to its high single-linear oxygen quantum yield. A detailed analysis of Gd-N complex demonstrates that it

could identify tumor cells within the first six dosage hours through its anionic phosphatidylserine membrane. It could penetrate tumor cells and generate  $^1\text{O}_2$  in response to laser irradiation at a certain wavelength. The Gd-N complex could effectively target tumors after a simple blood vessel injection, according to the conclusions of *in vivo* mice models and biodistribution studies.

The conclusions of *in vivo* mice models and biodistribution experiments further reveal that Gd-N could effectively target tumors after a simple blood vessel injection. As shown in Figure 1.16, after 24 hours of therapy, solid tumors shrank when  $^1\text{O}_2$  is released from the porphyrin. Thus, Gd-N complex could form a basis for new-generation developing of smart lanthanide porphyrins PDT agents using for actual tumor tracking, imaging, and killing.

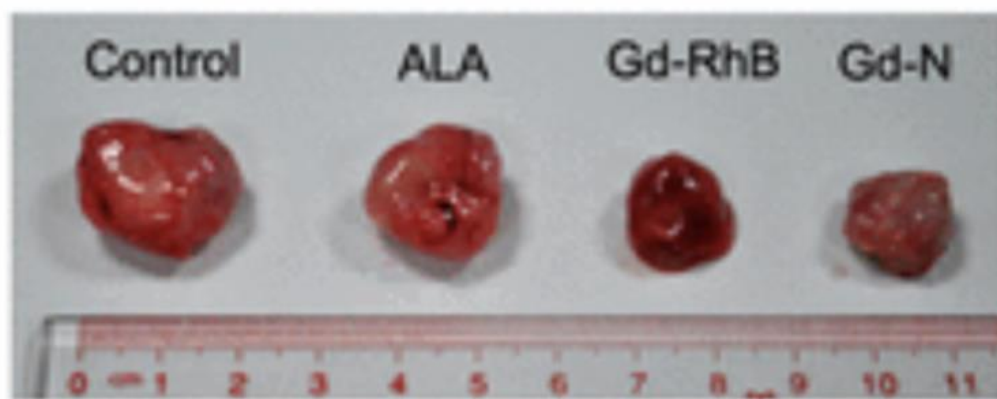


Figure 1.16. *In vivo* tumor inhibition assays of Gd-N.<sup>38</sup>

In 2014, Wai-Kwok Wong's group reported YbPor-L complex, a *meso*-position functionalized porphyrin molecule through the rhodamine-free intermediate YbPor-SS for the identification of heavy  $\text{Hg}^{2+}$  ions.<sup>4</sup> The molecular structures of YbPor-L and YbPor-SS complexes are shown in Figure 1.17. This research is inspired by the previously published biochromatic sensing systems, including rhodamine units complexed with organic chromophores and fluorescent transition metals and the stable NIR fluorescence of porphyrinate ytterbium complexes in aqueous solution.<sup>35, 39</sup>

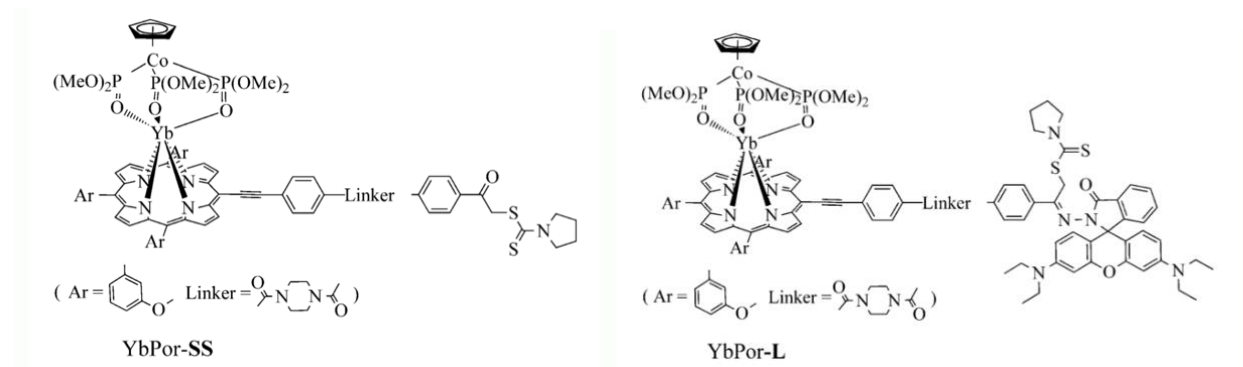


Figure 1.17. Molecular structures of YbPor-SS and YbPor-L complexes.<sup>4</sup>

As the spectra shown in Figure 1.18, The YbPor-L complex exhibits the typical absorption spectrum of metalloporphyrin molecule, with a strong Soret-band peak at 420 nm and two modest peaks between in 500-700 nm Q-band region. With the excitation at 440 nm, the YbPor-L complex shows moderate red emission with low emission yield from the  $\pi$ - $\pi$  transition of porphyrin ligand. It also exhibits comparatively strong NIR emission, which is attributed to the  $^2F_{5/2} - ^2F_{7/2}$  transition of Yb(III) ion. The similar absorption and emission spectra are observed for the intermediate YbPor-SS under the same conditions, indicating that the photophysical properties of the porphyrinate ytterbium complex are not significantly affected by the presence of the ring-closed Rhodamine B unit.



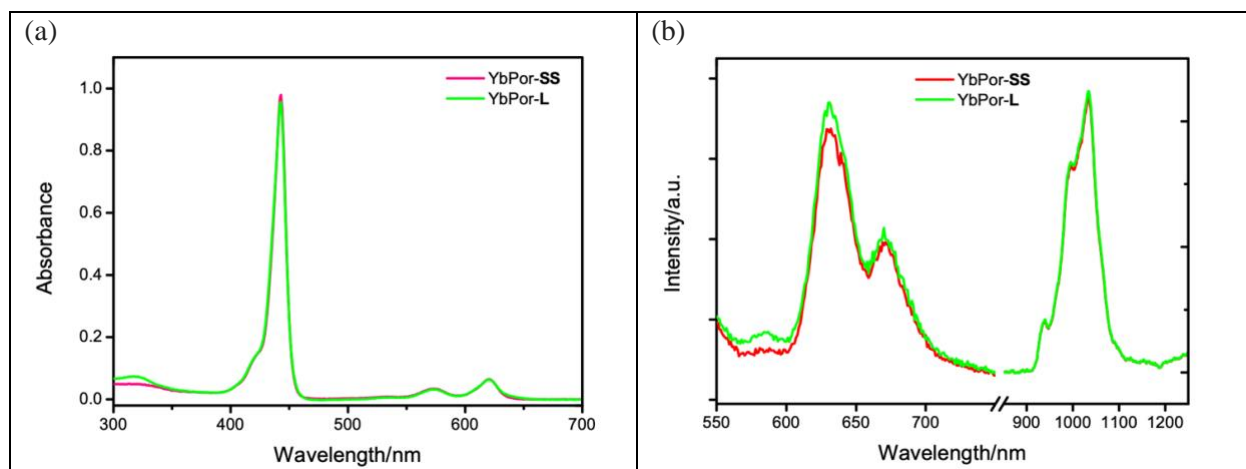


Figure 1.18. (a) Absorption spectra of YbPor-SS and YbPor-L in CH<sub>3</sub>CN/HEPES buffer (2:1, v/v, pH = 7.4);<sup>4</sup> (b) Visible and near-infrared emission spectra of YbPor-SS and YbPor-L in CH<sub>3</sub>CN/HEPES buffer (2:1, v/v, pH = 7.4),  $\lambda_{\text{ex}} = 440 \text{ nm}$ .<sup>4</sup>

Notably, The addition of Hg(ClO<sub>4</sub>)<sub>2</sub> as Hg<sup>2+</sup> ion source in the YbPor-L buffer solution results in an eightfold enhancement in the absorbance at 570 nm, as shown in Figure 1.19(a), and the solution color changes from green to burgundy. In contrast, the absorbance at 440 and 620 nm remained unchanged. Also, the addition of Hg<sup>2+</sup> ions in the intermediate YbPor-SS buffer has no effect on the absorption. This is ascribed to the ring-opening of the rhodamine B sensing unit in the YbPor-L complex after its association with Hg<sup>2+</sup> ions. As the emission spectra shown in Figure 1.19(b), the YbPor-L complex exhibits considerable emission enhancement at 590 nm in red area and 1030 nm in the NIR region of with increasing Hg<sup>2+</sup> concentration when excited at 570 nm. The YbPor-L complex has a strong binding selectivity in both visible and NIR regions, since only Hg<sup>2+</sup> ions produce a color change of the YbPor-L buffer solution. The properties of the porphyrinate ytterbium complex and the rhodamine B-derived unit allow the great sensitivity and selectivity for Hg<sup>2+</sup> ions in buffered solutions, indicating that the YbPor-L complex has promise as a time-resolved Hg<sup>2+</sup> ion detector.

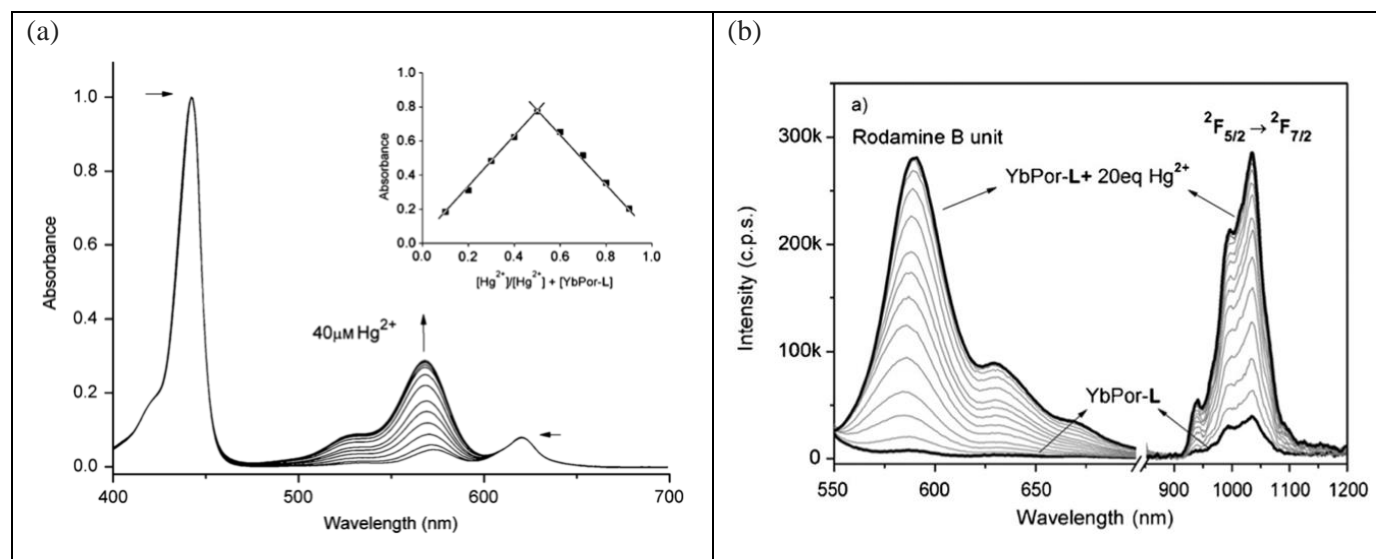


Figure 1.19. (a) Changes in absorption spectra of YbPor-L (5  $\mu\text{M}$ ) in  $\text{CH}_3\text{CN}/\text{HEPES}$  buffer (2:1, v/v, pH 7.4) upon addition of  $\text{Hg}^{2+}$  (40  $\mu\text{M}$ ). Inset: Job's plot between YbPor-L and  $\text{Hg}^{2+}$ ; (b) Dual emission spectra ( $\lambda_{\text{ex}} = 570 \text{ nm}$ ) of YbPor-L (5  $\mu\text{M}$ ) in  $\text{CH}_3\text{CN}/\text{HEPES}$  buffer (2:1, v/v, pH 7.4) upon addition of  $\text{Hg}^{2+}$  ion (0 to 20 equiv.).<sup>4</sup>

Lanthanide porphyrins have promising applications in telecommunications, light-emitting devices, and bioimaging because of their strong NIR emission. But significantly increasing the quantum yield of those complex still remains a difficulty. In 2017, Song Gao and his research group synthesized a series of NIR-emitting Yb complexes, sandwiched between octafluorinated porphyrinate antenna ligands and deuterated Kläui ligands.<sup>40</sup> One of these complexes has a remarkable quantum yield of 63%, compared to the 12% of best quantum yield for similar Yb(III) complex previously reported.<sup>40, 41</sup> A series of octafluoroporphyrin products are prepared by the Lindsey's method, 3,4-difluoropyrrole and the corresponding benzaldehydes (pentafluorobenzaldehyde, 2,6-difluorobenzaldehyde, and 4-trifluoromethylbenzaldehyde) are condensed with the boron trifluoride ether as catalyst.

As the molecular structures and emission spectra of complexes shown in Figure 1.20(a), [D18]-1-Yb complex with (2,3,7,8,12,13,17,18-octafluoro-5,10,15,20-

tetrakis(pentafluorophenyl)porphyrin as antenna ligand, comparing with [D18]-2-Yb and [D26]-2-Yb porphyrin as references, it could be concluded that when the C-H oscillator is completely replaced by the C-F oscillator, the emission quenching could be minimized, resulting in high fluorescence emission quantum yields. This series of fluorinated Yb(III) complexes has a similar UV-Vis absorption and NIR emission spectrum to ytterbium porphyrin complexes. The increased quantum yield of those fluorinated porphyrinate ytterbium complexes opens up a new avenue for photoconversion system design.

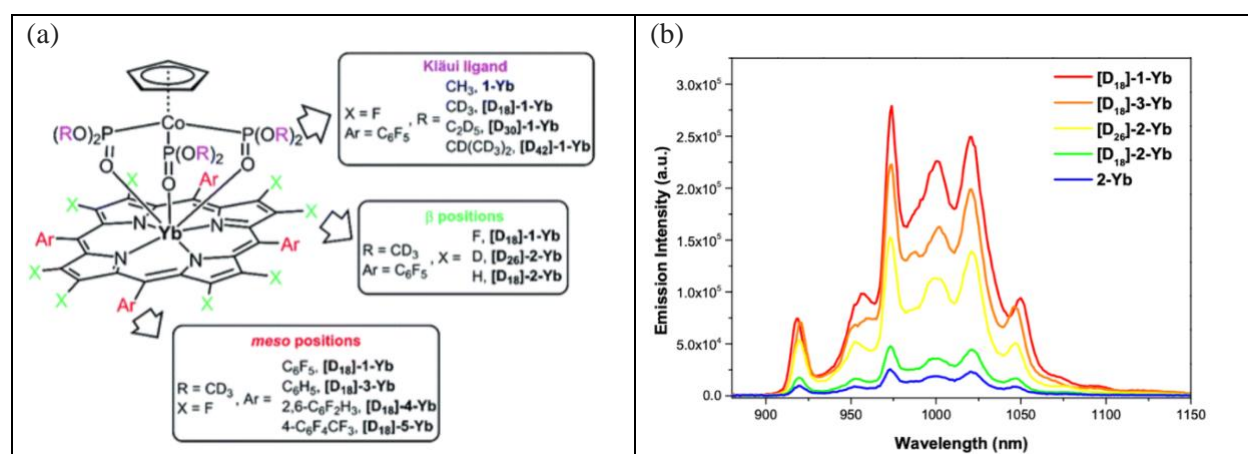


Figure 1.20. (a) Molecular structures of the Ln(III) complexes; (b) Emission spectra of the ytterbium complexes with various degrees of C-H bond replacement under the same conditions ( $\lambda_{\text{ex}} = 425$  nm, Abs = 0.10).<sup>40</sup>

For the investigation of NIR bioimaging in living cells and ytterbium octafluorinated porphyrin compounds, in 2018, Jun-Long Zhang's group reported the synthesis of water-soluble ytterbium complexes through carboxylates and cationic phosphonium groups.<sup>42</sup>

As pictured in Figure 1.21, the *meso*-position functionalized porphyrins are synthesized through the [2+2] method condensed 2,6-difluoropyrrole with corresponding water-soluble benzaldehyde or pentafluorobenzaldehyde. Following by the reaction with lanthanide acetylacetonate and the partially deuterated Kläui ligand  $[(\eta^5\text{-C}_5\text{H}_5)\text{Co}\{\text{P}(\text{O})(\text{OMeD})_2\}_3]$ , a

series of lanthanide porphyrin complexes are formed. This class of ytterbium octafluoroporphyrin complexes has high fluorescence quantum yields (5.1-13%) in aqueous solution, high stability, and long decay lifetime (>100 ns), which makes them an attractive NIR molecular bio-probe for real-time visualization in clinical diagnostics and surgery.

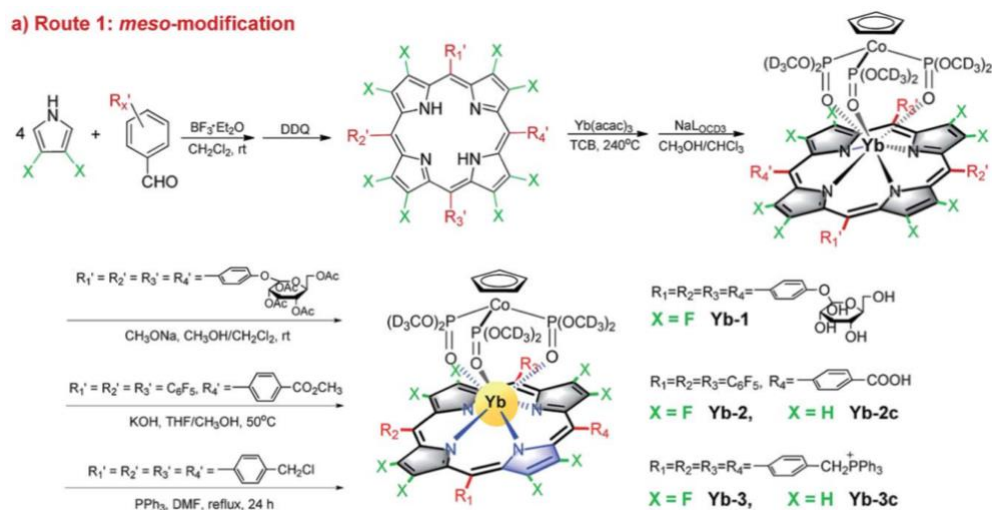


Figure 1.21. Synthesis routes of *meso*-modification Yb(III) complexes.<sup>42</sup>

Later in 2019, Jun-Long Zhang's group synthesized another similar ytterbium octafluoroporphyrin complexes, as shown in Figure 1.22. These complexes are also introducing the Kläui tripolar ligand [ $\eta^5\text{-C}_5\text{H}_5$ Co{P(=O)(OMe<sup>D</sup>)<sub>2</sub>}<sub>3</sub>] in the coordination site of ytterbium, but substituting the 4-carboxyphenyl derivative in one *meso*-position of porphyrin.<sup>43</sup>

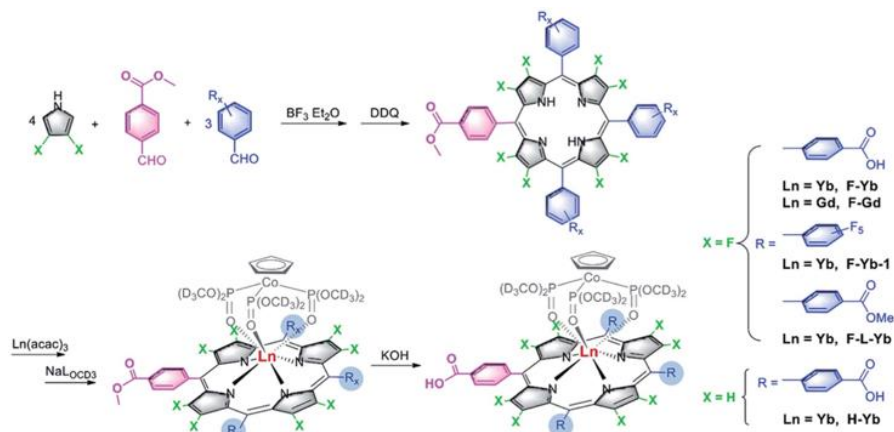


Figure 1.22. Synthetic procedures of the lanthanide complexes.<sup>43</sup>

In the NIR emission spectrum shown in Figure 1.23, F-Yb complex exhibits considerable pH-sensitive emission in aqueous solution between pH 9.0 and 5.0. Similarly, it is pH sensitive in live cells. The pH of F-Yb is measured in HeLa spheroids using Nigericin as an inducer, and there was a significant decrease in NIR emission lifetime when the pH increased.

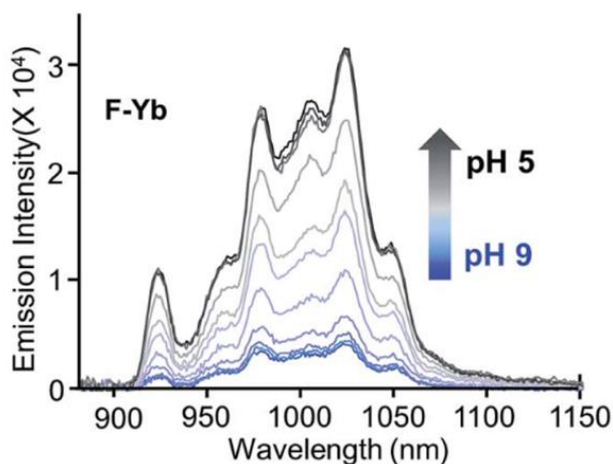


Figure 1.23. Fluorescence emission spectra of F-Yb in pH 5.0-9.0 PBS buffer.<sup>43</sup>

The majority of metalloporphyrin complexes utilize porphyrins as a single chromophore, while auxiliary ligands functionalized at various positions on the porphyrin are not engaged in the sensitization process of lanthanide metals because of their low absorption of visible light. In 2013, Xunjin Zhu's group reported a series of lanthanide porphyrin products, where the porphyrins substituted with boron dipyrrole-methylene (BODIPY) on one or more *meso*-positions, as a novel chromophore to co-sensitize the lanthanide ions.<sup>44</sup> One of the typical structure of complexes is shown in Figure 1.24 (upper one). When the conjugated structure with YbPor is increased, the BODIPY part could also absorb part of the low-energy visible light as an antenna ligand and transferred its energy to the YbPor counterpart, effectively sensitizing the NIR emission of Yb(III) ions and increasing the quantum efficiency of NIR to 0.73% with a lifetime of about 40  $\mu$ s.

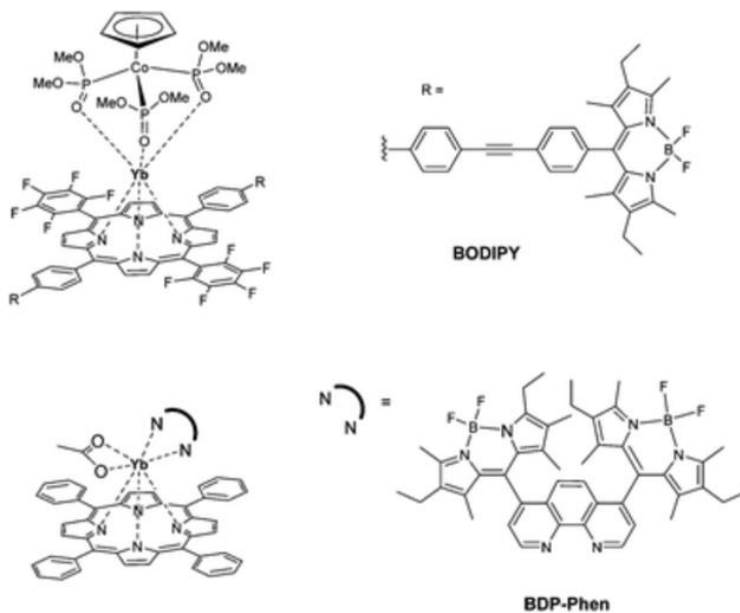


Figure 1.24. Molecular structures of porphyrin-based Yb(III) complexes conjugated to co-photosensitizers

BODIPY and bis(BODIPY)phenanthroline.<sup>44,45</sup>

In a related work, Hongshan He's group reported the ytterbium acetate complex Yb(TPP)(OAc)(BDP-Phen) with BODIPY as an antenna ligand and porphyrin as co-sensitizer. Its molecular structure is shown in Figure 1.24(below one). The Yb(TPP)(OAc)(BDP-Phen) complex exhibits a considerably higher absorption peak at 528 nm in Q-band region compared the reference Yb(TPP)(OAc)(Me-Phen), as shown in Figure 1.25(a). The NIR emission intensity of Yb(TPP)(OAc)(BDP-Phen) complex with the excitation at 525 nm is much higher than excited at the 375 nm of Soret-band, and 2.4 times higher than that of Yb(TPP)(OAc)(Me-Phen) reference under the same conditions, as shown in Figure 1.25(b). Introducing BODIPY and porphyrin as the co-sensitizers into the Yb(III) framework allows for intense NIR emission with a wider excitation window and provides an innovative and enhanced methods for NIR optical probes excited at long wavelengths.

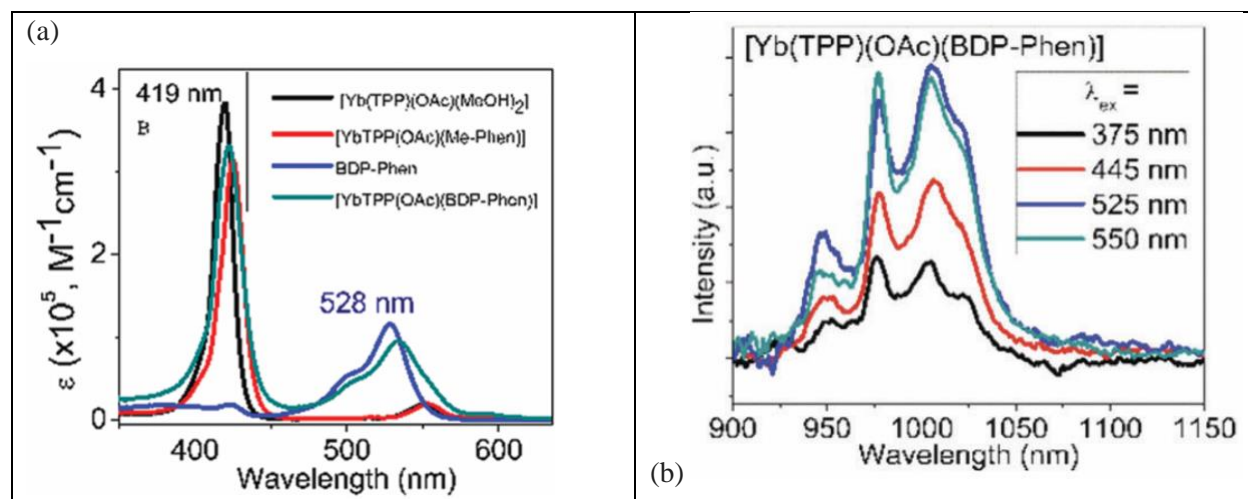


Figure 1.25. (a) Absorption spectra of BDP-Phen and Yb(III) complexes in DCM at room temperature;<sup>45</sup>

(b) The near-infrared emission spectra of [Yb(TPP)(OAc)(BDP-Phen)] under various excitation wavelengths ( $3.23 \times 10^{-5}$  M in DCM).<sup>45</sup>

Also investigating the conjugated structure of porphyrin chromophores, as shown in Figure 1.26, Ching-Yao Lin's group designed the visible range absorbing dye LD31 based on the previous works (LD14 and AN-4 complexes). The LD31 complex has a greatly extended  $\pi$ -electron conjugated structure as the electron donor because of the introduction of the benzene rings. It also has the absorption in wavelength up to 800 nm and the overall efficiency of power conversion reached a value of 10.3%.

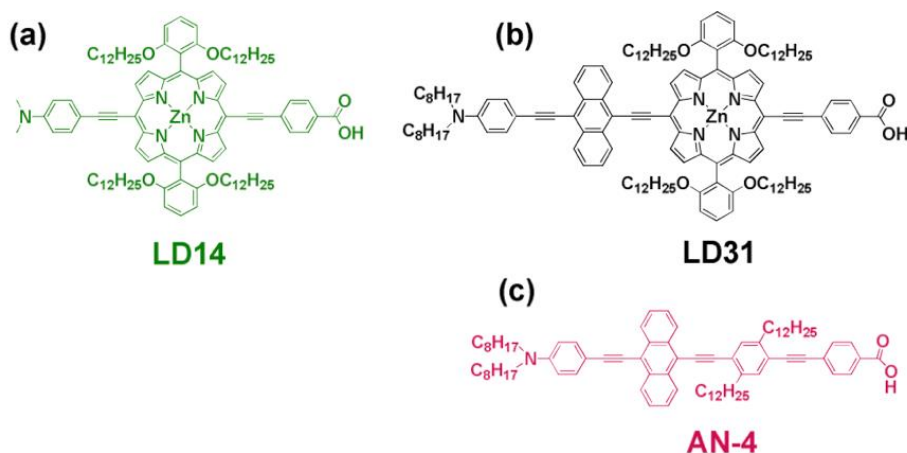


Figure 1.26. Molecular structures of (a) LD14, (b) LD31 and (c) AN-4.<sup>46</sup>

### 1.3.2 Photophysical properties and applications of $\beta$ -position functionalized lanthanide porphyrin complexes

With the considerable research on *meso*-substituted porphyrins, emphasis has progressively shifted to the  $\beta$ -position porphyrins. It is now possible to perform a series of reactions such as bromination and nitration at the  $\beta$ -position of porphyrins, as well as to link or bridge two porphyrin molecules directly through the  $\beta$ -position.<sup>47,48</sup> This indicates that more studies could now be carried on porphyrins not only in the *meso*-position but also in the  $\beta$ -position in order to synthesize various complexes that fulfill research requirements.

By modifying the structure of the inner porphyrin ring, Junlong Zhang's team reported a series of ytterbium acetylacetonate  $\beta$ -endoporphyrin complexes, with enhanced NIR fluorescence emission in 2014, which exhibits a 50-120% increase in NIR emission efficiency over the common ytterbium(III) porphyrin complexes.<sup>6</sup> The  $\beta$ -lactonization of the porphyrin ligand could boost the sensitization efficiency of  $\text{Yb}^{3+}$  NIR fluorescence emission by narrowing the energy gap between the porphyrin  $\text{T}_1$  state and the lowest excited state of  $\text{Yb}^{3+}$ .

In order to restore the NIR emission of the water-soluble ytterbium(III)  $\beta$ -pyrrolic modified porphyrin complex, the solvent quenching effect caused by the low coordination number could be eliminated by substituting a specific biomolecule in this complex, which is weakly coordinated to water. Thus, the solvent quenching effect is eliminated, and the NIR emission is regenerated for the purpose of identifying the target molecule. As shown in Figure 1.27(left), a  $\beta$ -lactonization poporphyrin ytterbium complex with all four porphyrin *meso*-sites glycosylated is synthesized by the reaction of ytterbium *meso*-tetrakis-(pentafluororophenyl)-porpholactone with 2,3,4,6-tetra-O-acetyl glucosyl thioacetate.<sup>6</sup>



As shown in Figure 1.27(right), the NIR emission of this complex is activated in the presence of glucose oxidase and deactivated with the addition of glucose, allowing for the selective NIR detection of glucokinase in the presence of glucose. It is shown in this work, a novel concept for the functional modification of porphyrins to enhance the NIR emission efficiency of Ln-porpholactone complexes has emerged.

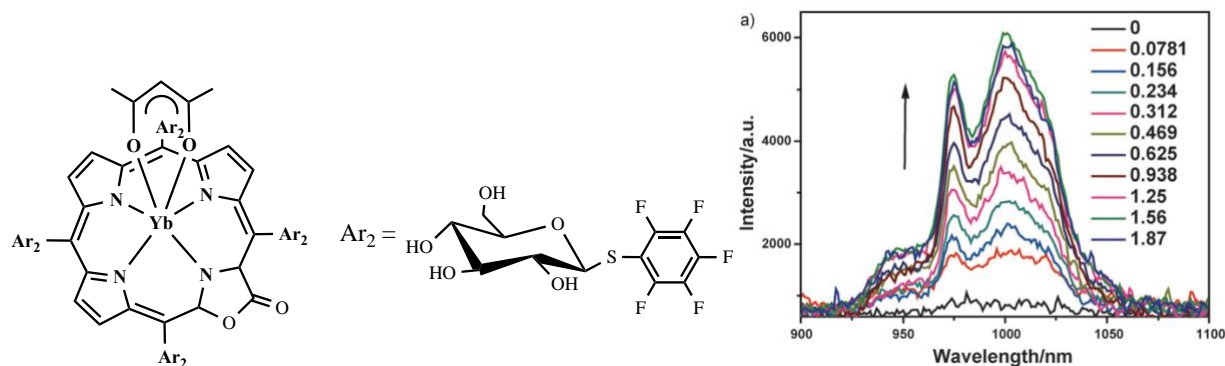


Figure 1.27. Near-infrared emission spectra of Glycosylated ytterbium porpholactone (4 μM) at various concentrations (μM) of GOx in Tris·HCl buffer (50 μM, pH 7.4) at 25.8 °C.<sup>6</sup>

In 2017, Junlong Zhang's group developed and synthesized cis/trans-Ln-porpholactone complex to investigate the impacts of regioisomerism effect on the energy transfer efficiency of lanthanide ion in NIR region.<sup>49</sup>

The position change of the  $\beta$ -substituent orientation in ytterbium complex has a significant effect on the  $T_1$  and  $T_1 \rightarrow Yb^*$  energy transfer processes of porphyrins. The  $T_1 \rightarrow Yb^*$  energy gap of cis-Yb ( $\sim 1152 \text{ cm}^{-1}$ ) is much larger than that of trans-Yb ( $\sim -25 \text{ cm}^{-1}$ ). The cis/trans-Ln-porpholactone complex could “turn on (cis)/off (trans)” the  $Yb^{3+}$  NIR emission with the energy transfer efficiency of about 84% and 12%, and the quantum yield of 3.3% and 0.4%, respectively. These results demonstrate that the nature of trilinear state of porphyrins could be precisely regulated by adjusting the regional isomerization effect of the lactone group to alter the energy level difference  $E(T_1 \rightarrow Ln^*)$  and the energy transfer efficiency between the  $T_1$  state and

the excited state of Ln<sup>3+</sup> ion,<sup>49</sup> as the Jablonski diagram shown in Figure 1.28. This presents a novel approach to optimizing and designing NIR-emitting lanthanide probes.

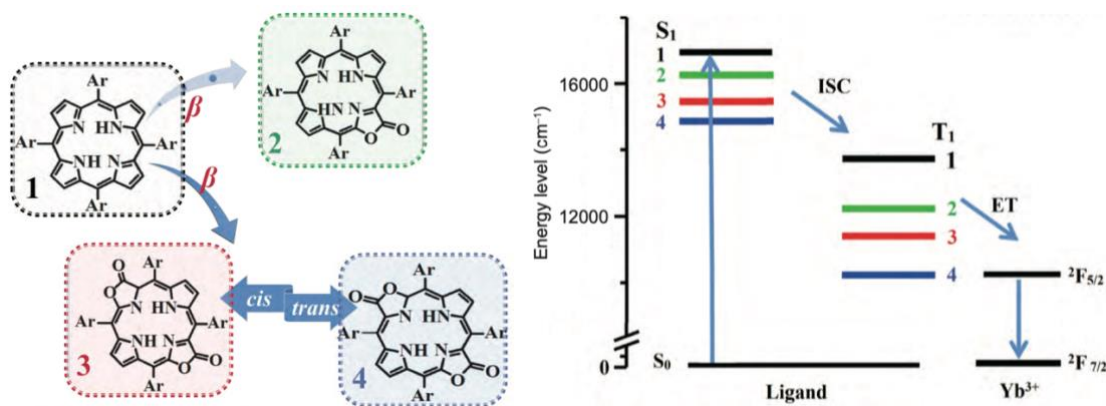


Figure 1.28. Schematic diagram of adjusting the porphyrinic T<sub>1</sub> energy state of porphyrin by changing the number and orientation alteration of  $\beta$ -substituent (color on line).<sup>49</sup>

To further investigate the influence of regioisomerism effect on the NIR emission of lanthanide metals, Junlong Zhang's group developed and synthesized the ytterbium porpholactone NIR emitters Yb-up and Yb-down,<sup>50</sup> as shown in Figure 1.29, in which the Yb<sup>3+</sup> is sandwiched between a porpholactone chromophore (7,8,12,13,17,18-hexafluoro-5,10,15,20-tetrakis(pentafluorophenyl) porpholactone) and a deuterated Kläui ligand.

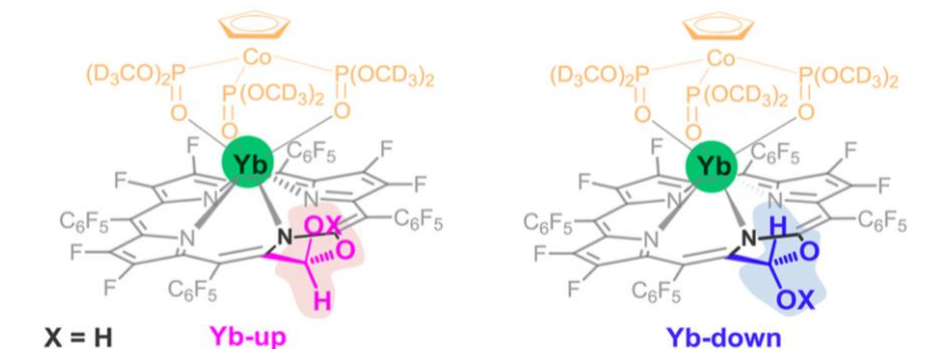


Figure 1.29. Chemistry structures of Yb-up and Yb-down.<sup>50</sup>

The  $\beta$ -hydroxyl group on the periphery of porpholactone gives two stereoisomerisms. The Yb-up complex forms intermolecular hydrogen bonds with the Kläui ligand when the  $\beta$ -OH

is oriented in the same direction as the Yb(III) center, and Yb-down complex has no effect on the intermolecular force when the  $\beta$ -OH is oriented in the opposite direction as the Yb(III) center.

As shown in Figure 1.30(a), the absorption spectra of Yb-up and Yb-down complexes are same, with an intense peak at 402 nm in Soret-band region and three distinctive peaks between 550 to 700 nm in Q-band region. This indicates the stereoisomerization of  $\beta$ -OH group does not modify the lowest triplet state of the porphyrin. It is known the NIR emission of Ln is highly dependent on the vibration of the X-H (X = C, N and O) bonds from previous studies. As shown in Figure 1.30(b), with the excitation at 406 nm, the Yb-down displays a 2-fold greater emission intensity and longer lifetime than Yb-up. The O-H vibration rather than C-H bond on  $\beta$ -mercapto position is the most likely explanation for the difference NIR emission of Yb-up/down. It is also indicated the intermolecular OH bond has a quenching effect on the NIR emission of Ln complexes. This discovery presents a fresh perspective for studying the NIR emission characteristics of lanthanide metals. In the future, novel NIR-emitting functional materials could be developed by modifying and optimizing the secondary coordination layers.

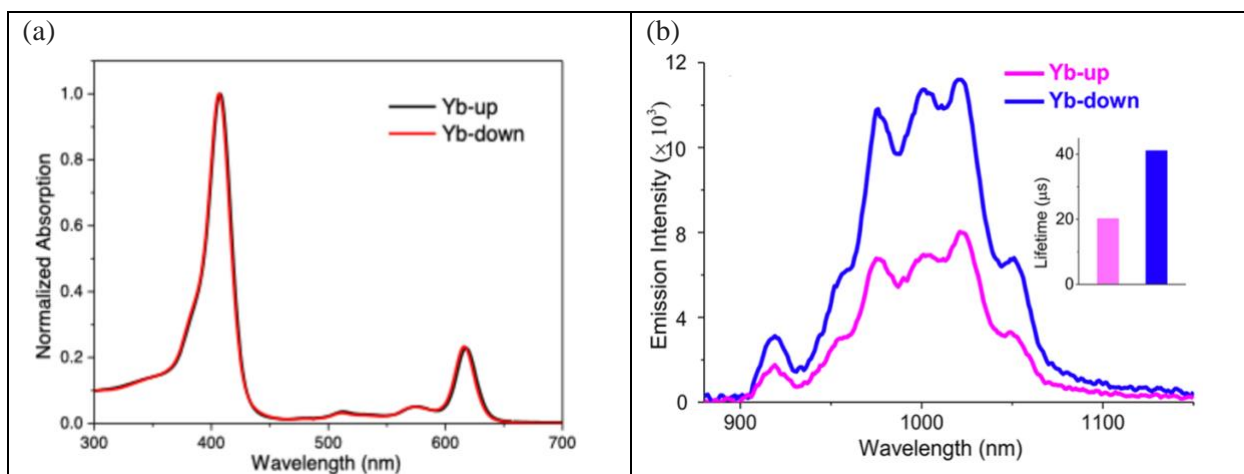


Figure 1.30. (a) Normalized absorption spectra of Yb-up/down in  $\text{CH}_2\text{Cl}_2$  at room temperature;<sup>50</sup> (b) Emission

intensities of Yb-up and Yb-down in  $\text{CH}_2\text{Cl}_2$  at room temperature ( $\lambda_{\text{ex}} = 406 \text{ nm}$ ,  $A_{406 \text{ nm}} = 0.1$ ).<sup>50</sup>

The design and preparation of molecular phototherapeutic reagents could be substantially simplified, and the foundation for the Practicality of phototherapy could be established if multifunctional collection and balancing could be accomplished in the same molecule in an easy and controlled manner. The key to achieving this goal is to finely regulate the dissipation pathway of excited state energy.

The groups of Jun-Long Zhang and Jonathan Sessler cleverly modulated the excited-state energy dissipation process of carbazole-based porphyrinoids complexes, resulting in a photosensitizer with both phototherapeutic and diagnostic capabilities in a single molecule.<sup>51</sup> The molecular structures shown in Figure 1.31.

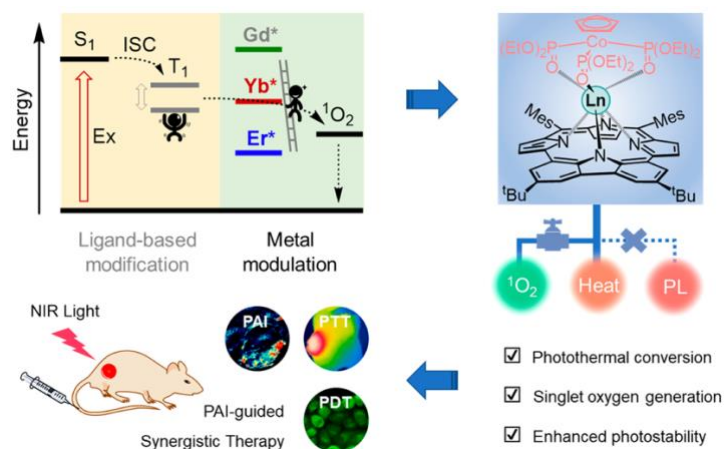


Figure 1.31. Schematic diagram of energy dissipation pathways in Ln complexes and photoacoustic imaging-guided photothermal/photodynamic synergy therapy.<sup>51</sup>

The carbazole-based porphyrinoids ligand is used to synthesize a variety of the NIR-emitting complexes (LnL, Ln = Gd, Yb, and Er) with different lanthanide centers. In the photothermal window of 650-850 nm, these compounds displayed a significant absorption. The absorption, emission, and transient absorption spectra, combined with theoretical calculations, demonstrate that the energy dissipation pathways of the Ln complexes under photoexcitation are highly reliant on the energy gap between the triplet state of ligand and the excited state of Ln ion.

Among them, the Yb complex (YbL) shows a good balance between energy dissipation pathways such as generation of single-linear state oxygen, exotherm and emission, while realizing the functions of photoacoustic imaging, photothermal therapy and photodynamic therapy. The efficient photothermal conversion efficiency ( $\eta = 45\%$ ) and excellent single-linear oxygen quantum yield ( $\Phi\Delta = 31\%$ ) are achieved by loading YbL complex onto mesoporous silica nanoparticles (MSN), while the YbL@MSN complex is both biocompatible and water-soluble.

In addition, the mice tumor model study demonstrates that YbL@MSN is capable of photothermal and photodynamic synergistic therapy *in vivo*, effectively inhibiting tumor development after a single NIR laser irradiation, as shown in Figure 1.32. In summary, this study proposes a design strategy for phototherapeutic reagents that balance the excited state features of photosensitizers through the carbazole-based porphyrinoids complexes.

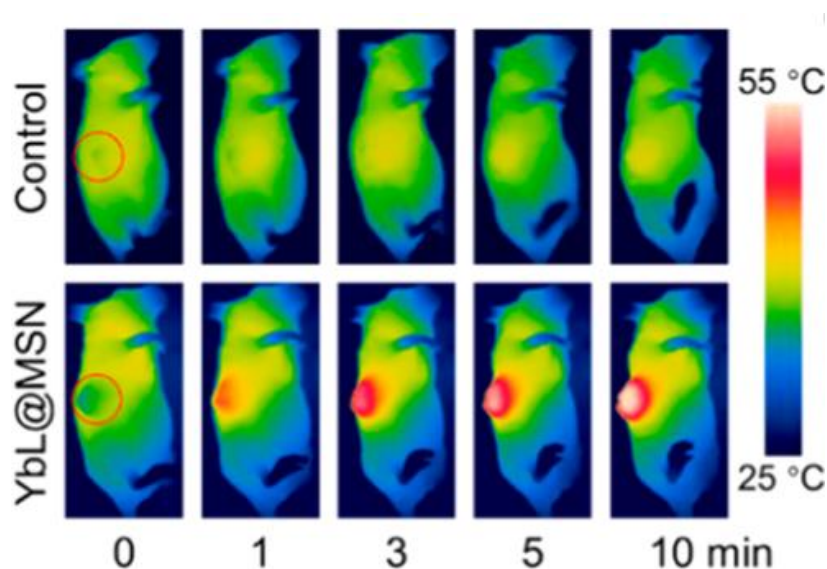


Figure 1.32. Infrared thermographs of the mice under laser irradiation (690 nm, 0.2 W/cm<sup>2</sup>) in the control and YbL@MSN groups.<sup>51</sup>

In lanthanide porpholactone complexes, the trilinear energy levels of porphyrin ligands are precisely regulate by introducing the lactone structure and controlling the orientation of the lactone groups to achieve the regulation of trilinear energy transfer processes, such as Yb(III) NIR emission, single-linear oxygen sensitization, photocatalytic reactions and trilinear annihilation up-conversion. The amplification of regioisomerism effect is achieved and the modulation of bio-functionality is realized through the regulation of aromaticity. Those benefits demonstrate the of development trends and broad application prospects of lanthanide porpholactone complexes in the biomedical fields.

### **1.3.3 Near-infrared emission properties of lanthanide porphyrin complexes**

Generally speaking, the fluorescence emission mechanism of lanthanide ions is classified into three types,<sup>52</sup> as shown in Figure 1.33. First, the substrate molecule is excited and transfers energy to the lanthanide ion after the energy level jump. Second, the charge that is initially fixed in the ligand's L orbital is transferred to the metal's M orbital, thus allowing the lanthanide ion to reach the excited state. this process refers to the metal-ligand charge jumping mechanism (LMCT: ligand-to-metal charge transfer).<sup>53</sup> Third, the excited state of the ligand transmits energy to the lanthanide ion, which process is known as intramolecular energy transfer, or antenna effect. The lanthanide ions produce fluorescence when they transition from the excited state to the ground state using these three mechanisms.

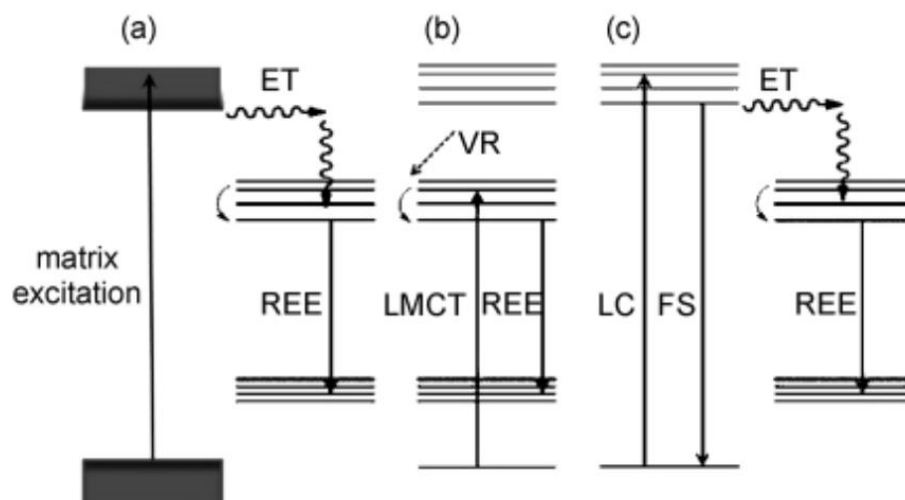


Figure 1.33. Three paths to lanthanide fluorescence emission (ET: energy transfer, REE: rare earth emission, VR: vibrational relaxation, LMCT: ligand→metal charge transfer absorption, LC: ligand-centered absorption, FS: fluorescence).<sup>52</sup>

Lanthanide coordination complexes are one of the most active frontiers in the study of lanthanide phosphorescent materials. In the 1960s, Crosby et al. systematically studied and elaborated the phosphorescent mechanism of such complexes.<sup>54,55,56</sup> The widely accepted view is that the antenna effect occurred when the appropriate organic ligands and lanthanide ion are coordinated. The absorbed energy is transferred to the lanthanide ion through intramolecular energy transfer, and the fluorescence of lanthanide ion is sensitized, effectively enhancing the fluorescent properties. This process is separated into three different phases: ligand energy absorption, ligand-lanthanide ion energy transfer and lanthanide ion emission.

Thus far, the research of the fluorescence characteristics of lanthanide complexes have matured, beginning with the study of modified functional groups on ligands. Especially, it is critical to use the X-ray single crystal diffraction method for studying the effect of complex structure on fluorescence characteristics.<sup>57</sup> The NIR-emitting lanthanide ions are very sensitive to

vibrational passivation. The f4 high-energy oscillators in the ligands, such as C-H and O-H bonds, predominantly quenched the excited states of lanthanide ions in a nonradiative manner, resulting in decreased light emission intensity and a shorter excited state lifetime for lanthanides. Thus, synthesizing lanthanide complexes with efficient emission properties often requires deuterating the H atom in C-H bond or substituting a C-F or C-Br bond for C-H bond in the ligands, which reduce energy loss owing to ligand vibration.<sup>58,59</sup>

In addition, since H<sub>2</sub>O or other polar solvent molecules could have a quenching effect on the fluorescence of the complexes, a second ligand with sufficient coordination sites is required to shield the lanthanide ions from the interference of polar solvent molecules, thereby increasing the fluorescence intensity and emission efficiency of the complexes.<sup>60</sup> The new frontiers of supramolecular chemistry include the design and synthesis of macrocyclic lanthanide complexes based on the lock and key concept, as well as their application to light-emitting molecular devices and fluorescent probes.

#### **1.3.4 Comparison method for quantum yield calculation**

Fluorescence is one of very prevalent photoluminescent phenomena. Fluorophores form an energetically excited state when certain material molecules are irradiated by light, and eventually return to the ground state through deactivation (energy loss). In fluorescence, the principal deactivation mechanisms include radioactive leap (fluorescence), internal conversion, vibrational relaxation and inter-system scrambling. The fluorescence quantum yield ( $\Phi_F$ ) is defined as the ratio of photons absorbed to photons released by fluorescence. The greater value of  $\Phi_F$  indicates the stronger fluorescence of the complex, while the fluorescence quantum yield of a non-fluorescent substance is equal to or very close to zero.



As a result, it is vital to correctly determine the  $\Phi_F$ , which reflected the light intensity of the fluorescent compound. The most reliable method for determining  $\Phi_F$  is the “comparison method” proposed in the literature,<sup>61,62</sup> which is based on the preparation of a series of dilute solutions of a standard complex (reference) and substance to be measured. So that their absorptions at a certain wavelength are in a gradient. The emission peak with certain excitation wavelength is measured and the area of peak is integrated. A linear fit to the absorbances vs. integrated areas is performed, and the quantum yield is then calculated as follows:

$$\Phi_X = \Phi_{ST} \left( \frac{k_X}{k_{ST}} \right) \left( \frac{\eta_X^2}{\eta_{ST}^2} \right),$$

where  $\Phi_{ST}$  is the fluorescence quantum yield of the standard;  $\text{Grad}_X$  and  $\text{Grad}_{ST}$  are the gradients from the plot of integrated fluorescence emission intensity vs. absorbance of the complex and standard, respectively;  $\eta_X$  and  $\eta_{ST}$  are the solvent refractive indexes of standard and complex, respectively. It should be noted that to minimize the impact of self-absorption effect, the absorption of a cuvette with a 10 mm optical range should not exceed 0.1, same as the absorption of a cuvette with a 20 mm optical range should not exceed 0.2, and so on. Exceeding this number would lead to a nonlinear relationship as a result of the self-absorption effect, which has an effect on the measured fluorescence quantum efficiency.

## 1.4 Applications of other metalloporphyrin complexes

### 1.4.1 Applications in medical and biochemistry fields

Porphyrins and their metal complexes have a high affinity for a variety of tumor cells, could remain selectively inside tumor cells once introduced, and their unique photon absorption and emission properties could be used to detect and kill tumor cells. Therefore, it has been of great interest in the field of medical and biochemistry. Along with the fluorescent probes discussed above, self-assembled porphyrin nanoparticles have been extensively employed in these field.<sup>63,64</sup>

The majority of porphyrin photosensitizing molecules are hydrophobic, and their phototherapeutic efficiency is limited by aggregation and tumor localization. Nanosensitization of porphyrin photosensitizers through a nano metal-organic frame (NMOF) material platform is one of the effective approaches to overcome these drawbacks. Indeed, by introducing photosensitizing molecules in this manner of a periodic and porous NMOF framework, aggregation amongst photosensitizers is successfully avoided, and their cellular uptake at the tumor site during PDT therapy is significantly increased. Therefore, porphyrin photosensitizers could also be nanosized by a post-synthesis method using an NMOF platform.

The groups of Jinglan Kan and Yubin Dong used UiO-66 type NMOF and S-ethylthiol ester monosubstituted free porphyrin (TPP-SH) to synthesize novel UiO-66 type NMOF photosensitizer (UiO-66-TPP-SH) by post-modification under mild conditions, in other words, by post-synthesis with NMOF attached to the exterior surface of photosensitizer MOF nanoparticles,<sup>65</sup> as shown in Figure 1.34. Furthermore, the surface-localized porphyrin photosensitizer UiO-66-TPP-SH is facile to synthesize and has a higher singlet oxygen capacity than the TCPP & UiO-66 with internal sites. On the other hand, the generated MOF

nanoparticles exhibits minimal cytotoxicity, high membrane permeability and efficient single-linear oxygen generation capacity, making them potential photodynamic therapy photosensitizers for tumor therapy. This work suggests a new research direction for developing more novel and practical nano photosensitizers for PDT.

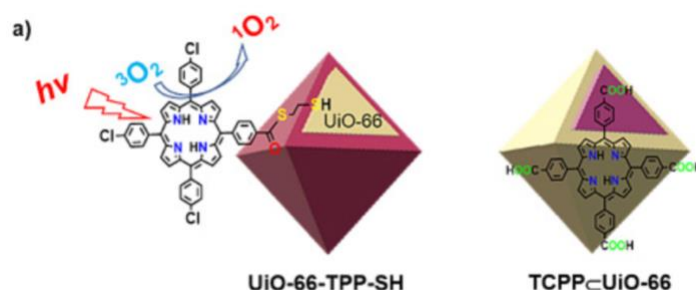


Figure 1.34. Schematic structure of surface-modified UiO-66-TPP-SH and one-pot method TCPP & UiO-66.<sup>65</sup>

Gang Zheng and his group used self-assembled porphyrin nanoparticles to examine the therapeutic efficiency of photodynamic and photothermal treatment on hypoxic tumor cells.<sup>66</sup> Following the illustration shown in Figure 1.35, in compared to photodynamic treatment, this self-assembled porphyrin nanoparticle photothermal therapy proves more successful in overcoming hypoxic circumstances and effectively ablating cells.

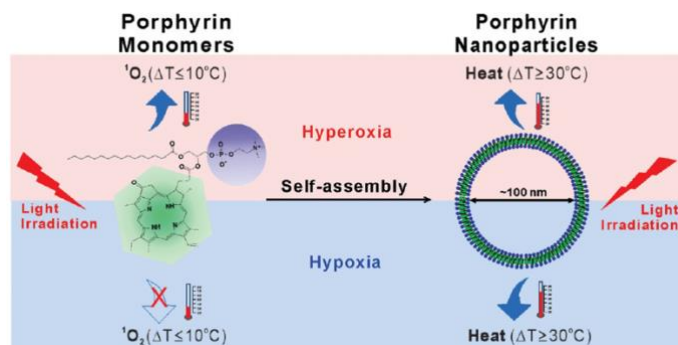


Figure 1.35. Schematic illustration of the study rationale and design.<sup>66</sup>

Wenbin Lin and his group pioneered the development of the chlorine-based metal nanoparticle organic framework DBC-UiO, as shown in Figure 1.36, which significantly enhance

its photophysical characteristics over the previously used DBP-UiO. In two mice models of tumors, DBC-UiO displays superior photodynamic characteristics.<sup>67,68</sup>

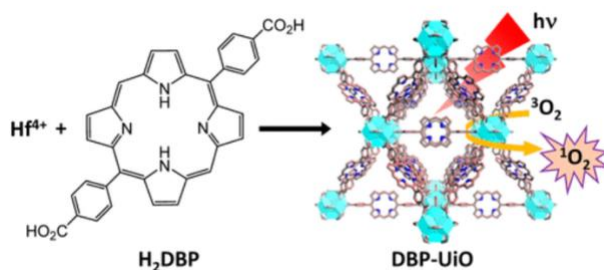


Figure 1.36. Synthesis of Hf-DBP NMOF and the schematic description of singlet oxygen generation process.<sup>67</sup>

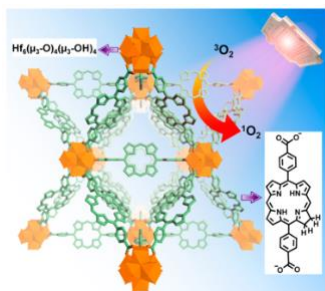


Figure 1.37. Schematic description of singlet oxygen generation by DBC-UiO photosensitization with LED light.<sup>68</sup>

## 1.4.2 Applications in catalysis

In the field of catalysis, the structural characteristics of metalloporphyrin with its excellent electron transfer ability could be used to synthesize the efficient, highly selective, and stable catalysts. With the metalloporphyrin catalysts, the innovative processes are further built for industrial production of hydrocarbon bionic oxidation to promote traditional chemical industry technology.

Metalloporphyrin, which is found in chlorophyll P680, plays an important role in regulating and catalyzing a variety of important biological processes, such as oxygen transport and catalytic oxygen activation in aerobic respiration. While O-O bond formation is the inverse

reaction of O-O bond breakage, theoretically, metalloporphyrin could be used as catalyst for the oxidation of water.

Rui Cao's group was inspired by this and investigated the characteristics of water oxidation using metalloporphyrins and their derivatives. In 2015, they reported a nickel porphyrin catalyst that achieved electrocatalytic water oxidation at an ultra-low overpotential of 184 mV, fully demonstrating the prediction that metalloporphyrins could catalyze water oxidation.<sup>69</sup> In 2019, the group designed another copper porphyrin complex and made significant progress in electrocatalytic water oxidation. As the structure shown in Figure 1.38, a water-soluble copper porphyrin CuTMPyP(OTf)<sub>4</sub> was synthesized.<sup>70</sup> Its peak overpotential for oxygen production from water oxidation in a neutral pH phosphate buffer is determined to be only 310 mV, with a TOF of 30 s<sup>-1</sup>. Previously reported copper molecular compounds for catalytic water oxidation often need strong alkaline solutions and much greater overpotential to function. Therefore, this copper porphyrin catalyst has apparent benefits. Furthermore, it is capable of catalyzing the two-electron generation of H<sub>2</sub>O<sub>2</sub> from the oxidation of water at an acidic pH, which is very rare electrocatalytic water oxidation processes. In general, the neutral and acidic catalytic oxygen formation and hydrogen peroxide creation capabilities of this copper porphyrin would bring fresh ideas for the design of catalysts and studies water oxidation mechanisms.

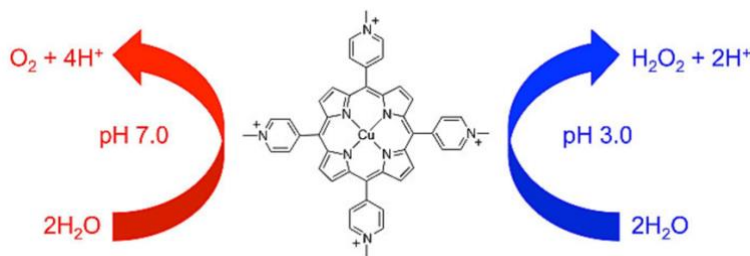


Figure 1.38. Schematic diagram of copper porphyrin electrocatalytic water oxidation.<sup>70</sup>

The reactivity of naturally occurring metalloporphyrin active centers is influenced by the axial ligand and the metal center, which is the “push effect” between these two. When the coordination reaction occurred, the coordination atoms of axial ligand function as electron donors, giving electrons to the d orbitals of porphyrin metal center and modifying its catalytic activity by altering the electronic density states of central metal ion. The existing studies mainly focus on the performance modulation of Fe-N<sub>4</sub> macrocyclic complexes. The central cobalt ion of Co-based catalysts do not participate in the Fenton reaction, so it has theoretically higher stability than Fe-based catalysts, making Co-based ORR catalyst design and performance studies more promising for practical applications.

In 2019, Haibo Ma’s group constructed a model system of cobalt tetramethoxyphenylporphyrin (TMPPCo) monomolecular layer ligated by sulfhydryl ligands, using controlled molecular self-assembly technique on Au electrode surface. The schematic diagram is shown in Figure 1.39. The performance of TMPPCo catalyzed is investigated by ligating various axial ligands in acidic medium for oxygen reduction reaction (ORR).<sup>71</sup>



Figure 1.39. Schematic diagram of Au electrode surface model system construction.<sup>71</sup>

The mechanism of axial ligand modulation of cobalt porphyrin-catalyzed ORR activity is thoroughly studied with theoretical calculations. Three aromatic axial ligands are used in decreasing order of ligand binding strength: 4-mercaptopyridine (MPy) > 4-aminothiophenol

(APT) > 4-mercaptobenzonitrile (MBN). The greatest difference in the spike potential of cobalt porphyrin-catalyzed ORR with each of the three ligands is 80 mV. The catalytic activity increases with the binding strength of ligand, but the axial ligands have no effect on the ORR 2e reaction mechanism. The results of DFT calculations indicate that the introduction of axial ligand alters the charge distribution on the Co(II) center of TMPPCo. It with the energy levels of the frontier molecular orbitals within TMPPCo, together affect the feedback  $\pi$ -bonding between the Co(II) center and the adsorbed O<sub>2</sub>, thus changing the performance of the TMPPCo-catalyzed ORR.

In 2019, Rui Cao's group studied the oxygen reduction characteristics of an asymmetric Pacman-type dinuclear cobalt porphyrin.<sup>72</sup> As shown in Figure 1.40, the group developed an asymmetric dinuclear cobalt porphyrin and made significant progress in electrocatalytic oxygen reduction. The Co<sub>2</sub>TPP-TPFP has a half-wave overpotential  $\eta_{E1/2}$  of 510 mV and a number of transferred electrons  $n$  closes to 3.9. The catalytic spike potential of Co<sub>2</sub>TPP-TPFP is about 60 mV lower than that of Co<sub>2</sub>TPFP.

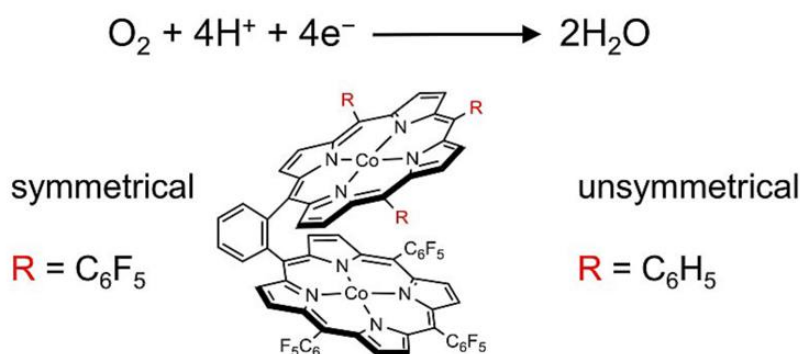


Figure 1.40. Molecular structures of symmetrical and unsymmetrical dinuclear cobalt porphyrins.<sup>72</sup>

The asymmetric dinuclear cobalt porphyrin Co<sub>2</sub>TPP-TPFP, and symmetric dinuclear cobalt porphyrin Co<sub>2</sub>TPFP are synthesized. The oxygen reduction electrochemical properties reveal that the asymmetric dinuclear cobalt porphyrin exhibits significant advantages in the

catalytic ORR process. The analysis suggests that the dinuclear cobalt porphyrin complex has a Pacman structure, and one of the cobalt porphyrin molecules acts as Lewis acid by forming a positive charge during the ORR process, which assists in bonding and activating oxygen molecules. This study demonstrates the benefits of asymmetric dinuclear cobalt porphyrins for catalytic oxygen reduction, which is critical for the development of other catalysts for small molecule activation.

### **1.4.3 Applications in solar energy**

Solar energy is the primary source of energy in our life, and all energy is converted to or from solar energy, either directly or indirectly. Photosynthesis is the primary mechanism in which solar energy is used in nature. Chlorophyll is magnesium porphyrin complex as the major ingredient of photosynthesis in cells. Inspired by this metalloporphyrin complexes have become the leading option for studying artificial photosynthesis.<sup>73,74</sup>

Jing Cao's group modified the self-assembled supramolecules of aminoporphyrin at the grain boundaries of chalcogenide thin films in situ.<sup>75</sup> At the supramolecule-chalcogenide grain interface, the amino porphyrin molecules react with the organic cations in chalcogenide. The resultant ammonium porphyrin complexes efficiently modify the surface of chalcogenide grains, passivate defects, and achieve effective charge extraction. The porphyrin self-assembled supramolecule achieves rapid hole transport for effective charge extraction and transport at the chalcogenide grain boundaries.

The Ni porphyrin self-assembled supramolecular modified chalcogenide solar cell achieves a device efficiency of 24.2%, and the assembled large-area cell device with an active area of 1 cm<sup>2</sup> achieves an efficiency of 22.8%. Also, the assembled cell devices display excellent



water, thermal, and optical stability because to the high hydrophobic characteristics and chemical stability of porphyrin self-assembled supramolecules.

Consumption of vast quantities of fossil fuels has resulted in excessive carbon dioxide emissions. This disrupts the natural carbon balance and results in a slew of energy and environmental problems. The catalytic conversion of CO<sub>2</sub> to value-added compounds under moderate circumstances has emerged as a critical scientific topic. Despite the fact that researchers develop a variety of photocatalytic carbon reduction systems, it is still extremely difficult to combine oxidation and reduction active sites in a single catalyst to achieve both carbon reduction and water oxidation (etc. artificial photosynthesis) at the same time.

With the advantage of crystalline metalloporphyrin porous coordination materials, Qipu Lin's and Jian Zhang's groups assembled a series of iron- and indium-chain-based framework porous materials with a niobium oxide topological network structure thru metallophenolic porphyrin orientation, named Fe/InTCP-Co. When uncoordinated hydroxyl groups were introduced, the corresponding structure named Fe/InTCP-OH-Co, and the artificial photosynthetic properties of such materials were investigated.<sup>76</sup>

The results of photocatalytic carbon reduction experiments demonstrate that this class of materials (without the inclusion of photosensitizers and sacrificial agents) could perform artificial photosynthesis, such as carbon reduction and water oxidation, when exposed to visible light irradiation. The FeTCP-Co has a photocatalytic carbon dioxide reduction efficiency that is 3.7 times that of InTCP-Co. The photocatalytic efficiency is further improved by the introduction of uncoordinated hydroxyl groups into the Fe/InTCP-Co structure. Specifically, for FeTCP-OH-Co, it possesses a photocatalytic efficiency 4.3 times that of FeTCP-Co and a selectivity of 97.8% for the reduced product formic acid. This work provides a revolutionary technique for

designing and synthesizing innovative CO<sub>2</sub> photoreduction catalysts, particularly for the artificial photosynthetic bionanocatalytic materials.

## 1.5 Motivation

Lanthanide near-infrared emitting materials exhibit distinctive photophysical properties, including narrow spectrum bands, large Stokes shifts and long fluorescence lifetimes of milliseconds, which possess great promise for applications in popular fields such as medical diagnostics, imaging and immunoassays. However, because of the Laporte selection rule, the absorption coefficients of lanthanide ions are low, and they must be sensitized with certain chromophores to increase their fluorescence emission properties. Among several chromophores, porphyrin derivatives have garnered considerable interest in recent years because of their excited state energy levels closely matching the energy levels of lanthanide ions for near-infrared emission and could better sensitize lanthanide ions to obtain high near-infrared emission efficiency. In this research, a series of ytterbium(III) complexes with different functionalized porphyrins have been designed and synthesized, as well as porpholactone, with broader absorption in red region for strong emission in near-infrared region.

## **1.6 Objective**

### **Task 1**

Synthesize COOH functionalized porphyrins and ytterbium(III) complexes

Photophysical studies for the synthesized COOH functionalized complexes

### **Task 2**

Synthesize BDP functionalized porphyrins and ytterbium(III) complexes

Photophysical studies for the synthesized BDP functionalized complexes

### **Task 3**

Synthesize tetraphenylporpholactone and optimize the reaction conditions

Photophysical studies for the synthesized tetraphenylporpholactone

# Chapter 2 Experimental

## 2.1 General

### 2.1.1 Materials

All reagents and solutions were commercially purchased and did not require purifications prior to use unless statements were otherwise specified. Dichloromethane (DCM), chloroform (certified ACS approx. 0.75% ethanol as preservative), methanol, hexane (certified ACS various methylpentanes, 4.2% and triethylamine reagent grade) were purchased from Fisher chemical; dichloromethane (spectrophotometric grade, 99.7+%, stab. with amylene), 1,2-dichloroethane (DCE) and sulfolane were purchased from Alfa Aesar; toluene, tetrahydrofuran (99.5%, extra dry over molecular sieve) and chloroform-d (99.8+ atom% D, contains 0.03 v/v% TMS) were purchased from ACROS Organics; dimethyl sulfoxide-d<sub>6</sub> was Purchased from Aldrich. N-Bromosuccinimide (99%), ytterbium (III) acetate hydrate (99.9%), 1,10-phenanthroline monohydrate (99+%), tetrakis(triphenylphosphine)palladium and copper(I) iodide were purchased from Acros Organics; 2,2'-bipyridine (98%) and ruthenium (III) chloride (anhydrous, Ru 47.7% min) were purchased from Alfa Aesar; potassium peroxymonosulfate (> ca. 45%(T) as KHSO<sub>5</sub>) was purchased from Tokyo Chemical Industry Co., Ltd.; sodium hydroxide was purchased from Fisher chemical. 5,15-Dimesityl-porphyrin (DMPH<sub>2</sub>), 5,10,15,20-tetraphenylporphyrin (TPPH<sub>2</sub>), 4-ethynylbenzoic acid and 8-(4-ethynylphenyl)-1,3,5,7-tetramethyl-BODIPY were synthesized in lab before and were characterized by <sup>1</sup>H NMR. Nitrogen and argon gas were provided by Gano Welding (Charleston, IL). The 70-230-mesh silica gel was used for column chromatography.

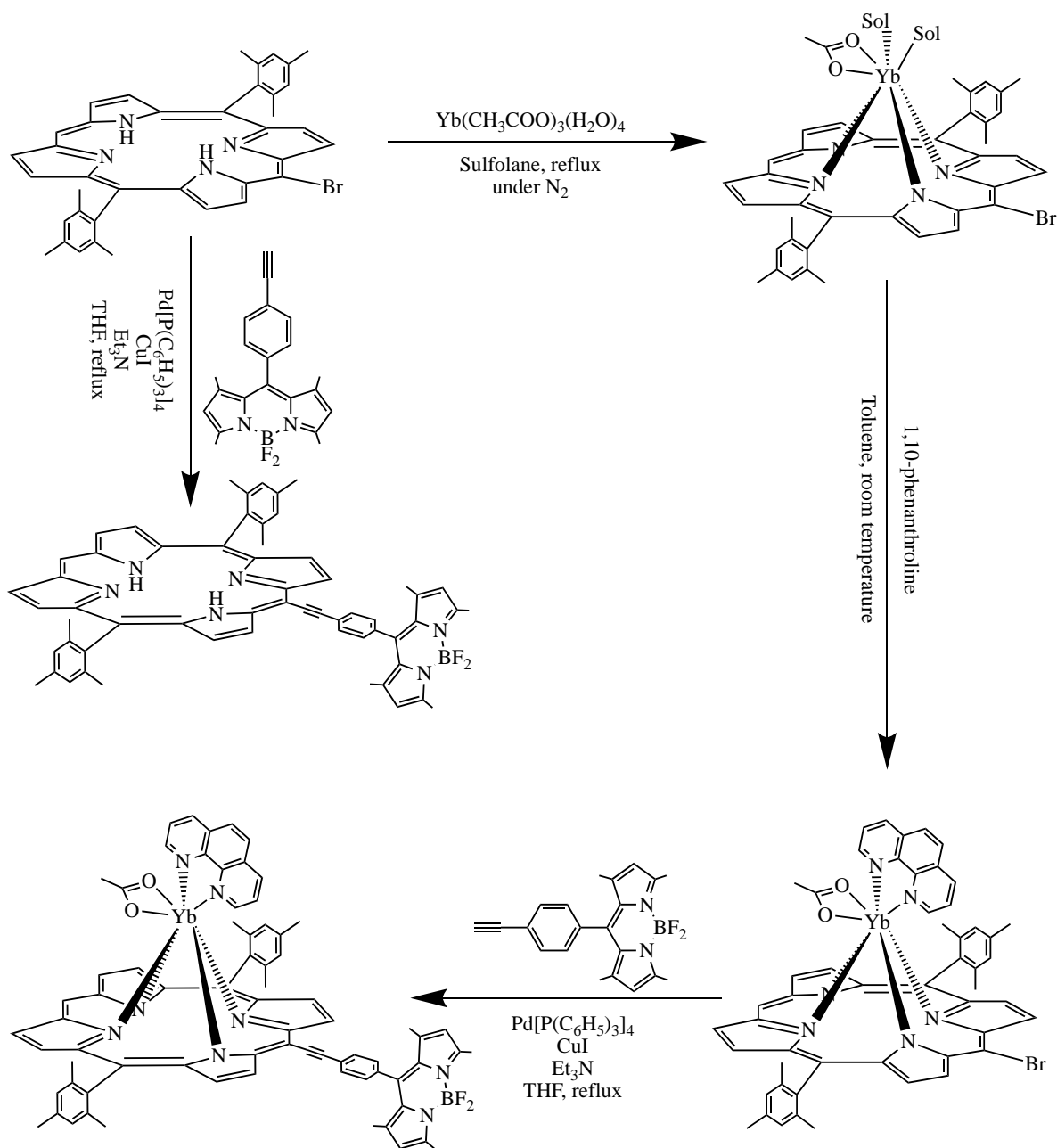
### 2.1.2 Instruments

All  $^1\text{H}$  NMR spectra were collected on a 400 MHz-Bruker Avance FT-NMR spectrometer. The  $\text{CHCl}_3$ -d or dimethyl sulfoxide- $\text{d}_6$  were used as reagent. The acquired  $^1\text{H}$  NMR spectra were processed by the software Bruker's TopSpin 4.1.1, and the identified chemical shifts of signal were reported using the unit part per million (ppm), while the signal splittings were denoted by the following abbreviations: br, broad peak; s, singlet; d, doublet; t, triplet; dd, doublet of doublets, ddd, doublet of doublets of doublets; m, multiplet. All UV-Vis absorption spectra were collected on a Cary 100 Series UV-Vis Dual Beam Spectrophotometer in the wavelength range of 200 – 800 nm, and all the fluorescence spectra including emission spectra and fluorescence lifetime were collected on a FS5 fluorescence spectrometer (Edinburgh Instrument, Inc), with the additional parameters being specified under the spectrum.

## 2.2 Synthesis

### 2.2.1 Synthesis of DMPH<sub>2</sub>-BDP ligand and YbDMP-BDP complexes

The scheme below illustrates the overall synthetic procedures of DMPH<sub>2</sub>-BDP ligand and YbDMP-BDP complex. Details of the synthesis were described in the following section.



Scheme 2.1 Synthetic route for DMPH<sub>2</sub>-BDP ligand and YbDMP-BDP complex.

### 2.2.1.1 Preparation of Br-DMPH<sub>2</sub>

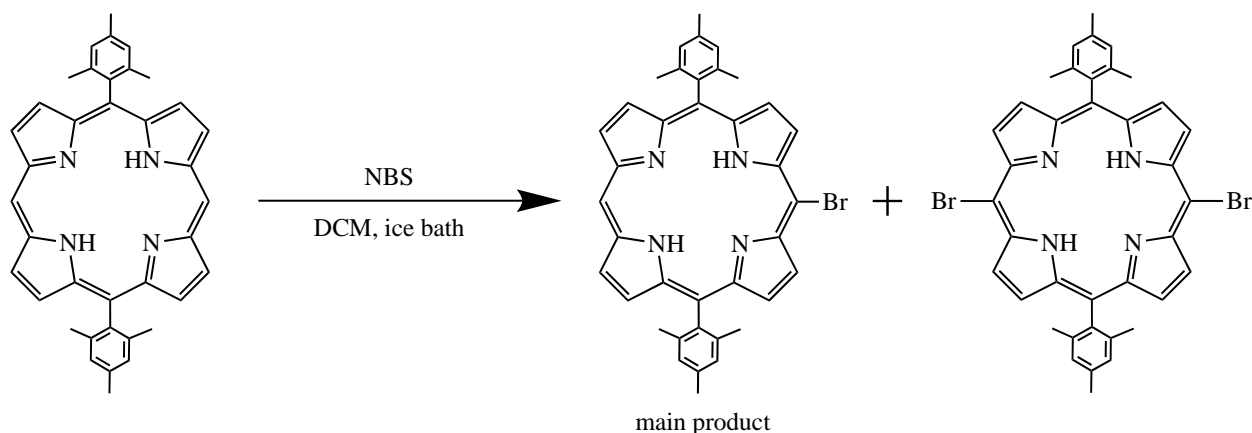


Figure 2.1. Preparation of Br-DMPH<sub>2</sub>.

Table 2.1. Summary of chemicals used in preparation of Br-DMPH<sub>2</sub>.

Reactant/Solvent	Amount used	M.W. (g/mol)	mmol	Equiv.
<b>DMPH<sub>2</sub></b>	0.202 g	546.72	0.369	1.00
<b>NBS</b>	0.106 g	177.99	0.598	1.62
<b>DCM</b>	550 mL			

To a 1000 mL round-bottom flask was added a stir bar, 500 mL DCM and 0.202 g DMPH<sub>2</sub> (0.369 mmol, violet powder). After the flask was set in an ice bath, the solution was stirred for 30 minutes. The NBS solution was prepared by dissolving 0.106 g NBS (0.598 mmol, yellowish powder) in 50 mL DCM in a baker, and the NBS solution was added into DMPH<sub>2</sub> solution dropwise for 40 to 60 minutes using a separation funnel. After NBS solution addition, the flask was capped by a glass stopper. The solution was stirred overnight in ice bath. The DCM solvent was removed by rotary evaporator for future purification.

The Br-DMPH<sub>2</sub> product was separated by column chromatography on silica. The column was packed with wet method and the eluent was DCM:Hexane (1:4). The eluent-soaked silica gel was slowly loaded to 2/3 of the column, then the Br-DMPH<sub>2</sub> crude product was dissolved in minimal amount of eluent and carefully added to the top of silica gel without the destruction of



the surface. The flask was washed 3-4 times with 2-3 pipettes of eluent, and those washes were added into column. After each addition, the solvent level was allowed to descend into the very top of the silica gel. Then 2-3 pipettes of elution were added and descended into column for couple times until it was colorless after adding. The eluent was continuously added to rinse the products out as different bands. After the first and second bands were collected, the eluent was removed by rotary evaporator and solid samples were recrystallized from methanol. The first band Br<sub>2</sub>-DMPH<sub>2</sub> (0.0275 g, 0.0390 mmol, M.W. 704.51 g/mol, yield: 9.89%, violet powder) and second band Br-DMPH<sub>2</sub> (0.226 g, 0.361 mmol, yield: 97.8%, violet) were collected by filtration.

#### 2.2.1.2 Preparation of Br-YbDMP(OAc)(Sol)<sub>2</sub>

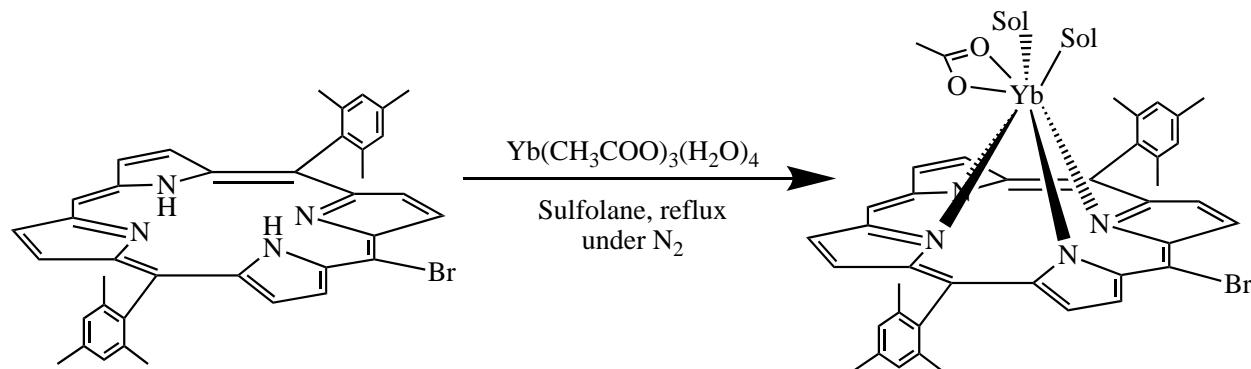


Figure 2.2. Preparation Br-YbDMP(OAc)(Sol)<sub>2</sub>.

Table 2.2. Summary of chemicals used in preparation of Br-YbDMP(OAc)(Sol)<sub>2</sub>.

Reactant/Solvent	Amount used	M.W. (g/mol)	mmol	Equiv.
Br-DMPH <sub>2</sub>	0.203 g	625.61	0.324	1.00
Yb(CH <sub>3</sub> COO) <sub>3</sub> (H <sub>2</sub> O) <sub>4</sub>	0.202 g	422.25	0.479	1.50
Sulfolane	40 mL			

To a 50 mL Schlenk flask equipped with a condenser was added a stir bar, Br-DMPH<sub>2</sub> (0.203 g, 0.324 mmol, violet powder), Yb(CH<sub>3</sub>COO)<sub>3</sub>(H<sub>2</sub>O)<sub>4</sub> (0.202 g, 0.479 mmol, clear crystal) and sulfolane (40 mL). The flask was placed on a heating block with the temperature of heating

plate was set to 410 °C. The reaction mixture was stirred and refluxed under nitrogen for 40 minutes, then left for naturally cooling down to room temperature while being stirred overnight. To the reaction mixture was added 30 mL DCM, then the resulting solution was washed by water (300 mL each time and for 3 times). The organic layer was collected, and solvent was removed by rotary evaporator for further purification.

Following the purification procedures mentioned in Section 2.2.1.1, the Br-YbDMP(OAc)(Sol)<sub>2</sub> crude product was purified through column chromatography on silica with elution by DCM first, after first band unreacted Br-DMPH<sub>2</sub> rinsed, the elution was changed to DCM:Methanol (200:30), and the second band was collected. The eluent was removed and Br-YbDMP(OAc)(Sol)<sub>2</sub> product (0.123 g, 0.134 mmol, yield: 41.27% ,violet powder) was recrystallized from methanol and collected through filtration.

### 2.2.1.3 Preparation of Br-YbDMP(OAc)(Phen)

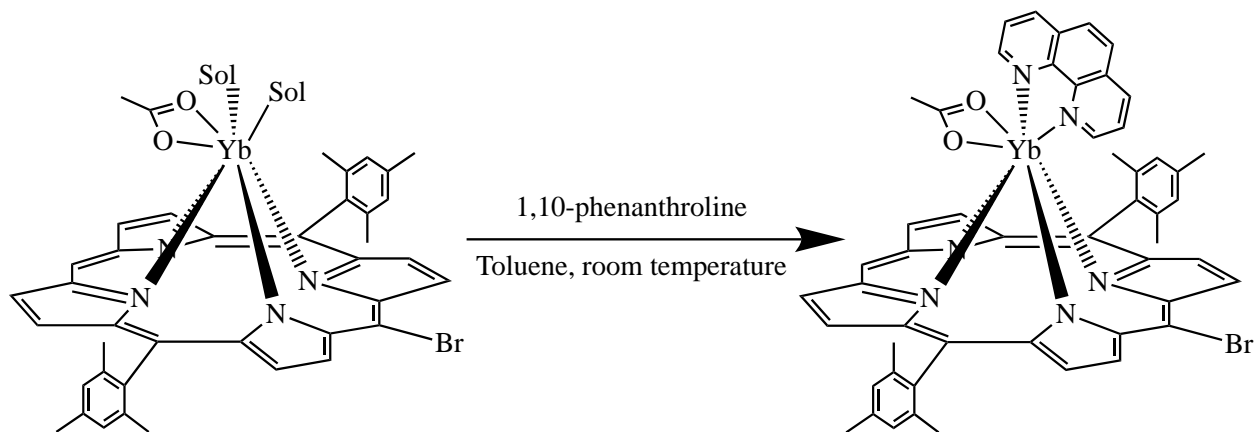


Figure 2.3. Preparation of Br-YbDMP(OAc)(Phen).

Table 2.3. Summary of chemicals used in preparation of Br-YbDMP(OAc)(Phen).

Reactant/Solvent	Amount used	M.W. (g/mol)	mmol	Equiv.
<b>Br-YbDMP(OAc)(Sol)<sub>2</sub></b>	0.123 g	919.78	0.134	1.00
<b>1,10-phenanthroline</b>	0.0285 g	180.21	0.158	1.23
<b>Toluene</b>	40 mL			

To a round bottom flask equipped with a Findenser was added a stir bar, Br-YbDMP(OAc)(Sol)<sub>2</sub> (0.123 g, 0.134 mmol, violet powder), 1,10-phenanthroline (0.0285 g, 0.158 mmol, white powder) and toluene (40 mL). The reaction mixture was stirred overnight at room temperature. The solvent was removed by rotary evaporator and the product recrystallized from DI water, solid product Br-YbDMP(OAc)(Phen) (0.137 g, 0.132 mmol, yield: 98.6%, violet solid) was collected through filtration.

#### 2.2.1.4 Synthesis of YbDMP-BDP

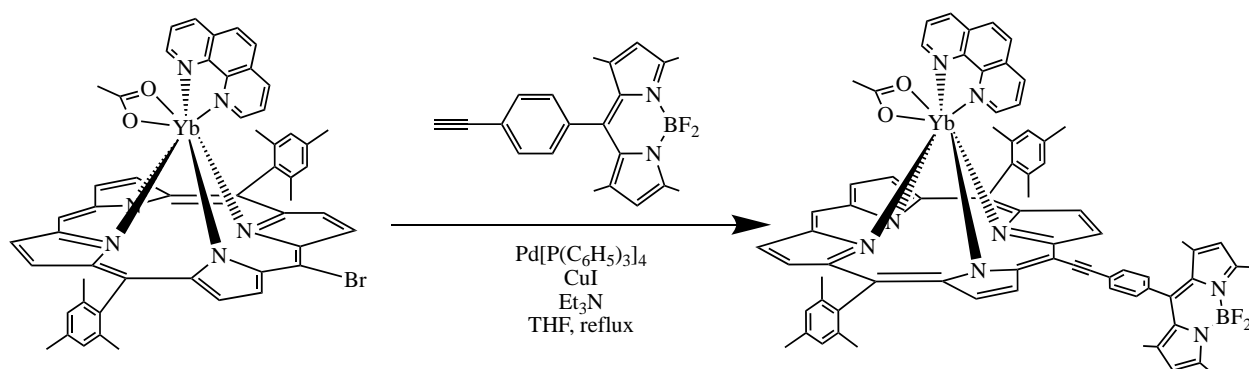


Figure 2.4. Synthesis of YbDMP-BDP.

Table 2.4. Summary of chemicals used in preparation of YbDMP-BDP.

Reactant/Solvent	Amount used	M.W. (g/mol)	mmol	Equiv.
Br-YbDMP(OAc)(Phen)	0.100 g	1035.91	0.0965	1.00
BODIPY derivative	0.0750 g	438.20	0.171	1.70
Pd(PPh <sub>3</sub> ) <sub>4</sub>	0.0056 g	1155.59	0.00485	4.8%
Copper(I) iodide	0.0010 g	190.45	0.00525	5.2%
Triethylamine	4 mL			
Dry tetrahydrofuran	20 mL			

To a 50 mL pressure tube was added a stir bar, Br-YbDMP(OAc)(Phen) (0.100 g, 0.0965 mmol, violet powder), 8-(4-ethynylphenyl)-1,3,5,7-tetramethyl-BODIPY (0.0750 g, 0.171 mmol, orange solid), tetrakis(triphenylphosphine)palladium (Pd(PPh<sub>3</sub>)<sub>4</sub>, 0.0056 g, 0.00485 mmol, 4.8%, light yellow crystal), copper(I) iodide (CuI, 0.0010 g, 0.00525 mmol, 5.2%, white powder),

triethylamine (Et<sub>3</sub>N, 4 mL) and dry tetrahydrofuran (THF, 20 mL). This procedure was performed inside an Ar-filled glovebox. The pressure tube was then sealed and transferred outside the glovebox, and the solution was stirred to reflux at 80 °C for two days. After the reaction mixture cooling down to room temperature, the solvent was removed by rotary evaporator.

Following the purification procedures mentioned in Section 2.2.1.1, the YbDMP-BDP crude product was purified through column chromatography on silica with elution by DCM first. After first band rinsed, the eluent was changed to DCM:Methanol (100:3), the major band (third band) was collected as YbDMP(OAc)(Phen)-BODIPY product. The eluent was removed by rotary evaporator, and the YbDMP(OAc)(Phen)-BODIPY product (30.0 mg, 0.0230 mmol, yield: 23.8%, dark green solid) was recrystallized from methanol and collected by filtration.

#### 2.2.1.5 Synthesis of DMPH<sub>2</sub>-BDP

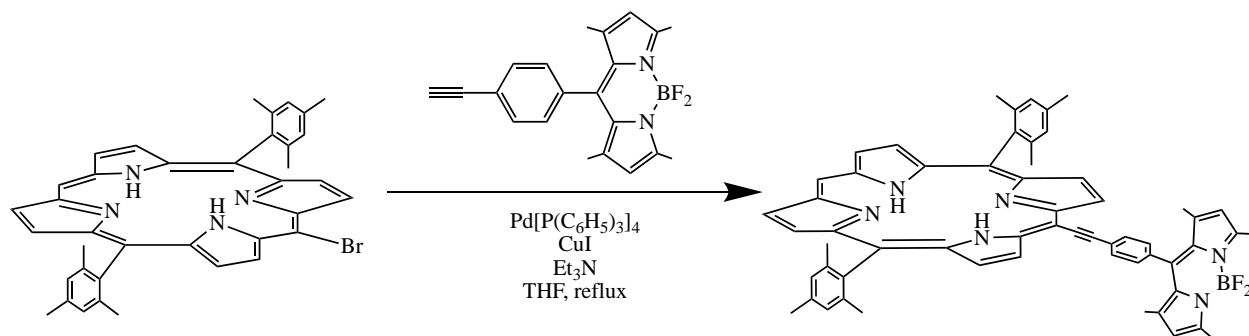


Figure 2.5. Synthesis of DMPH<sub>2</sub>-BDP.

Table 2.5. Summary of chemicals used in preparation of DMPH<sub>2</sub>-BDP.

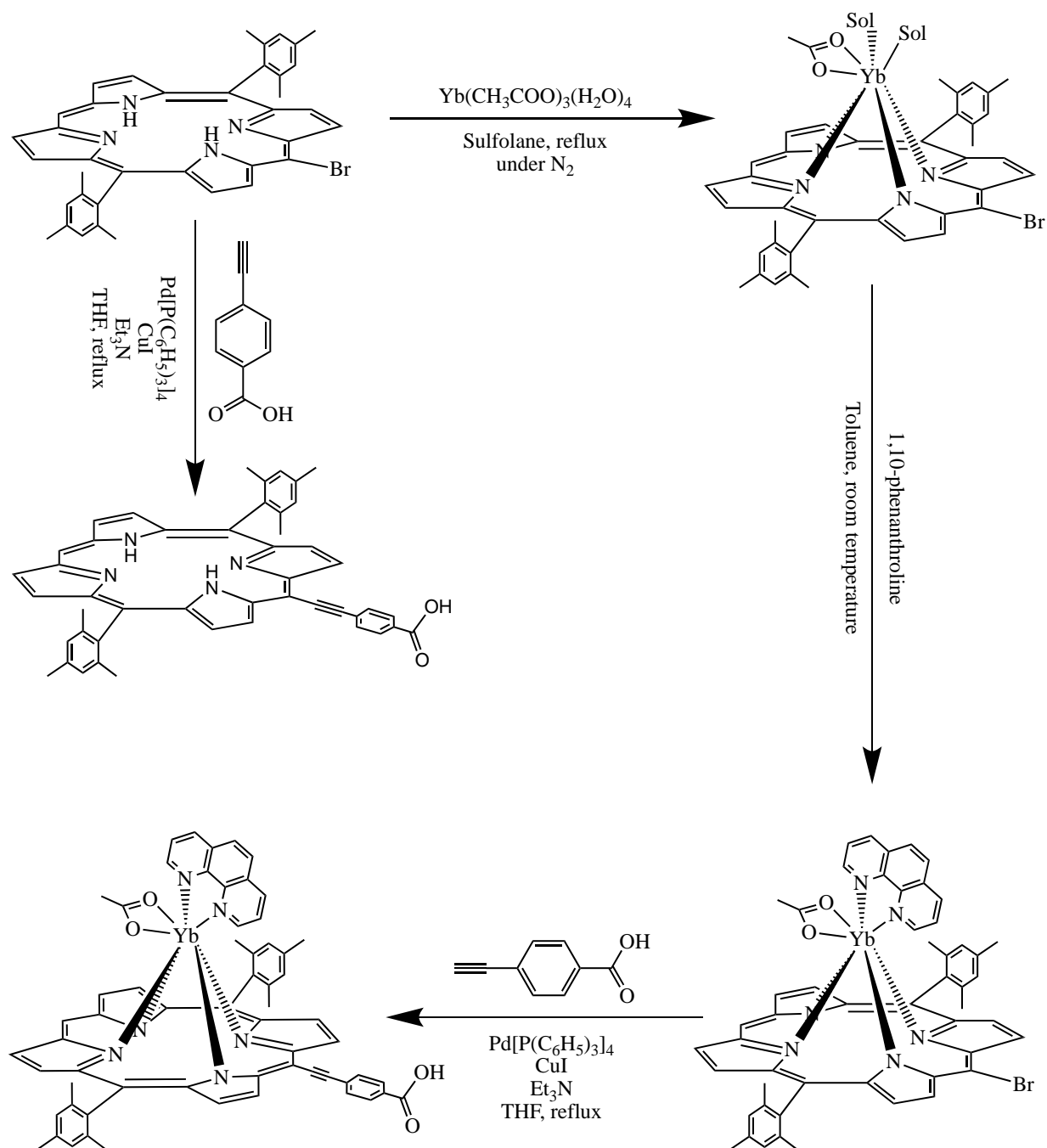
Reactant/Solvent	Amount used	M.W. (g/mol)	mmol	Equiv.
<b>Br-DMPH<sub>2</sub></b>	0.100 g	625.61	0.160	1.00
<b>BODIPY derivative</b>	0.111 g	348.20	0.319	2.00
<b>Pd(PPh<sub>3</sub>)<sub>4</sub></b>	0.0100 g	1155.59	0.00865	5.4%
<b>Copper(I) iodide</b>	0.0016 g	190.45	0.00840	5.3%
<b>Triethylamine</b>	4 mL			
<b>Dry tetrahydrofuran</b>	20 mL			

To a 50 mL pressure tube was added a stir bar, Br-DMPH<sub>2</sub> (0.100 g, 0.160 mmol, violet powder), 8-(4-ethynylphenyl)-1,3,5,7-tetramethyl-BODIPY (0.111 g, 0.319 mmol, orange powder), Pd(PPh<sub>3</sub>)<sub>4</sub> (0.0100 g, 0.00865 mmol, light yellow crystal), CuI (0.0016 g, 0.00840 mmol, white powder), Et<sub>3</sub>N (4 mL) and dry THF (20 mL). This procedure was performed inside an Ar-filled glovebox. The pressure tube was then sealed and transferred outside the glovebox, and the solution was stirred to reflux at 80 °C for two days. After cooling down to the room temperature, the solvent was removed by rotary evaporator.

Following the purification procedures mentioned in Section 2.2.1.1, the DMPH<sub>2</sub>-BODIPY crude product was purified through column chromatography on silica with elution by DCM:Hexane (1:1). After first band unreacted DMPH<sub>2</sub> was flushed, the major band (second band) collected. The eluent was removed by rotary evaporator and DMPH<sub>2</sub>-BODIPY product (87 mg, 0.0975 mmol, yield: 61.0%, dark green solid) was recrystallized from methanol and collected by filtration. <sup>1</sup>H NMR for DMPH<sub>2</sub>-BDP (400.13 MHz, CDCl<sub>3</sub>) δ 10.072 (s, 1H, <sup>a</sup>H), 9.755-9.743 (d, 2H, <sup>b</sup>H), 9.208-9.197 (d, 2H, <sup>c</sup>H), 8.812-8.800 (d, 2H, <sup>e</sup>H), 8.746-8.735 (d, 2H, <sup>d</sup>H), 8.151-8.131 (d, 2H, <sup>f</sup>H), 7.501-7.480 (d, 2H, <sup>g</sup>H), 7.301 (s, 4H, <sup>h</sup>H), 6.034 (s, 2H, <sup>m</sup>H), 2.640 (s, 6H, <sup>i</sup>H), 2.584 (s, 6H, <sup>l</sup>H), 1.841 (s, 12H, <sup>j</sup>H), 1.575 (s, 6H, <sup>k</sup>H), -2.602 (s, 2H, <sup>n</sup>H).

## 2.2.2 Synthesis of DMPH<sub>2</sub>-COOH ligand and YbDMP-COOH complexes

The figure below illustrates the overall synthetic procedures of DMPH<sub>2</sub>-COOH ligand and YbDMP-COOH complex. Details of the synthesis are described in the following section.



Scheme 2.2. Synthetic route for DMPH<sub>2</sub>-COOH ligand and YbDMP-COOH complex.

### 2.2.2.1 Synthesis of YbDMP-COOH

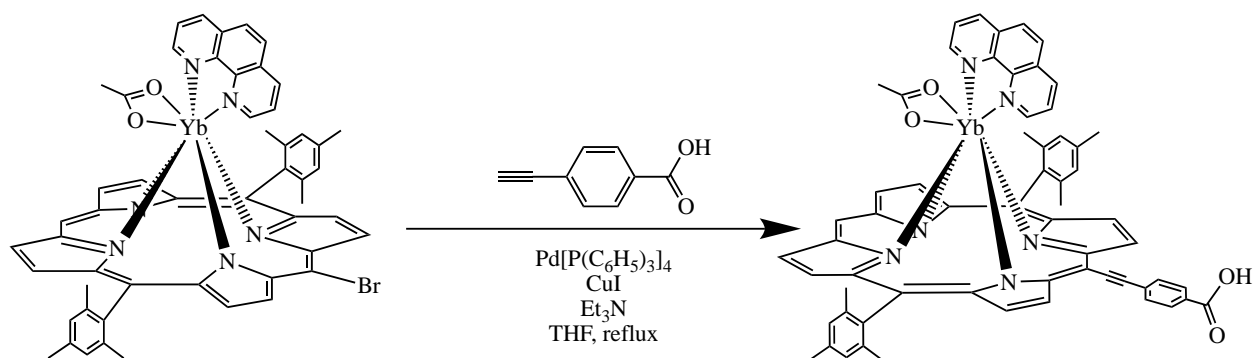


Figure 2.6. Synthesis of YbDMP-COOH.

Table 2.6. Summary of chemicals used in preparation of YbDMP-COOH.

Reactant/Solvent	Amount used	M.W. (g/mol)	mmol	Equiv.
<b>Br-YbDMP(OAc)(Phen)</b>	0.0497 g	1035.91	0.0480	1.00
<b>COOH derivative</b>	0.0070 g	146.15	0.0479	1.00
<b>Pd(PPh<sub>3</sub>)<sub>4</sub></b>	0.0030 g	1155.59	0.00260	5.4%
<b>Copper(I) iodide</b>	0.0010 g	190.45	0.00520	10.8%
<b>Triethylamine</b>	4 mL			
<b>Dry tetrahydrofuran</b>	20 mL			

The Br-YbDMP(OAc)(Sol)<sub>2</sub> and Br-YbDMP(OAc)(Phen) were synthesized by following the procedures described in Section 2.2.1.2-2.2.1.3.

To a 50 mL pressure tube was added a stir bar, Br-YbDMP(OAc)(Phen) (0.0497 g, 0.0480 mmol, violet powder), 4-ethynylbenzoic acid (0.0700 g, 0.0479 mmol, white solid), Pd(PPh<sub>3</sub>)<sub>4</sub> (0.0030g, 0.00260 mmol, light yellow crystal), CuI (0.0010 g, 0.00520 mmol, white powder), Et<sub>3</sub>N (4 mL) and dry THF (20 mL). This procedure was performed inside an Ar-filled glovebox. The pressure tube was then sealed and transferred outside the glovebox, and the solution was stirred and refluxed at 80 °C for two days. After cooling down to the room temperature, the solvent was removed by rotary evaporator.

Following the purification procedures mentioned in Section 2.2.1.1, the YbDMP(OAc)(Phen)-COOH crude product was purified through column chromatography on silica with elution by DCM:Methanol (100:2). The major band (second band) was collected as product. The YbDMP-COOH product (14 mg, 0.0127 mmol, yield: 26.5%, dark green solid) was recrystallized from Methanol and collected by filtration.

#### 2.2.2.2 Synthesis of DMPH<sub>2</sub>-COOH

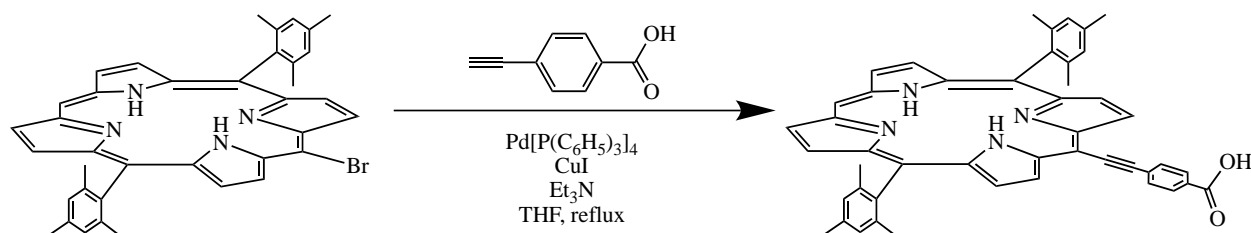


Figure 2.7. Synthesis of DMPH<sub>2</sub>-COOH.

Table 2.7. Summary of chemicals used in preparation of DMPH<sub>2</sub>-COOH.

Reactant/Solvent	Amount used	M.W. (g/mol)	mmol	Equiv.
<b>Br-DMPH<sub>2</sub></b>	0.100 g	625.61	0.160	1.00
<b>COOH derivative</b>	0.0460 g	146.15	0.315	1.94
<b>Pd(PPh<sub>3</sub>)<sub>4</sub></b>	0.0100 g	1155.59	0.00865	5.4%
<b>Copper(I) iodide</b>	0.0016 g	190.45	0.00840	5.2%
<b>Triethylamine</b>	4 mL			
<b>Dry tetrahydrofuran</b>	20 mL			

To a 50 mL pressure tube was added a stir bar, Br-DMPH<sub>2</sub> (0.100 g, 0.160 mmol, violet powder), 4-ethynylbenzoic acid (0.0460 g, 0.315 mmol, white solid), 0.0100g Pd(PPh<sub>3</sub>)<sub>4</sub> (0.00865 mmol, light yellow crystal), CuI (0.0016 g, 0.00840 mmol, white powder), Et<sub>3</sub>N (4 mL) and dry THF (20 mL). This procedure was performed inside an Ar-filled glovebox. The pressure tube was then sealed and transferred outside the glovebox, and the solution was stirred and refluxed at 80 °C for two days. After cooling down to the room temperature, the solvent was removed by rotary evaporator.



Following the purification procedures mentioned in Section 2.2.1.1, the DMPH<sub>2</sub>-COOH crude product was purified through column chromatography on silica with elution by DCM:Methanol (200:1). After the first band unreacted DMPH<sub>2</sub> was flushed, the major band (second band) was collected as product. The DMPH<sub>2</sub>-COOH product (30 mg, 0.0434 mmol, yield: 27.2%, dark green solid) was recrystallized from methanol and collected by filtration. <sup>1</sup>H NMR for DMPH<sub>2</sub>-COOH (400.13 MHz, DMSO) δ 13.238 (s, 1H, <sup>1</sup>H), 10.463 (s, 1H, <sup>a</sup>H), 9.856-9.844 (d, 2H, <sup>b</sup>H), 9.510-9.501 (d, 2H, <sup>c</sup>H), 8.765-8.754 (d, 2H, <sup>e</sup>H), 8.681-8.671 (d, 2H, <sup>d</sup>H), 8.280-8.260 (d, 2H, <sup>f</sup>H), 8.201-8.181 (d, 2H, <sup>g</sup>H), 7.398 (s, 4H, <sup>h</sup>H), 2.624 (s, 6H, <sup>i</sup>H), 1.792 (s, 12H, <sup>j</sup>H), -2.602 (s, 2H, <sup>k</sup>H).

### 2.2.3 Synthesis of YbDMP as reference

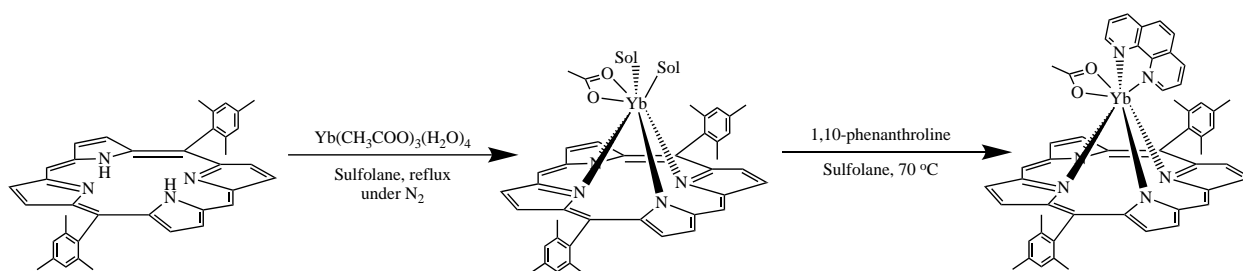


Figure 2.8. Synthesis of YbDMP.

Table 2.8. Summary of chemicals used in preparation of YbDMP.

Reactant/Solvent	Amount used	M.W. (g/mol)	mmol	Equiv.
DMPH <sub>2</sub>	0.220 g	546.72	0.402	1.00
Yb(CH <sub>3</sub> COO) <sub>3</sub> (H <sub>2</sub> O) <sub>4</sub>	0.210 g	422.25	0.497	2.50
1,10-phenanthroline	0.160 g	180.21	0.888	4.45
Sulfolane	20 mL			

To a 50 mL Schlenk flask equipped with a Findenser was added a stir bar, DMPH<sub>2</sub> (0.220 g, 0.402 mmol, violet powder), Yb(CH<sub>3</sub>COO)<sub>3</sub>(H<sub>2</sub>O)<sub>4</sub> (0.210 g, 0.497 mmol, clear crystal) and sulfolane (20 mL). The flask was placed on a heating block and the temperature of heating plate was set up to 410 °C. The reaction mixture was stirred at reflux under nitrogen for 45 minutes,

then allowed to cool down to 70 °C. The 0.160 g 1,10-phenanthroline (0.888 mmol, white powder) was added into the reaction mixture and stirred overnight. To the reaction mixture was added 30 mL DCM. Then the resulting solution was washed by water (300 mL each time and for 3 times). The organic layer was collected, and solvent was removed by rotary evaporator for further purification.

Following the purification procedures mentioned in Section 2.2.1.1, the YbDMP(OAc)(Phen) crude product was purified through column chromatography on silica with elution by DCM first. After first band unreacted Br-DMPH<sub>2</sub> was rinsed, the eluent was changed to DCM:Methanol (100:5), and the second band was collected. The elution was removed and YbDMP(OAc)(Phen) product (0.140 g, 0.146 mmol, yield: 36.4%, violet powder) was recrystallized from methanol and collected through filtration.

## 2.2.4 Synthesis of TPLH<sub>2</sub> ligand

General procedure for synthesis of 5,10,15,20-tetraphenylporpholactone (TPLH<sub>2</sub>) was shown in Figure 2.8.

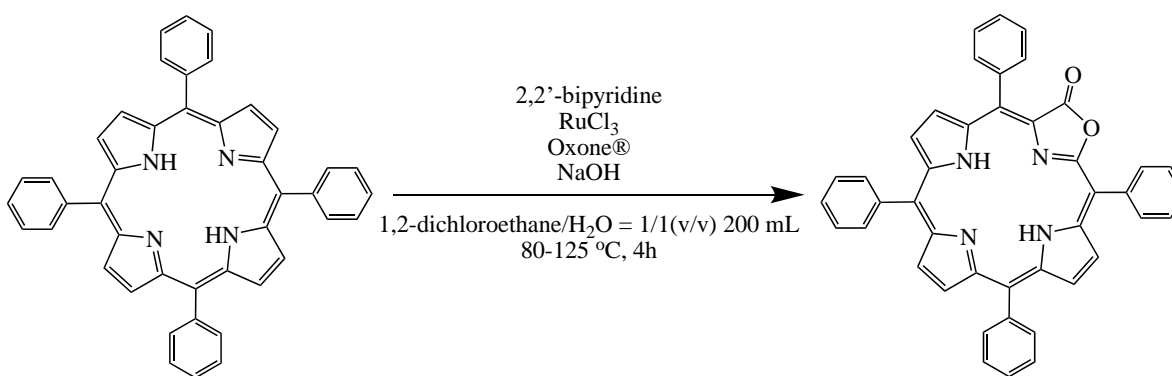


Figure. 2.9. Synthesis of TPLH<sub>2</sub>.

Table 2.9. Summary of chemicals used in preparation of TPLH<sub>2</sub>.

Reactant/Solvent	Amount used	M.W. (g/mol)	mmol	Equiv.
TPPH <sub>2</sub>	0.639 g	614.75	1.04	1.00
2,2'-bipyridine	0.0500 g	156.19	0.320	30.8 %

<b>RuCl<sub>3</sub></b>	0.0604 g	207.43	0.291	27.9 %
<b>Oxone®</b>	6.93 g	614.74	11.3	10.85
<b>NaOH</b>	0.620 g	40.00	15.5	14.89
<b>DCE</b>	100 mL			
<b>DI water</b>	100 mL			

To a 250 mL three-neck round bottom flask equipped with a Findenser was added a stir bar, 5,10,15,20-tetraphenylporphyrin (TPPH<sub>2</sub>, 0.639 g, 1.04 mmol, violet powder), 2,2'-bipyridine (0.0500 g, 0.320 mmol, clear crystal) and DCE (100 mL). The flask was placed in oil bath, and the mixture was stirred to dissolve. When temperature reached to 100 °C, ruthenium (III) chloride (RuCl<sub>3</sub>, 0.0604 g, 0.291 mmol, dark-brown powder) dissolved in DI water (60 mL) was added into the flask and heating to reflux, the temperature of reaction mixture was maintained at 100 °C. The potassium peroxymonosulfate (Oxone®, 6.93 g, 11.3 mmol, off-white powder) and sodium hydroxide (NaOH, 0.620 g, 15.5 mmol, white opaque crystals) were dissolved in DI water (40 mL) and added into the flask dropwise over 40 minutes. The reaction mixture was stirred and refluxed for 4 hours. After the reaction mixture cooling to room temperature, the organic layer was collected, and solvent was removed by rotary evaporator.

The TPLH<sub>2</sub> crude product was purified through column chromatography on silica with elution by Chloroform:Hexane (1:1), the second band was collected. The eluent was removed by rotary evaporator. The TPLH<sub>2</sub> product (0.128 g, 0.202 mmol, yield: 19.4%, violet powder) was recrystallized from methanol and collected through filtration. <sup>1</sup>H NMR for TPLH<sub>2</sub> (400.13 MHz, CDCl<sub>3</sub>) δ 8.773-8.729 (ddd, 2H, <sup>a</sup>H), 8.679-8.667 (dd, 1H, <sup>d</sup>H), 8.574-8.540 (m, 2H, <sup>b</sup>H), 8.506-8.495 (d, 1H, <sup>c</sup>H), 8.121-8.062 (m, 6H, <sup>f</sup>H), 7.959-7.935 (dd, 2H, <sup>f</sup>H), 7.729-7.710 ppm (m, 12H, <sup>e</sup>H&<sup>e'</sup>H), -1.695(s, 1H, <sup>h</sup>H), -2.064 (s, 1H, <sup>g</sup>H).

## 2.3 Photophysical measurements

### 2.3.1 Stock solutions

For the DMPH<sub>2</sub>-BDP stock solution, to a 25 mL volumetric flask with 0.0011 g DMPH<sub>2</sub>-BDP, dichloromethane (DCM, spectrophotometric grade) was added to the marked line on the neck of flask, then the flask was capped and sealed, and inverted several times until all the solid dissolved. The final concentration for DMPH<sub>2</sub>-BDP stock solution was  $4.93 \times 10^{-5}$  M.

Following the same procedures, the amount added for ligands, complexes and references and final concentrations of stock solutions were listed in the table 2.10.

Table 2.10. Concentrations of stock solutions.

Stock solution	Amount added (g)	DCM (mL)	Concentration (M)
DMPH <sub>2</sub> -BDP	0.0011	25.0	$4.93 \times 10^{-5}$
YbDMP-BDP	0.0016	25.0	$4.91 \times 10^{-5}$
DMPH <sub>2</sub> -COOH	0.0006	25.0	$3.47 \times 10^{-5}$
YbDMP-COOH	0.0010	25.0	$3.49 \times 10^{-5}$
TPLH <sub>2</sub>	0.0080	25.0	$5.06 \times 10^{-5}$
TPPH <sub>2</sub>	0.0078	25.0	$5.08 \times 10^{-5}$
YbTPPTpH	0.0055	25.0	$2.20 \times 10^{-5}$
YbDMP	0.0008	25.0	$3.51 \times 10^{-5}$

### 2.3.2 UV-Vis absorption spectra in solution

The UV-Vis absorption spectra were measured for synthesized ligands, complexes and references by Cary 100 Series UV-Vis Dual Beam Spectrophotometer with 10 mm capped quartz glass cuvette cell. Baseline corrections were collected before measurements.

To a 10 mm capped quartz glass cuvette cell was added 500  $\mu$ L of DMPH<sub>2</sub>-BDP stock solution and 2.5 mL DCM, and the final concentration was  $8.21 \times 10^{-6}$ . The UV-Vis absorption spectrum for DMPH<sub>2</sub>-BDP was recorded from 200-800 nm.

Following the same procedures, the amount added for each ligand, complex and reference and final concentrations of absorption solutions were listed in the table 2.11. According to Beer-Lambert law, the molar absorptivity of each peak could be calculated through the formula  $A = \epsilon \cdot l \cdot C$ , while A was absorbance,  $\epsilon$  was molar absorptivity, l was length of light path, which was 1 cm in this research, and C was concentration.

Table 2.11. Concentrations of solutions prepared for absorption.

Solution for Abs	Amount added ( $\mu\text{L}$ )	DCM (mL)	Concentration (M)
<b>DMPH<sub>2</sub>-BDP</b>	500	2.5	$8.21 \times 10^{-6}$
	190	2.5	$3.48 \times 10^{-6}$
<b>YbDMP-BDP</b>	500	2.5	$8.18 \times 10^{-6}$
	190	2.5	$3.47 \times 10^{-6}$
<b>DMPH<sub>2</sub>-COOH</b>	280	2.5	$3.50 \times 10^{-6}$
<b>YbDMP-COOH</b>	280	2.5	$3.51 \times 10^{-6}$
<b>TPLH<sub>2</sub></b>	100	2.5	$1.95 \times 10^{-5}$
<b>TPPH<sub>2</sub></b>	100	2.5	$1.95 \times 10^{-5}$
<b>YbDMP</b>	280	2.5	$3.54 \times 10^{-6}$

### 2.3.3 Fluorescence emission spectra in solution

The fluorescence emission spectra were measured for synthesized ligands and complexes by Edinburgh spectrofluorometer FS5 using steady-state excitation with a xenon arc lamp as light source. The fluorescence emission spectra for ligands were recorded from 600-800 nm in visible range with the excitation at 556 nm. The fluorescence emission spectra for complexes were recorded from 600-800 nm in visible region with the excitation at 556 nm and 900-1150 nm in NIR region with the excitation at various excitation wavelength. The concentration of ligands and complexes were kept the same as in stock solutions or in absorption measurements.

### 2.3.4 Quantum yields

The quantum yields were evaluated for synthesized ligands and complexes following the equation:

$$\Phi_X = \Phi_{ST} \left( \frac{\text{Grad}_X}{\text{Grad}_{ST}} \right) \left( \frac{\eta_X^2}{\eta_{ST}^2} \right),$$

Where  $\Phi_{ST}$  is the fluorescence quantum yield of the standard;  $\text{Grad}_X$  and  $\text{Grad}_{ST}$  are the gradient from the plot of integrated fluorescence emission intensity vs. absorbance of the complex and standard, respectively;  $\eta_X$  and  $\eta_{ST}$  are the refractive indexes of standard's and complex's solvent, respectively. (Section 1.3.3.)

For the quantum yields measurements of ligands, the TPPH<sub>2</sub> in DCM was used as standard ( $\Phi_{ST} = 0.62$ ,  $\lambda_{ex} = 556$  nm) for visible emission.<sup>77</sup> For the quantum yields measurements of complexes, the YbTPPTpH in DCM was used as standard ( $\Phi_{ST} = 0.032$ ,  $\lambda_{ex} = 556$  nm) for NIR emission.<sup>78</sup>

For the preparation of DMPH<sub>2</sub>-BDP solution with gradient concentrations, to a 10 mm cuvette with 2.50 mL DCM, was added 80  $\mu$ L, 160  $\mu$ L, 240  $\mu$ L, 320  $\mu$ L and 380  $\mu$ L DMPH<sub>2</sub>-BDP stock solution respectively. The UV-Vis absorption (from 300-700 nm) and fluorescence emission spectra (from 600-800 for visible region and 900-1150 nm for NIR region,  $\lambda_{ex} = 556$  nm) were measured.

Following the same procedures, the ligands and complexes solutions with gradient concentrations were prepared and listed in section 3.3.3, and the UV-Vis absorption and fluorescence emission spectra were recorded. The integrated fluorescence emission intensities were calculated by the software SciDAVis 1.25.1, and the quantum yields were calculated by the equation mentioned above.

# Chapter 3 Results and Discussion

## 3.1 Characterization

### 3.1.1 $^1\text{H}$ NMR spectroscopy

#### 3.1.1.1 $^1\text{H}$ NMR for DMPH<sub>2</sub>-BDP

The DMPH<sub>2</sub>-BDP ligand is characterized by  $^1\text{H}$  NMR, this spectrum is illustrated in the Figure 3.1.

The singlet peak at 10.072 ppm indicates the *meso*-position **a** of the methine bridge, the integration of 1.00 proves this. The four sets of doublet peaks at 9.755-9.743 ppm, 9.208-9.197 ppm, 8.812-8.800 ppm and 8.746-8.735 ppm indicate  $\beta$ -positions **b**, **c**, **e** and **d** on the pyrrolic rings, the integrations of 1.95, 1.98, 2.12 and 1.93 prove the symmetry structure of DMPH<sub>2</sub>-BDP ligand. The singlet peak at 7.301 ppm indicates the four *meta* positions **h** of two phenyl rings, the integration of 4.09 proves this. The singlet peak at 2.640 ppm indicates the two methyl groups **i** at *para* positions of two phenyl rings and the singlet peak at 1.841 ppm indicates the four methyl groups **j** at four *ortho* positions of two phenyl rings, also the integrations of 6.16 and 12.00 also prove these. The singlet peak at -2.457 ppm indicates the two NH positions **n** and the integration is 2.23.

The two sets of doublet peaks at 8.151-8.131 ppm and 7.501-7.480 ppm indicate the two *ortho* and *meta* positions **f**, **g** of the phenyl in BODIPY derivative with the integrations as 2.03 and 2.22. The two sets of singlet peak at 2.584 ppm and 1.575 ppm indicate the methyl position **l**, **k** in BODIPY derivative, the integrations of 6.16 and 5.83 also prove these. While the singlet peak at 6.034 ppm indicates the position **m** of methine bridge in BODIPY derivative and the integration is 2.01. From this  $^1\text{H}$  NMR spectrum, the characteristic peaks of DMPH<sub>2</sub>-BDP ligand

are shown, and there are no peaks from impurities, which mean the DMPH<sub>2</sub>-BDP ligand has been successfully synthesized.



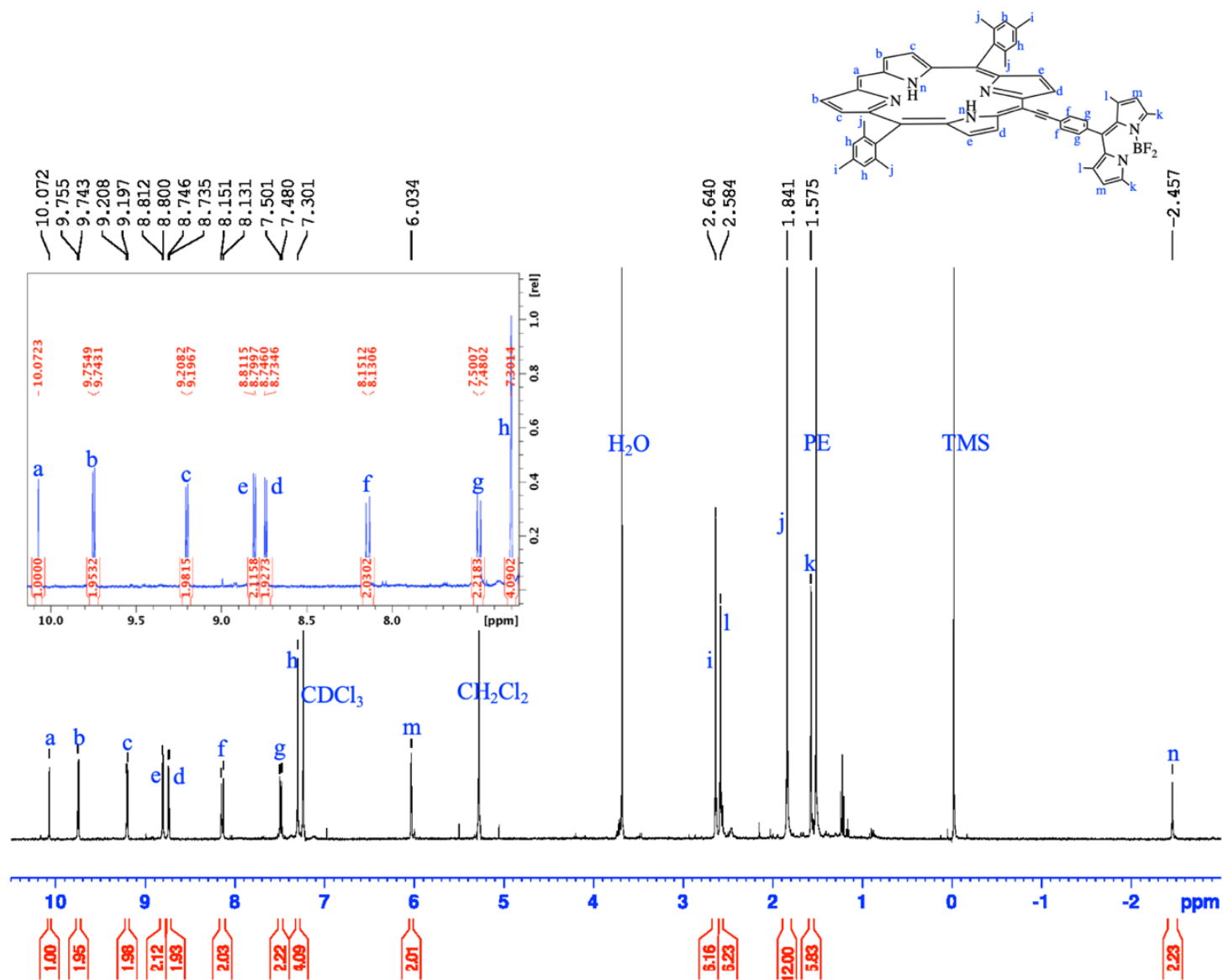


Figure 3.1. <sup>1</sup>H NMR spectrum for DMPH<sub>2</sub>-BDP in CDCl<sub>3</sub> at room temperature.

### 3.1.1.2 $^1\text{H}$ NMR for $\text{DMPH}_2\text{-COOH}$

The  $\text{DMPH}_2\text{-COOH}$  ligand is characterized by  $^1\text{H}$  NMR, this spectrum is illustrated in the Figure 3.2.

The singlet peak at 10.463 ppm indicates the *meso*-position **a** of the methine bridge, the integration of 1.00 proves this. The four sets of doublet peaks at 9.856-9.844 ppm, 9.510-9.501 ppm, 8.765-8.754 ppm and 8.681-8.671 ppm indicate  $\beta$ -positions **b**, **c**, **e** and **d** on the pyrrolic rings, the integrations of 1.93, 1.94, 1.90 and 1.97 prove the symmetry structure of  $\text{DMPH}_2\text{-COOH}$  ligand. The singlet peak at 7.398 ppm indicates the four *meta* positions **h** of two phenyl rings, the integration of 4.02 proves this. The singlet peak at 2.624 ppm indicates the two methyl groups **i** at *para* positions of two phenyl rings and the singlet peak at 1.792 ppm indicate the four methyl groups **j** at four *ortho* positions of two phenyl rings, also the integrations of 5.73 and 11.86 also prove these. The singlet peak at -2.602 ppm indicates the two NH positions **k** and the integration is 2.17.

The two sets of doublet peaks at 8.280-8.260 ppm and 8.201-8.181 ppm indicate the two *ortho* and *meta* positions **f**, **g** of the benzoic acid and the singlet broad peak at 13.238 indicates the OH position **l** of the benzoic acid. From this  $^1\text{H}$  NMR spectrum, the significant characteristic peaks of  $\text{DMPH}_2\text{-COOH}$  ligand are shown, and there are no peaks from impurities, which mean the  $\text{DMPH}_2\text{-COOH}$  ligand has been successfully synthesized.

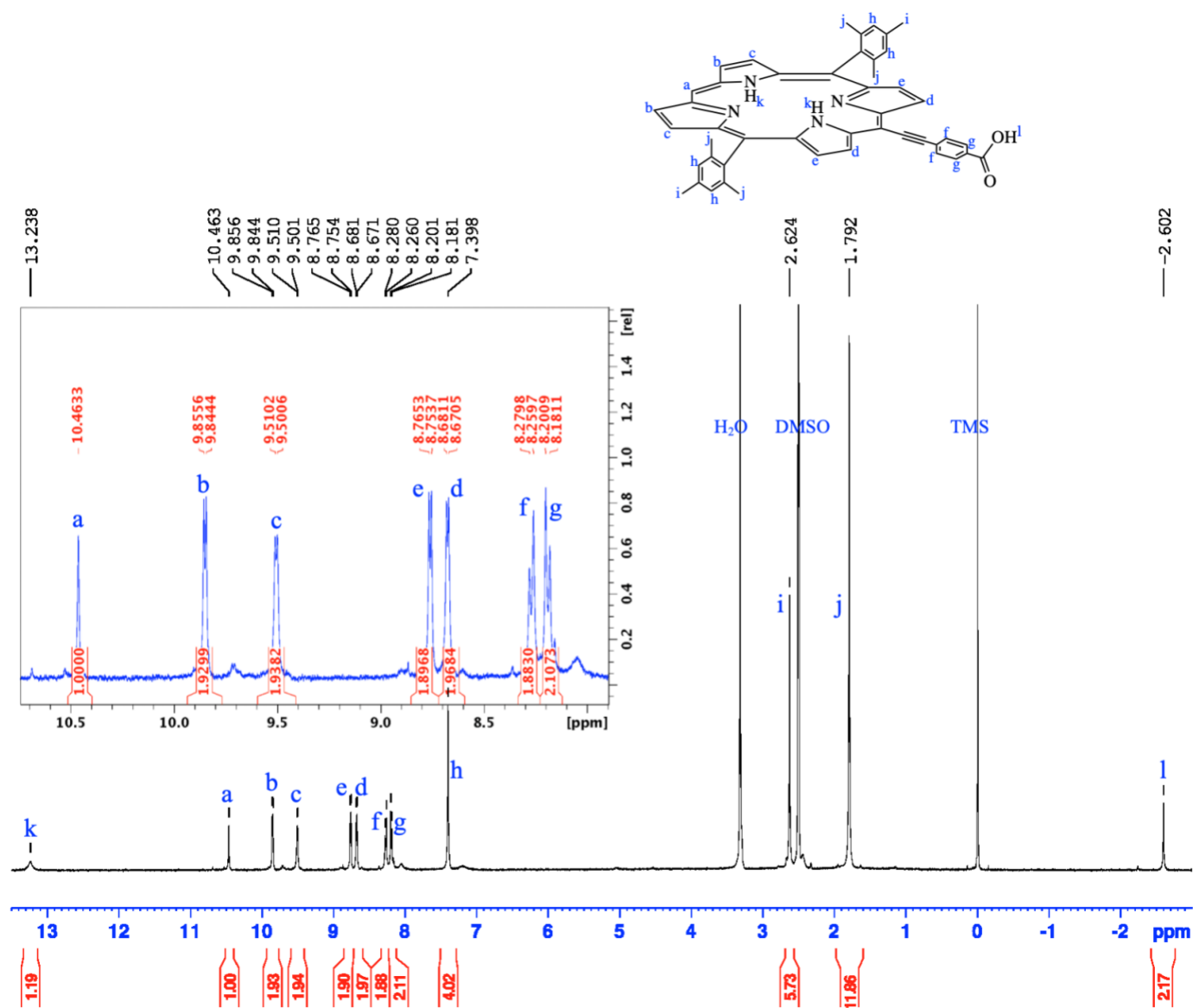


Figure 3.2. <sup>1</sup>H NMR spectrum for DMPH<sub>2</sub>-COOH in DMSO-d<sub>6</sub> at room temperature.

### 3.1.1.3 $^1\text{H}$ NMR for $\text{TPLH}_2$

5,10,15,20-tetraphenylporpholactone ( $\text{TPLH}_2$ ) is characterized by  $^1\text{H}$  NMR, the spectrum is shown in Figure 3.3.

In the  $^1\text{H}$  NMR spectrum of  $\text{TPLH}_2$ , the doublet of doublets of doublets peaks at 8.773-8.729 ppm and multiplet peaks at 8.574-8.540 ppm indicate the two sets of  $\beta$ -positions ***a*** and ***b*** on the pyrrolic rings, the integrations are 2.00 and 1.93 respectively. The doublet of doublets at 8.679-8.667 ppm and doublet peaks at 8.506-8.495 ppm indicate another two sets of  $\beta$ -positions ***d*** and ***c*** on the pyrrolic rings, the integrations are 1.14 and 0.96. The multiplet peaks at 8.121-8.062 ppm and doublet of doublets at 7.959-7.935 ppm indicate the *ortho* positions ***f*** and ***f'*** of the four phenyl rings, the integration of 5.94 and 2.05 prove this; also, the multiplet peaks at 7.729-7.710 ppm indicate the *meta* and *para* positions ***e'*** and ***e*** of the four phenyl rings, which is proved by integration of 11.73. The two sets of singlet peak at -1.695 ppm and -2.064 ppm indicate the two NH positions ***h*** and ***g***, which the integrations are 1.16 and 1.21. From this  $^1\text{H}$  NMR spectrum, the characteristic peaks of  $\text{TPLH}_2$  ligand are shown, and there are no peaks from impurities, which mean the  $\text{TPLH}_2$  ligand has been successfully synthesized.

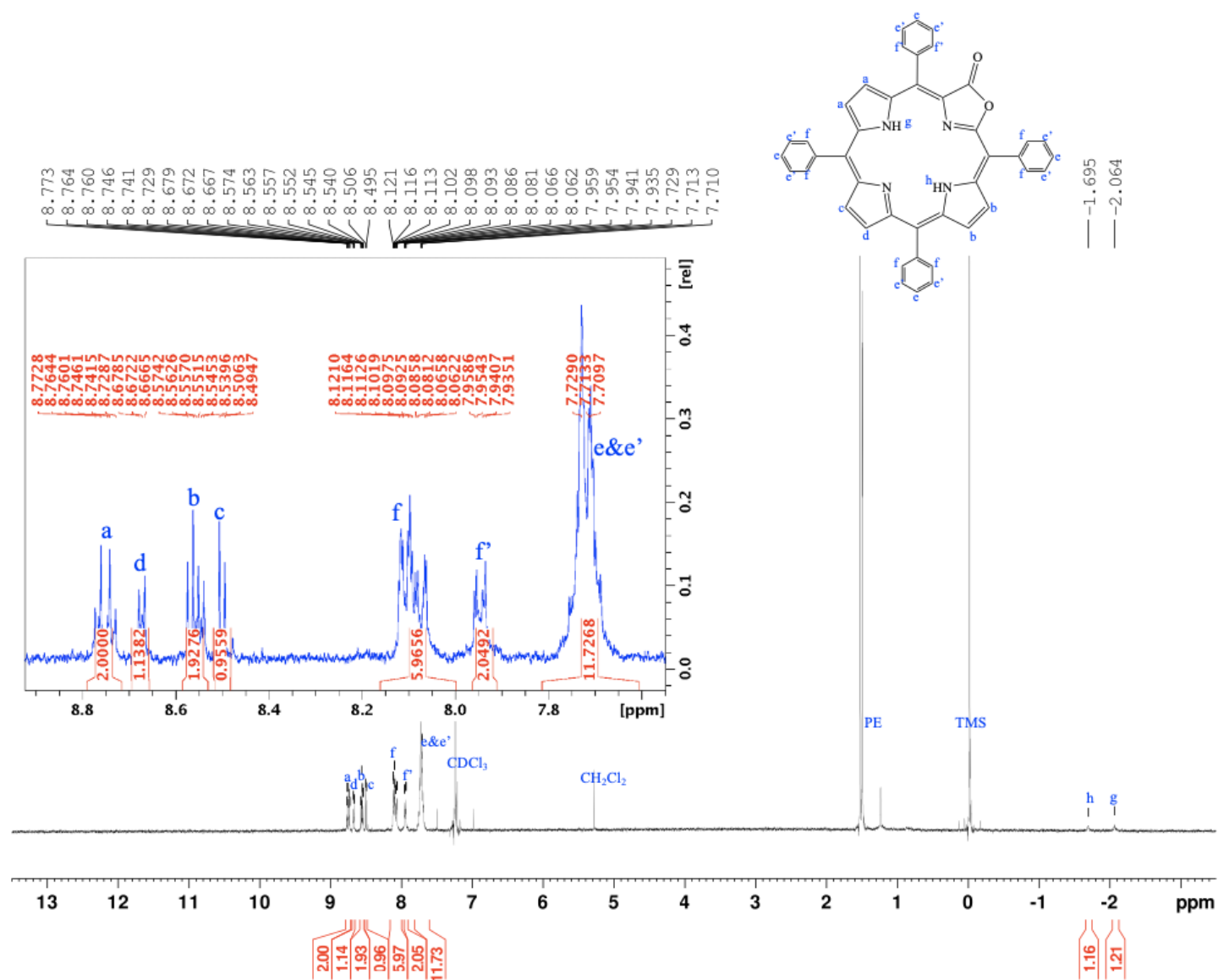


Figure 3.3. <sup>1</sup>H NMR spectrum for TPLH<sub>2</sub> in CDCl<sub>3</sub> at room temperature.

### 3.2 Optimization of TPLH<sub>2</sub> reaction conditions

A series of controlled experiments were designed and implemented to investigate the effects of temperature, catalyst ratio and reactants scale on the yield of TPLH<sub>2</sub> synthesis. The following table 3.1. summarizes the results of controlled experiments for TPLH<sub>2</sub> synthesis.

Table 3.1. Controlled experiments for TPLH<sub>2</sub> synthesis.

	Amount used (mmol)								
Trial	TPPH <sub>2</sub>	2,2'-bipyridine	RuCl <sub>3</sub>	Oxone	NaOH	TPLH <sub>2</sub> (mmol)	Yield (%)	Temp. (°C)	Ratio of RuCl <sub>3</sub>
1	0.4	0.09	0.08	3.84	4	0.06	14.45	80-85	0.2 equiv.
2	0.4	0.09	0.08	3.9	4.1	0.05	13.1	120-125	0.2 equiv.
3	0.56	0.13	0.12	5.87	7.22	0.09	16.19	100-105	0.2 equiv.
4	0.54	0.16	0.18	5.83	7.01	0.09	16.35	100-105	0.3 equiv.
5	1.34	0.38	0.3	14	15.65	0.16	11.64	100-105	0.3 equiv.
6	1.04	0.32	0.29	11.28	15.49	0.2	19.44	100-105	0.3 equiv.
7	0.97	0.33	0.29	11.4	15.28	0.18	18.71	100-105	0.3 equiv.

The effect of reaction temperature on yield is examined in trial 1, 2, and 3. As demonstrated in trial 3, the highest yield of TPLH<sub>2</sub> occurred when the reaction temperature is maintained between 100 and 105 °C, which yield is 16.19%. Temperatures that are too high or too low would reduce the yield. Controlled trial 3 and 4 are conducted to determine the effect of catalyst addition ratio on yield. As seen in trial 4, when catalyst RuCl<sub>3</sub> is 0.3 equivalent to reactant TPPH<sub>2</sub>, it slightly increases the yield of TPLH<sub>2</sub> comparing to it is 0.2 equivalent to reactant TPPH<sub>2</sub>.

The effect of large reactant scale on yield are discussed in trial 4, 5, 6, and 7. The results of trial 4 and 5 indicate that when the amount of TPPH<sub>2</sub> reactant addition increased, the yield does decrease from 16.35% to 11.64% under the same reaction conditions. However, it is observed that when the catalyst RuCl<sub>3</sub> addition is increased, it does not dissolve thoroughly in DI H<sub>2</sub>O. Trial 6 and 7 use heating and constant stirring to completely dissolve RuCl<sub>3</sub> in 40 mL of DI

H<sub>2</sub>O before slowly adding it to the reaction solution, resulting in a significantly increased yield of TPLH<sub>2</sub>. These controlled experiments provide some simple optimizations of TPLH<sub>2</sub> synthesis conditions and suggest some strategies for increasing TPLH<sub>2</sub> yields and generating large quantities of TPLH<sub>2</sub> products in a single experiment.

## 3.3 Photophysical properties

### 3.3.1 Absorbance

The UV-Vis absorption spectra for DMPH<sub>2</sub>-BDP ligand and YbDMP-BDP complex are shown in Figure 3.4. The DMPH<sub>2</sub>-BDP ligand has an intense peak at 430 nm in Soret-band region and four moderate peaks at 502 nm, 566 nm, 597 nm and 659 nm in Q-band region. Molar absorptivity of each peak shows  $\epsilon_{430 \text{ nm (Soret)}} > \epsilon_{502 \text{ nm}} > \epsilon_{566 \text{ nm}} > \epsilon_{659 \text{ nm}} > \epsilon_{597 \text{ nm}}$ . For YbDMP-BDP complex, one peak is observed at 438 nm in the Soret-band region and three peaks are observed at 502 nm, 562 nm and 611 nm in Q-band region. Molar absorptivity of each peak shows  $\epsilon_{438 \text{ nm (Soret)}} > \epsilon_{502 \text{ nm}} > \epsilon_{611 \text{ nm}} > \epsilon_{562 \text{ nm}}$ .

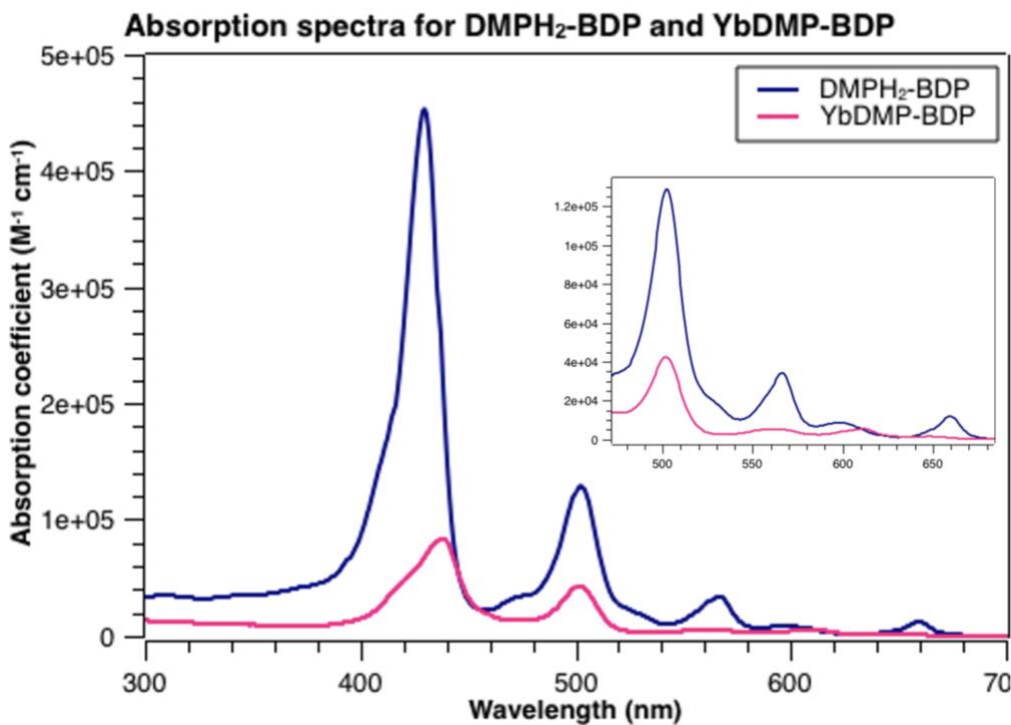


Figure 3.4. Absorption spectra of DMPH<sub>2</sub>-BDP ligand and YbDMP-BDP complex in DCM at room temperature with a concentration of  $8.2 \times 10^{-6}$  M.



Overall, the DMPH<sub>2</sub>-BDP ligand shows more intense and broader absorbance compared to the YbDMP-BDP complex, while the Soret-band peak of YbDMP-BDP complex is red-shifted 8 nm by the ligand.

The UV-Vis absorption spectra for DMPH<sub>2</sub>-COOH ligand and YbDMP-COOH complex are shown in Figure 3.5. The DMPH<sub>2</sub>-COOH ligand has an intense peak at 432 nm in Soret-band region and four moderate peaks at 528 nm, 568 nm, 598 nm and 660 nm in Q-band region. Molar absorptivity of each peak show  $\epsilon_{432 \text{ nm (Soret)}} > \epsilon_{568 \text{ nm}} > \epsilon_{528 \text{ nm}} > \epsilon_{660 \text{ nm}} > \epsilon_{598 \text{ nm}}$ . For YbDMP-COOH complex, one peak is observed at 439 nm in the Soret-band region and two peaks are observed at 568 nm and 615 nm. Molar absorptivity of each peak show  $\epsilon_{439 \text{ nm (Soret)}} > \epsilon_{615 \text{ nm}} > \epsilon_{568 \text{ nm}}$ .

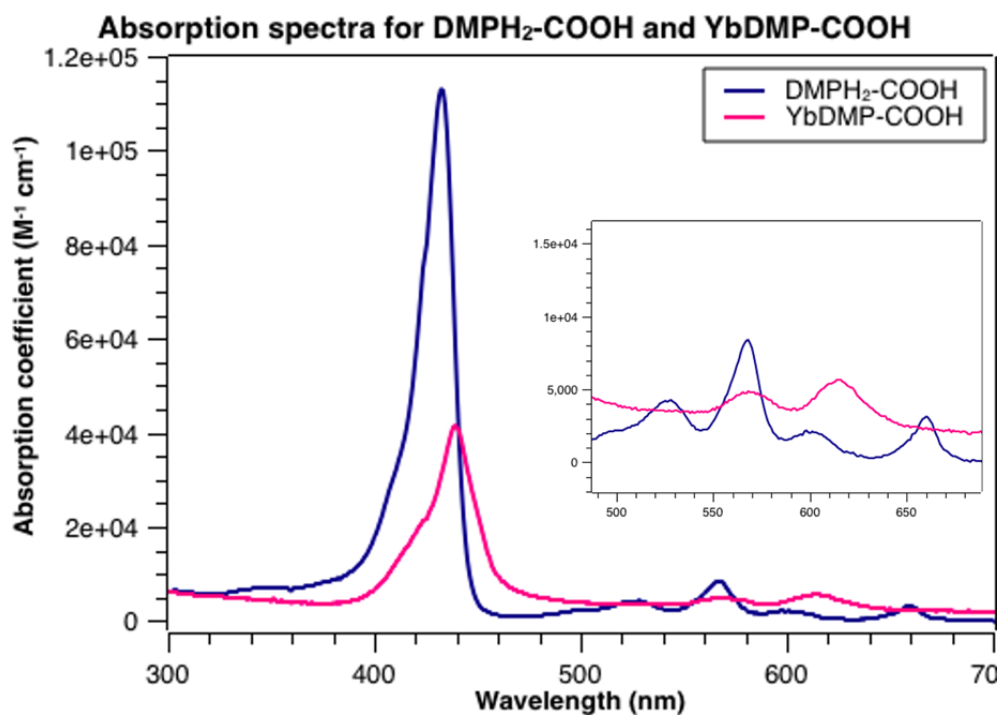


Figure 3.5. Absorption spectra of DMPH<sub>2</sub>-COOH ligand and YbDMP-COOH complex in DCM at room temperature with a concentration of  $3.5 \times 10^{-6}$  M.

Similarly, the DMPH<sub>2</sub>-COOH ligand shows more intense and broader absorbance compared to the YbDMP-COOH complex. Also, the Soret-band peak of YbDMP-COOH complex is red-shifted 7 nm by the ligand.

In two sets of ligands and complexes, the ligands exhibit a greater number of peaks with broader absorbance at 660 nm in far-red region in comparison to the complexes. According to Gouterman's theory, this is owing to the lower symmetry of DMPH<sub>2</sub>-BDP and DMPH<sub>2</sub>-COOH ligands before the substitution of ytterbium. In the case of YbDMP-BDP and YbDMP-COOH complexes, all four N atoms on the porphyrin ring are coordinated to the Yb(III) ion, which increases the symmetry of complex, brings the energy levels closer together, decreases the degree of molecular orbital splitting, and increases the degree of cylinder incorporation, resulting in a decrease in the number of Q band peaks.

The UV-Vis absorption spectrum for YbDMP complex as reference is also shown in Figure 3.6. It has an intense peak at 413 nm in Soret-band region and one moderate peak at 544 nm in Q-band region.

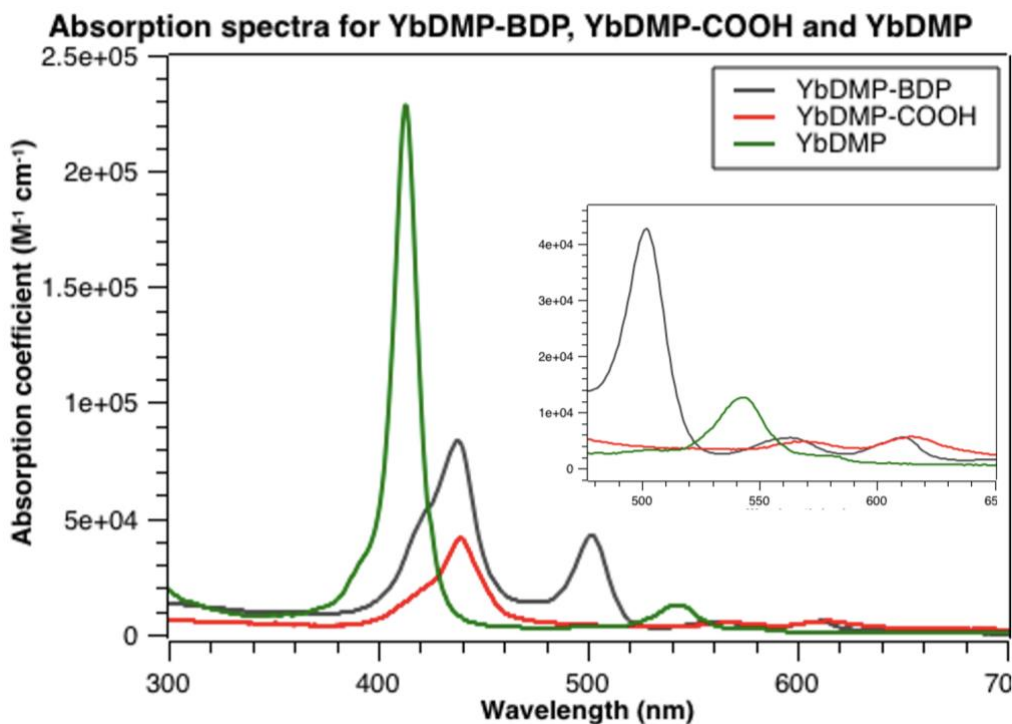


Figure 3.6. Absorption spectra of YbDMP-BDP, YbDMP-COOH and YbDMP complexes in DCM at room temperature with a concentration of  $3.5 \times 10^{-6}$  M.

The Soret-band peaks of YbDMP-BDP and YbDMP-COOH complexes are 26 nm red-shifted compared with YbDMP complex. In the Q-band region, the absorption coefficients of two peaks centered at 560-570 nm and 610-615 nm are enhanced and red-shifted compared to a single peak at 544 nm for YbDMP. But in general, the absorption coefficients for YbDMP-BDP and YbDMP-COOH complexes are lower than YbDMP. The 4-ethynylbenzoic acid and 8-(4-ethynylphenyl)-1,3,5,7-tetramethyl-BODIPY attached to the porphyrin ring form the larger  $\pi$ -conjugated system, which gives absorption a red-shift.

Comparing two ligands, as shown in Figure 3.7, both DMPH<sub>2</sub>-BDP and DMPH<sub>2</sub>-COOH exhibit very similar absorption peaks in the Q-band region between 540 and 680 nm. In addition, DMPH<sub>2</sub>-BDP has a strong absorption peak centered at 502 nm. This could be seen as a co-absorption derived from the tetramethyl-BODIPY derivative, which compensates for the

weak absorption of DMPH<sub>2</sub>-COOH in the 480-520 nm region. The same property is exhibited in the corresponding Yb(III) complexes as well. Also, both the DMPH<sub>2</sub>-BDP and YbDMP-BDP have higher absorption coefficients comparing to DMPH<sub>2</sub>-COOH and YbDMP-BDP, indicating that the BODIPY derivative has outstanding properties as auxiliary ligands in the absorption spectra.

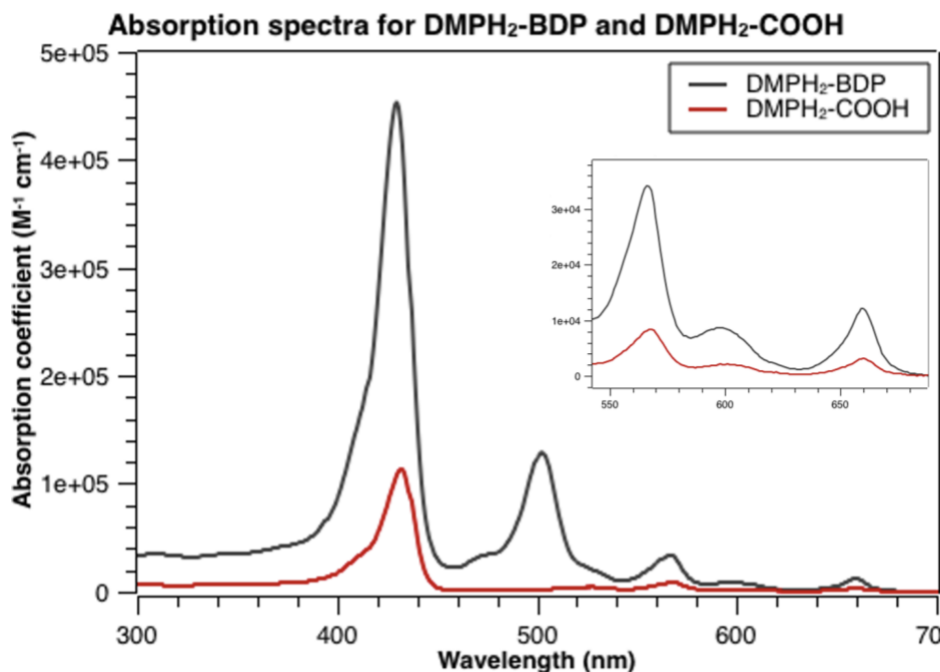


Figure 3.7. Absorption spectra of DMPH<sub>2</sub>-COOH and DMPH<sub>2</sub>-BDP ligands in DCM at room temperature with a concentration of  $3.5 \times 10^{-6}$  M.

The UV-Vis absorption spectra for TPLH<sub>2</sub> and TPPH<sub>2</sub> ligands are shown in Figure 3.8. The TPLH<sub>2</sub> ligand has an intense peak at 412 nm in Soret-band region and five moderate peaks at 520 nm, 558 nm, 588 nm, 641 nm and 688 nm in Q-band region. Molar absorptivity of each peak shows  $\epsilon_{412 \text{ nm (Soret)}} > \epsilon_{558 \text{ nm}} > \epsilon_{520 \text{ nm}} > \epsilon_{588 \text{ nm}} > \epsilon_{641 \text{ nm}} > \epsilon_{688 \text{ nm}}$ . For TPPH<sub>2</sub> ligand as reference, one peak is observed at 412 nm in the Soret-band region and four peaks are observed at 514 nm, 548 nm, 589 nm and 645 nm in Q-band region. Molar absorptivity of each peak shows  $\epsilon_{412 \text{ nm (Soret)}} > \epsilon_{514 \text{ nm}} > \epsilon_{548 \text{ nm}} > \epsilon_{589 \text{ nm}} > \epsilon_{645 \text{ nm}}$ .

In comparison to TPPH<sub>2</sub> as reference, overall TPLH<sub>2</sub> has a slightly greater absorption, and the absorption peaks of TPLH<sub>2</sub> are generally red-shifted in the Q-band region, reaching up to 668 nm.

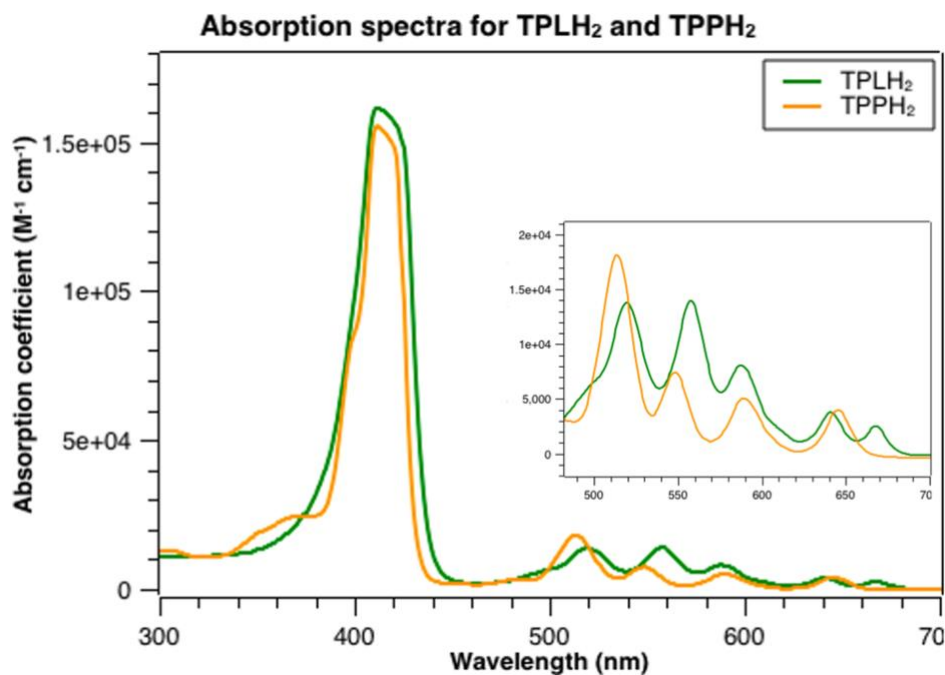


Figure 3.8. Absorption spectra of TPLH<sub>2</sub> and TPPH<sub>2</sub> ligands in DCM at room temperature with a concentration of  $1.95 \times 10^{-5}$  M.

### 3.3.2 Fluorescence emission

#### 3.3.2.1 Fluorescence emission in visible region

With the excitation at 556 nm, the DMPH<sub>2</sub>-BDP ligand has two fluorescence emission peaks at 662 nm and 730 nm in visible region; the DMPH<sub>2</sub>-COOH ligand has two fluorescence emission peaks at 662 nm and 735 nm in visible region, shown in Figure 3.9. The fluorescence intensity of YbDMP-BDP complex is less than 8.16% and Yb-COOH complex is less than 5.90% of the ligands, respectively. The DMPH<sub>2</sub>-BDP and DMPH<sub>2</sub>-COOH ligands show two strong emission peaks in the visible region, mainly as a result of the HOMO-LUMO transition. In comparison, the emission of their Yb<sup>3+</sup> complexes are quite feeble, indicating that the Yb<sup>3+</sup>

complexes have fluorescence quench in the visible region. The energy transfer from the ligands to the excited state of  $\text{Yb}^{3+}$  is most likely responsible for the fluorescence quench for the complexes.

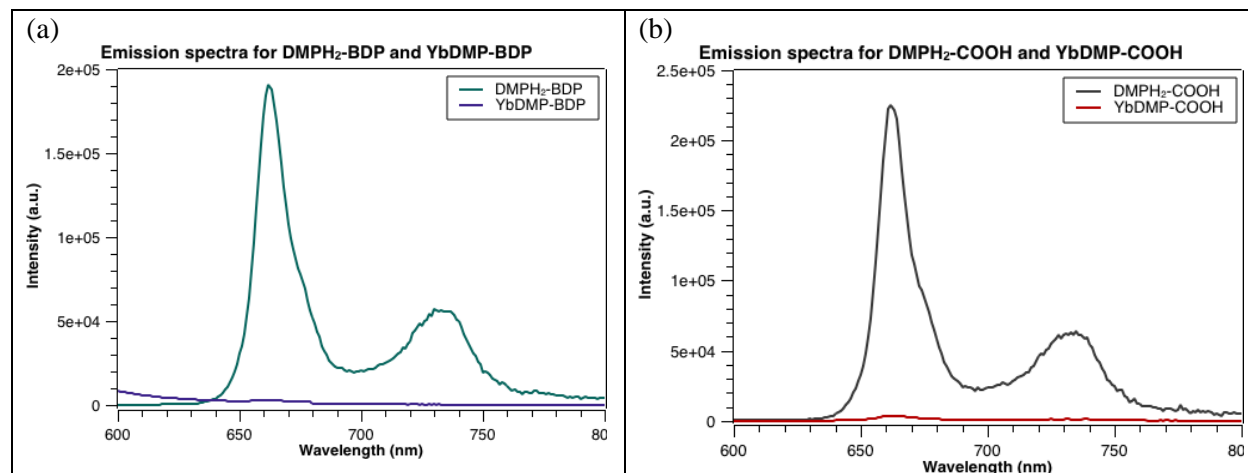


Figure 3.9. Emission spectra for DMPH<sub>2</sub>-BDP and YbDMP-BDP ( $\lambda_{\text{ex}} = 556 \text{ nm}$ ) (a) and emission spectra for DMPH<sub>2</sub>-COOH and YbDMP-COOH ( $\lambda_{\text{ex}} = 556 \text{ nm}$ ) (b) in DCM at room temperature with a concentration of  $3.50 \times 10^{-6} \text{ M}$ .

As shown in Figure 3.10, with the excitation at 556 nm, the TPLH<sub>2</sub> has two fluorescence emission peaks at 646 nm and 672 nm in visible region; the TPPH<sub>2</sub> as reference has two fluorescence emission peaks at 652 nm and 717 nm in visible region. At the same concentration, the emission intensity of TPLH<sub>2</sub> is stronger than that of TPPH<sub>2</sub>. Also, the emission peaks of TPLH<sub>2</sub> are narrow, which has advantages in reducing background and improving resolution.

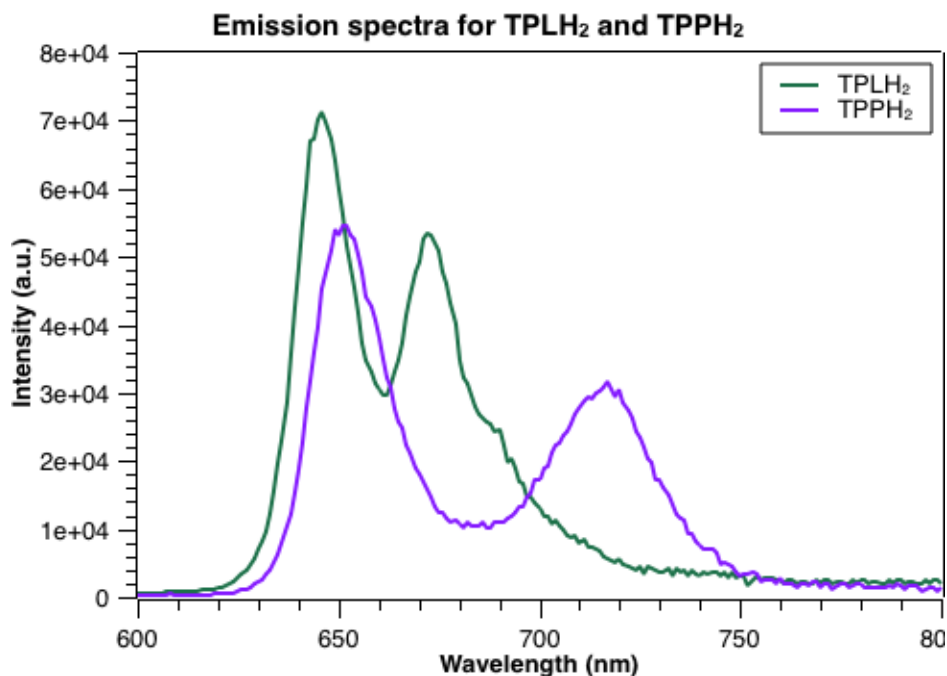


Figure 3.10. Emission spectra of TPLH<sub>2</sub> and TPPH<sub>2</sub> ( $\lambda_{\text{ex}} = 556 \text{ nm}$ ), in DCM at room temperature with a concentration of  $1.95 \times 10^{-5} \text{ M}$ .

### 3.3.2.2 Fluorescence emission in near-infrared region

With the excitation at different wavelengths, the YbDMP-BDP has two peaks at 978 nm and 1005 nm; the YbDMP-COOH complex has two peaks at 976 nm and 1002 nm with various intensities. The excitation wavelengths are chosen in accordance with the wavelengths of the YbDMP-BDP and YbDMP-COOH peaks in the absorption spectra. As seen in Figure 3.11, the varying excitation wavelengths have no effect on the shape of the two NIR emissions, but rather on their intensities.

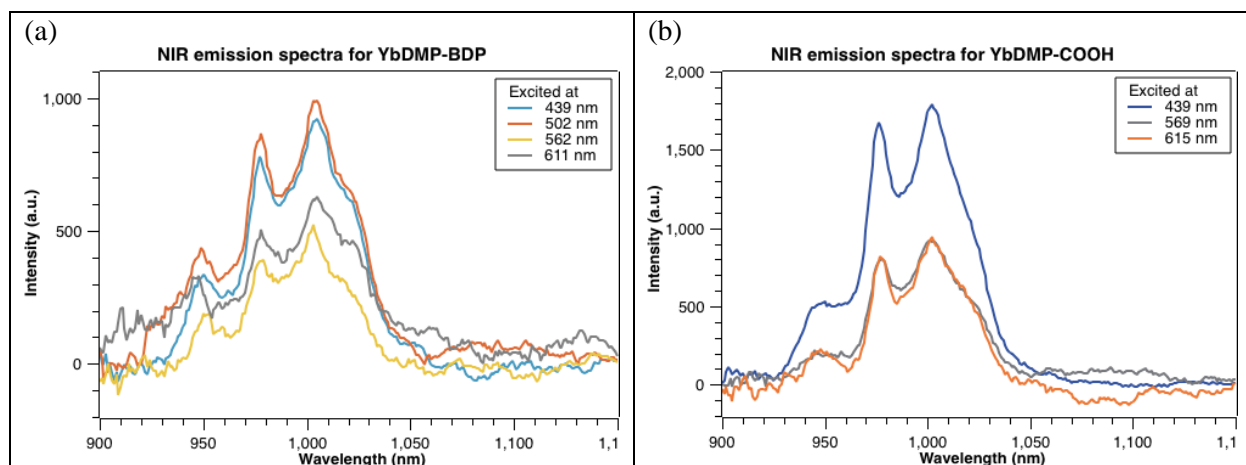


Figure 3.11. Emission spectra of YbDMP-BDP (concentration:  $5.0 \times 10^{-5}$  M) (a) and emission spectra of YbDMP-COOH (concentration:  $3.5 \times 10^{-5}$  M) (b) in DCM at room temperature, excited at various wavelengths.

It is notable that for YbDMP-BDP complex, the emission intensity with  $\lambda_{\text{ex}} = 502$  nm is higher than that with  $\lambda_{\text{ex}} = 439$  nm. The emission intensity of the YbDMP-COOH complex is twice at  $\lambda_{\text{ex}} = 439$  nm compared to  $\lambda_{\text{ex}} = 569$  nm, which is attributed to the Soret-band peak absorption being higher than Q-band peaks. Additionally, for two complexes, the emission intensity with longer  $\lambda_{\text{ex}}$  at 611/615 nm is slightly greater than that with shorter  $\lambda_{\text{ex}}$  at 562/569 nm.

The YbDMP-BDP and YbDMP-COOH complexes show two peaks in the NIR region after being excited, exhibiting characteristic  $\text{Yb}^{3+}$  emission, which are corresponded to the  $^2\text{F}_{5/2} - ^2\text{F}_{7/2}$  transition. Also,  $M_J$  splitting in the ground and/or emission states could be responsible for the various peaks that are shown in both complexes. The eight-coordination environment surrounding the  $\text{Yb}^{3+}$  ion could be inferred from the emission peaks centered at 978/976 nm and 1005/1002 nm, which were quite near to each other.

As discussed in Section 1.3.3, a process known as antenna effect is the reason for fluorescence emission of YbDMP-BDP and YbDMP-COOH complexes in NIR region. In this



process, light is first absorbed by the DMPH<sub>2</sub>-BDP or DMPH<sub>2</sub>-COOH, and energy transfers from the ligand to Yb<sup>3+</sup> ions through its triplet state. Then, lanthanide ion produces fluorescence, which is measured using a spectrometer in NIR region. In summary, the NIR emission of these two complexes are because of the intramolecular energy transfer.

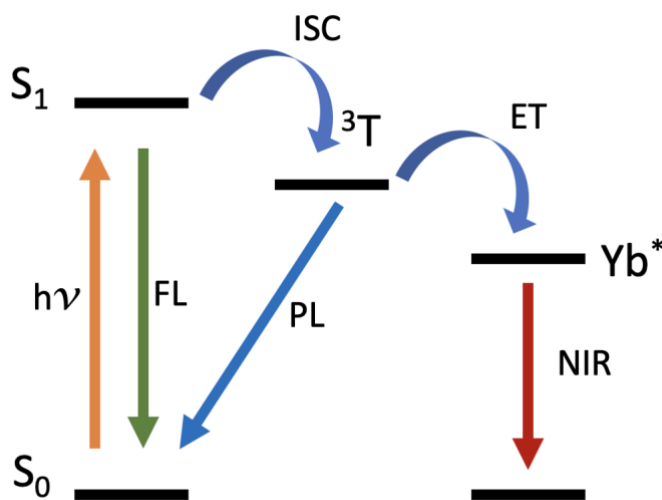


Figure 3.12. Jablonski diagram for YbDMP-BDP and YbDMP-COOH complexes;  $S_0$ , ground state;  $S_1$ , excited state;  $^3T$ , triplet state;  $Yb^*$ , lanthanide excited state, FL, fluorescence; PL, phosphorescence; ET, energy transfer; ISC, intersystem crossing.

### 3.3.3 Quantum yield measurements

Porphyrins and the majority of lanthanide complexes have great fluorescence properties, which are mostly attributed to the coordination process between porphyrins and lanthanide ions. Numerous lanthanide porphyrin complexes have a great affinity for tumor cells and could be used to identify diseased tissue. The long-lasting excited triplet state of lanthanide porphyrins usually provide a theoretical foundation for the selection of photosensitizers in photodynamic diagnostics. The effect of various substituents on the fluorescence emission characteristics of porphyrins could be investigated by measuring the fluorescence quantum yields of porphyrins and their substituted derivatives, as well as their lanthanide complexes.

With the excitation at 556 nm, the fluorescence quantum yields of DMPH<sub>2</sub>-BDP, DMPH<sub>2</sub>-COOH, TPLH<sub>2</sub> ligands and YbDMP-BDP, YbDMP-COOH complexes were measured in DCM. The  $\Phi_{\text{DMPH}_2\text{-BDP}}$  is 0.74, the  $\Phi_{\text{DMPH}_2\text{-COOH}}$  is 0.78 and  $\Phi_{\text{TPLH}_2}$  is 0.89. Their quantum yields are greatly improved as compared to reference TPPH<sub>2</sub> ( $\Phi_{\text{TPPH}_2} = 0.62$ , in DCM).

Porphyrins feature conjugated structures with a variety of substituent groups. Typically, substituent groups at the *meso*- and  $\beta$ - positions improve fluorescence emission. The addition of 8-(4-ethynylphenyl)-1,3,5,7-tetramethyl-BODIPY and 4-ethynylbenzoic acid at one *meso*-position of DMPH<sub>2</sub> could both operate as electron-donating groups because they contribute to the porphyrin conjugation system. Also, the acetylacetonate (the OR- group) on the  $\beta$ -position of inner porphyrin ring functions as an electron-donating group. The electron-donating substituents on porphyrins enhance the emission intensity, while the electron-withdrawing substituents reduce the emission intensity. This is because the electron lone pairs or the electrons of the substituent participate in the conjugated  $\pi$ -bond of porphyrin molecule, which increases the conjugation system and decreases the electron leap energy level of the porphyrin macrocycle.

The fluorescence quantum yields of YbDMP-BDP and YbDMP-COOH complexes are both 0.023 in DCM. The quantum yields of two complexes are slightly higher than that of YbDMP, which was 0.021.<sup>79</sup>

The quantum yields of the complexes are much lower than that of the ligands is attributed to the existence of steric effects, which could disrupt the coplanarity and conjugation of the molecule, thus weakening the emission. Also, the light absorbed by the porphyrin ligands is lost by vibrational relaxation and phosphorescence processes that reduce emission efficiency. In addition, the oscillation effect brought by the solution is also the reason for the low emission efficiency.

The following contents calculate the quantum yields of ligands and complexes.

TPPH<sub>2</sub> as reference:

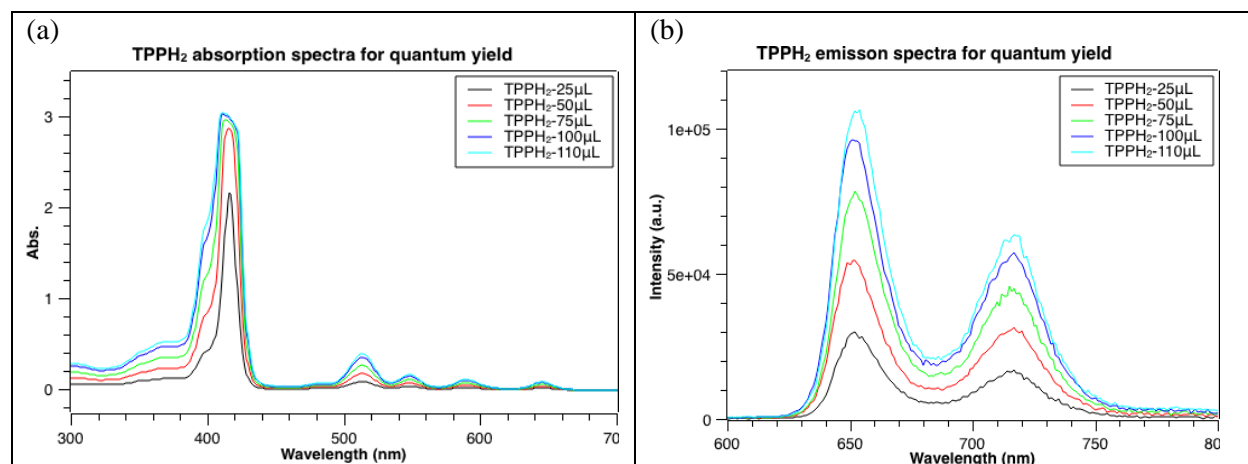


Figure 3.13. Absorption spectra for TPPH<sub>2</sub> with gradient concentrations (a) and emission spectra for TPPH<sub>2</sub>

with gradient concentrations ( $\lambda_{\text{ex}} = 556 \text{ nm}$ ) (b) in DCM at room temperature with a stock solution

concentration (TPPH<sub>2</sub>) of  $5.08 \times 10^{-5} \text{ M}$ .

Table 3.2. Absorbance and integrated fluorescence of TPPH<sub>2</sub> with gradient concentrations.

	Absorbance at 556 nm	Integration
TPLH <sub>2</sub> -25 μL, DCM-2.5 mL	0.0197	1381480.00
TPLH <sub>2</sub> -50 μL, DCM-2.5 mL	0.0434	2641340.00
TPLH <sub>2</sub> -75 μL, DCM-2.5 mL	0.0665	3765670.00
TPLH <sub>2</sub> -100 μL, DCM-2.5 mL	0.0911	4780720.00
TPLH <sub>2</sub> -110 μL, DCM-2.5 mL	0.1015	5258740.00

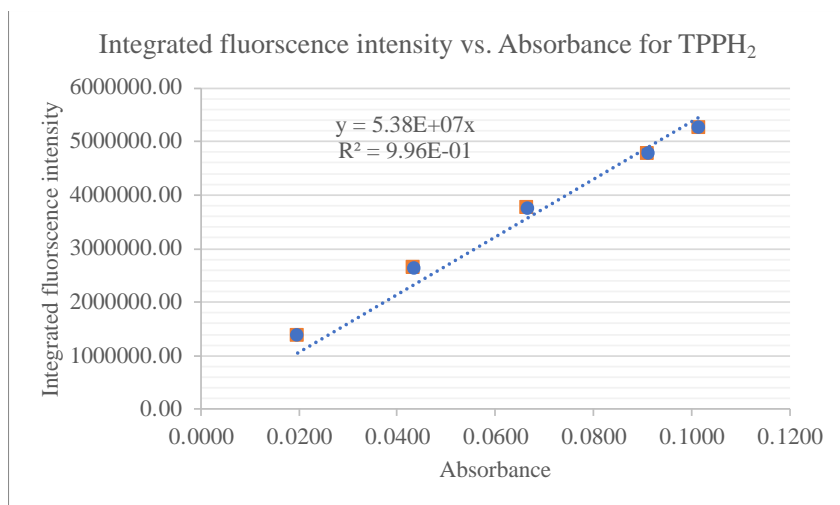


Figure 3.14. Integrated fluorescence vs. absorbance graph for TPPH<sub>2</sub> quantum yield determination.

DMPH<sub>2</sub>-BDP ligand:

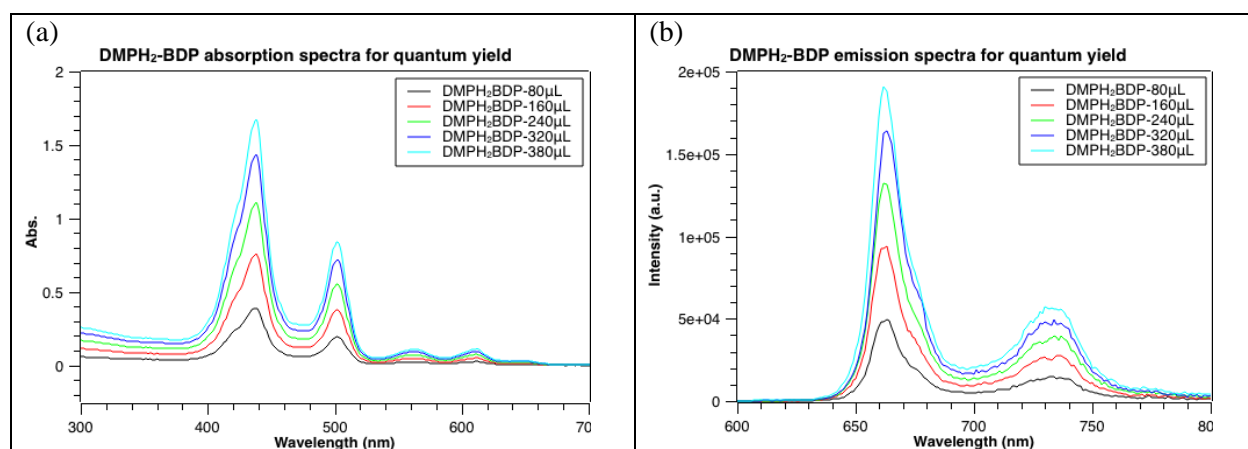


Figure 3.15. Absorption spectra for DMPH<sub>2</sub>-BDP with gradient concentrations (a) and emission spectra for

DMPH<sub>2</sub>-BDP with gradient concentrations ( $\lambda_{\text{ex}} = 556 \text{ nm}$ ) (b) in DCM at room temperature with a stock

solution concentration (DMPH<sub>2</sub>-BDP) of  $4.93 \times 10^{-5} \text{ M}$ .

Table 3.3. Absorbance and integrated fluorescence of DMPH<sub>2</sub>-BDP with gradient concentrations.

	Absorbance at 556 nm	Integration
DMPH <sub>2</sub> BDP-80 $\mu\text{L}$ , DCM-2.5 mL	0.0222	1624890.00
DMPH <sub>2</sub> BDP-160 $\mu\text{L}$ , DCM-2.5 mL	0.0445	3034990.00
DMPH <sub>2</sub> BDP-240 $\mu\text{L}$ , DCM-2.5 mL	0.0648	4281490.00
DMPH <sub>2</sub> BDP-320 $\mu\text{L}$ , DCM-2.5 mL	0.0854	5306610.00
DMPH <sub>2</sub> BDP-380 $\mu\text{L}$ , DCM-2.5 mL	0.0998	6296660.00

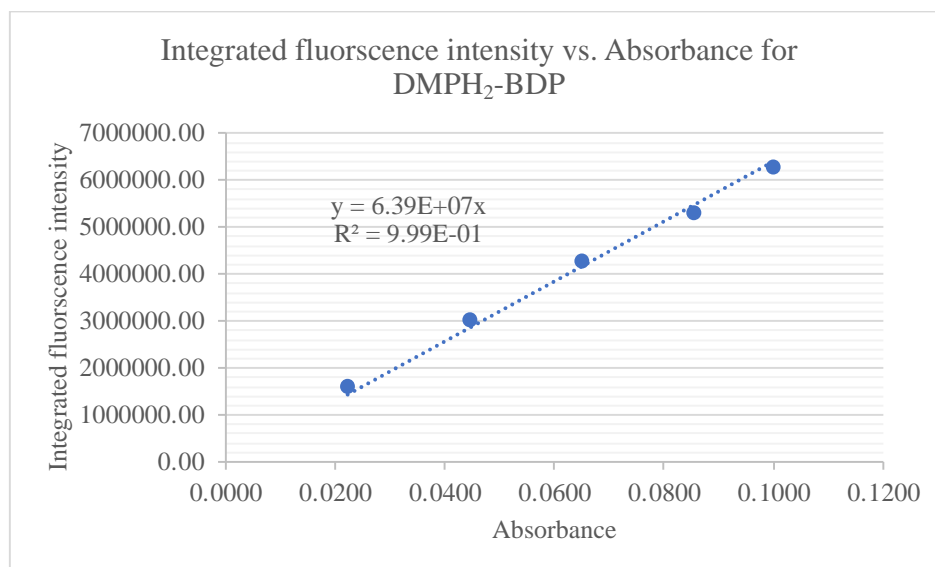


Figure 3.16. Integrated fluorescence vs. absorbance graph for DMPH<sub>2</sub>-BDP quantum yield determination.

Following the equation  $\Phi_X = \Phi_{ST} \left( \frac{\text{Grad}_X}{\text{Grad}_{ST}} \right) \left( \frac{\eta_X^2}{\eta_{ST}^2} \right)$ , the quantum yield of DMPH<sub>2</sub>-BDP in

DCM is calculated,  $\Phi_{\text{DMPH}_2\text{-BDP}} = 0.62 \times \left( \frac{6.39 \times 10^7}{5.38 \times 10^7} \right) \times 1 = 0.74$ .

TPLH<sub>2</sub> ligand:

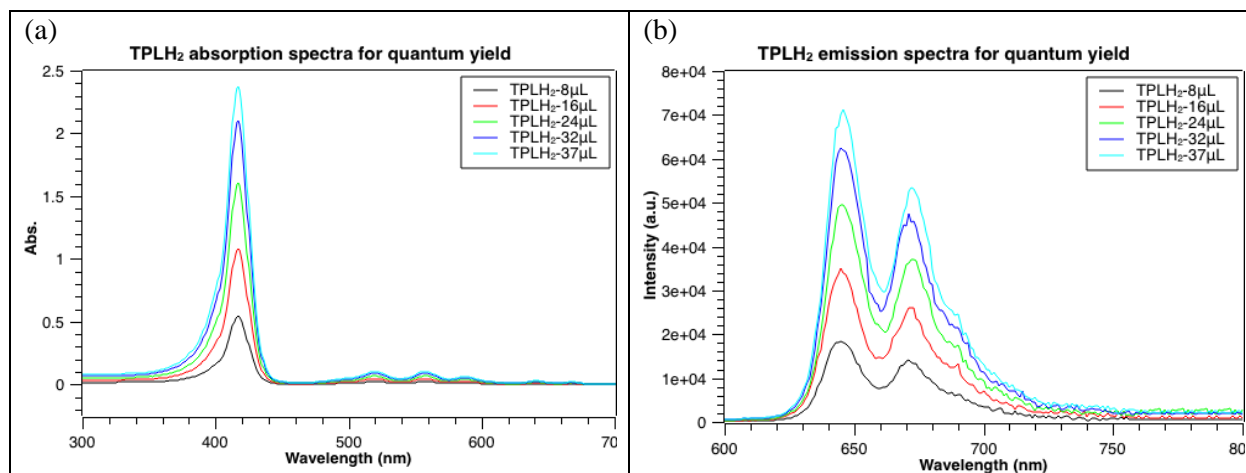


Figure 3.17. Absorption spectra for TPLH<sub>2</sub> with gradient concentrations (a) and emission spectra for TPLH<sub>2</sub>

with gradient concentrations ( $\lambda_{\text{ex}} = 556 \text{ nm}$ ) (b) in DCM at room temperature with a stock solution

concentration (TPLH<sub>2</sub>) of  $5.06 \times 10^{-5} \text{ M}$ .

Table 3.4. Absorbance and integrated fluorescence of TPLH<sub>2</sub> with gradient concentrations.

	Absorbance at 556 nm	Integration
TPLH <sub>2</sub> -8 $\mu$ L, DCM-2.5 mL	0.0218	1162000.00
TPLH <sub>2</sub> -16 $\mu$ L, DCM-2.5 mL	0.0440	2168850.00
TPLH <sub>2</sub> -24 $\mu$ L, DCM-2.5 mL	0.0663	3087010.00
TPLH <sub>2</sub> -32 $\mu$ L, DCM-2.5 mL	0.0886	3899240.00
TPLH <sub>2</sub> -37 $\mu$ L, DCM-2.5 mL	0.1031	4430050.00

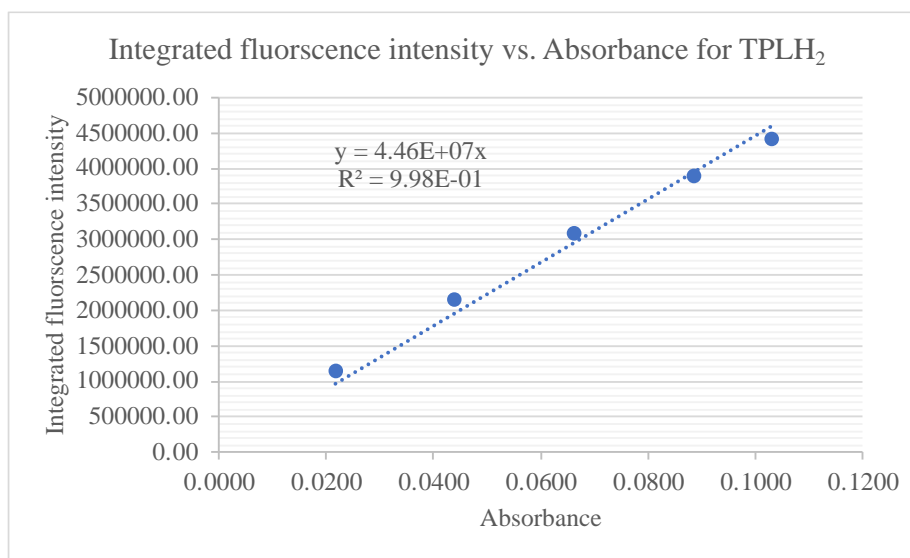


Figure 3.18. Integrated fluorescence vs. absorbance graph for TPLH<sub>2</sub> quantum yield determination.

Following the equation  $\Phi_X = \Phi_{ST} \left( \frac{\text{Grad}_X}{\text{Grad}_{ST}} \right) \left( \frac{\eta_X^2}{\eta_{ST}^2} \right)$ , the quantum yield of DMPH<sub>2</sub>-BDP in

DCM is calculated,  $\Phi_{\text{TPLH}_2} = 0.62 \times \left( \frac{6.39 \times 10^7}{4.46 \times 10^7} \right) \times 1 = 0.89$ .

TPPH<sub>2</sub> as reference:

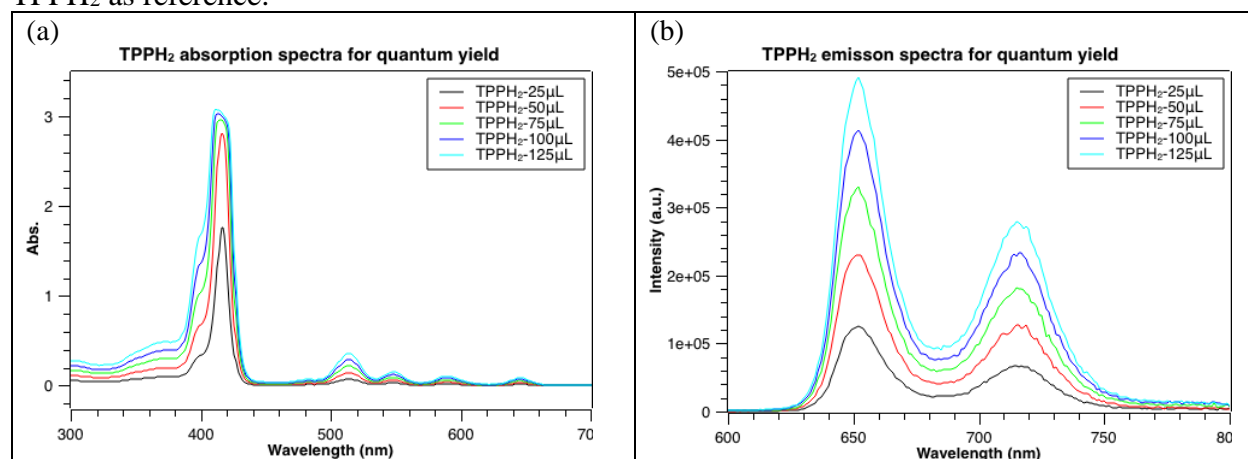


Figure 3.19. Absorption spectra for TPPH<sub>2</sub> with gradient concentrations (a) and emission spectra for TPPH<sub>2</sub>

with gradient concentrations ( $\lambda_{\text{ex}} = 556 \text{ nm}$ ) (b) in DCM at room temperature with a stock solution

concentration (TPPH<sub>2</sub>) of  $4.95 \times 10^{-5} \text{ M}$ .

Table 3.5. Absorbance and integrated fluorescence of TPPH<sub>2</sub> with gradient concentrations.

	Absorbance at 556 nm	Integration
TPPH <sub>2</sub> -25 μL, DCM-2.5 mL	0.0199	5857410.00
TPPH <sub>2</sub> -50 μL, DCM-2.5 mL	0.0398	10812700.00
TPPH <sub>2</sub> -75 μL, DCM-2.5 mL	0.0617	15548900.00
TPPH <sub>2</sub> -100 μL, DCM-2.5 mL	0.0809	19833900.00
TPPH <sub>2</sub> -125 μL, DCM-2.5 mL	0.1009	23586400.00

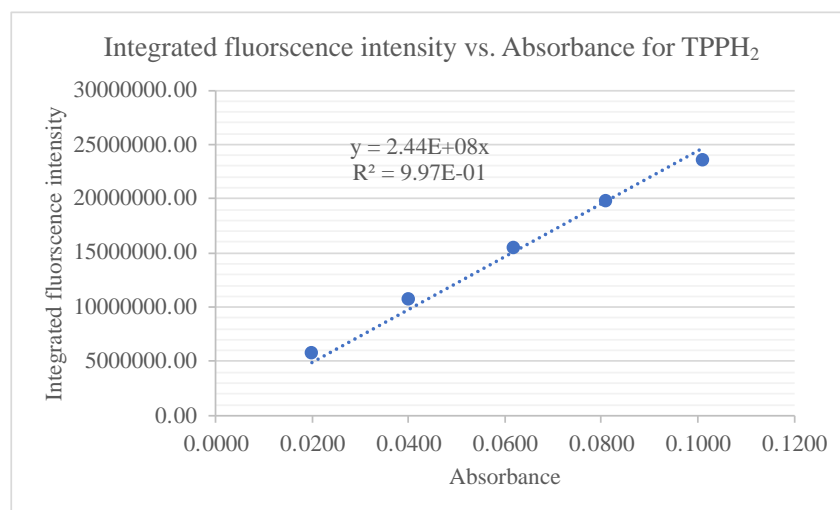


Figure 3.20. Integrated fluoroscence vs. absorbance graph for TPPH<sub>2</sub> quantum yield determination.

DMPH<sub>2</sub>-COOH ligand:

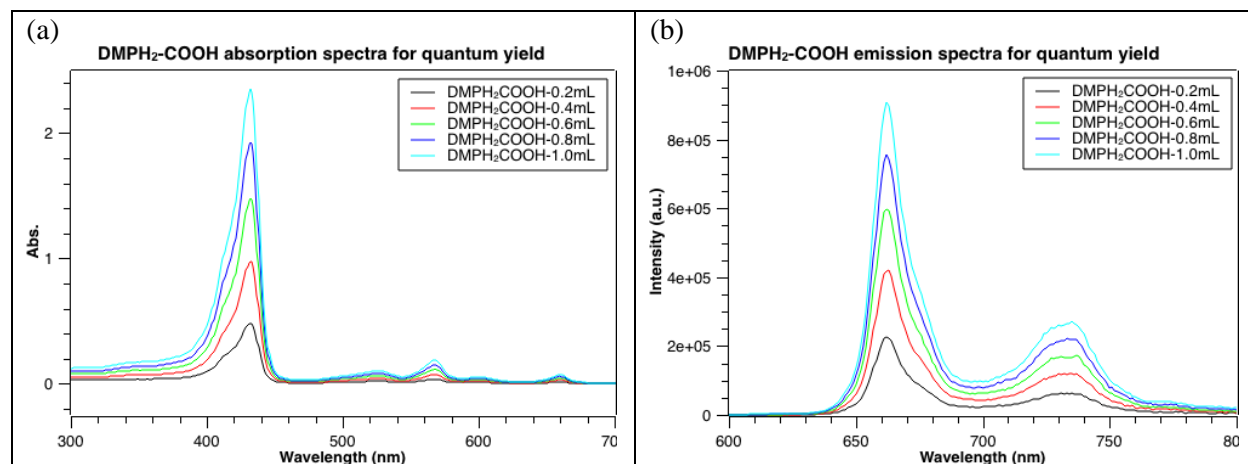


Figure 3.21. Absorption spectra for DMPH<sub>2</sub>-COOH with gradient concentrations (a) and emission spectra for DMPH<sub>2</sub>-COOH with gradient concentrations ( $\lambda_{\text{ex}} = 556 \text{ nm}$ ) (b) in DCM at room temperature with a stock solution concentration (DMPH<sub>2</sub>-COOH) of  $1.45 \times 10^{-5} \text{ M}$ .

Table 3.6. Absorbance and integrated fluorescence of DMPH<sub>2</sub>-COOH with gradient concentrations.

	Absorbance at 556 nm	Integration
DMPH <sub>2</sub> COOH-0.2 mL, DCM-2.8 mL	0.0194	7157340.00
DMPH <sub>2</sub> COOH-0.4 mL, DCM-2.6 mL	0.0407	13506400.00
DMPH <sub>2</sub> COOH-0.6 mL, DCM-2.4 mL	0.0626	19344300.00
DMPH <sub>2</sub> COOH-0.8 mL, DCM-2.2 mL	0.0813	24658500.00
DMPH <sub>2</sub> COOH-1.0 mL, DCM-2.0 mL	0.1018	29909000.00



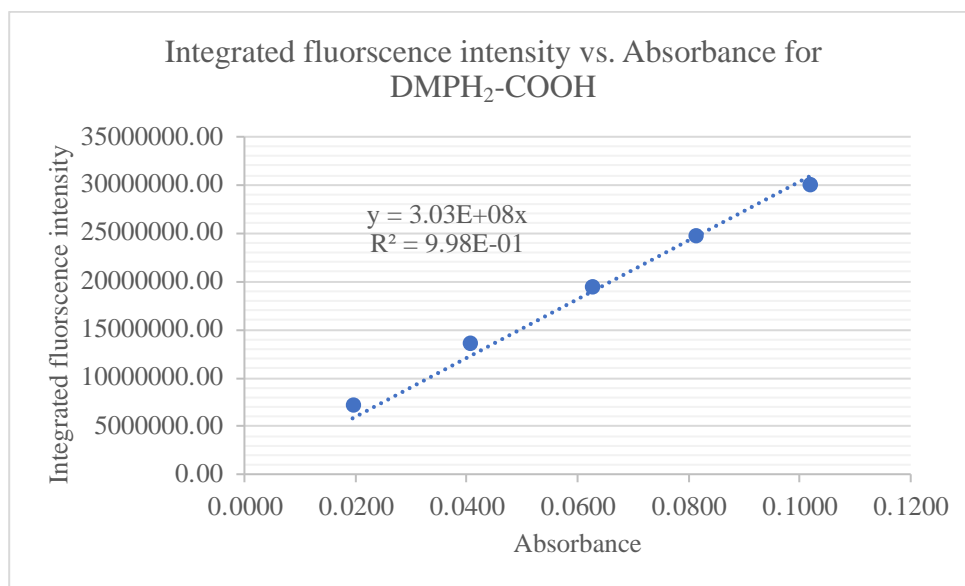


Figure 3.22. Integrated fluorescence vs. absorbance graph for TPPH<sub>2</sub> quantum yield determination.

Following the equation  $\Phi_X = \Phi_{ST} \left( \frac{\text{Grad}_X}{\text{Grad}_{ST}} \right) \left( \frac{\eta_X^2}{\eta_{ST}^2} \right)$ , the quantum yield of DMPH<sub>2</sub>-COOH in

DCM is calculated,  $\Phi_{\text{DMPH}_2\text{-COOH}} = 0.62 \times \left( \frac{3.03 \times 10^8}{2.44 \times 10^8} \right) \times 1 = 0.78$ .

YbTPPTpH as reference:

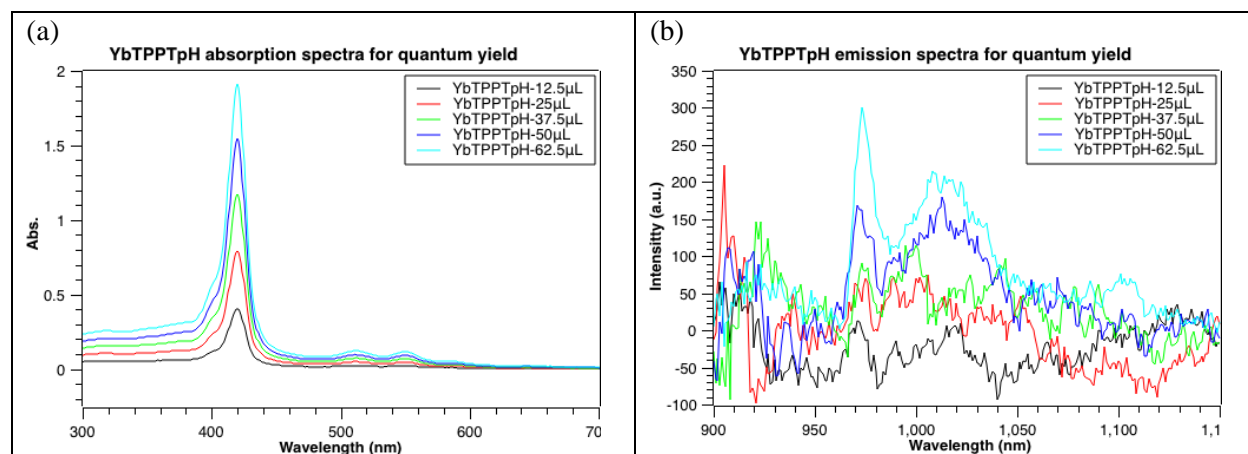


Figure 3.23. Absorption spectra for YbTPPTpH with gradient concentrations (a) and emission spectra for

YbTPPTpH with gradient concentrations ( $\lambda_{\text{ex}} = 556 \text{ nm}$ ) (b) in DCM at room temperature with a stock

solution concentration (YbTPPTpH) of  $2.20 \times 10^{-5} \text{ M}$ .

Table 3.7. Absorbance and integrated fluorescence of YbTPPTpH with gradient concentrations.

	Absorbance at 556 nm	Integration
YbTPPTpH-12.5 $\mu$ L, DCM-2.5 mL	0.0197	-5879.40
YbTPPTpH-25 $\mu$ L, DCM-2.5 mL	0.0410	-476.71
YbTPPTpH-37.5 $\mu$ L, DCM-2.5 mL	0.0615	7648.83
YbTPPTpH-50 $\mu$ L, DCM-2.5 mL	0.0808	11799.30
YbTPPTpH-62.5 $\mu$ L, DCM-2.5 mL	0.1022	19539.80

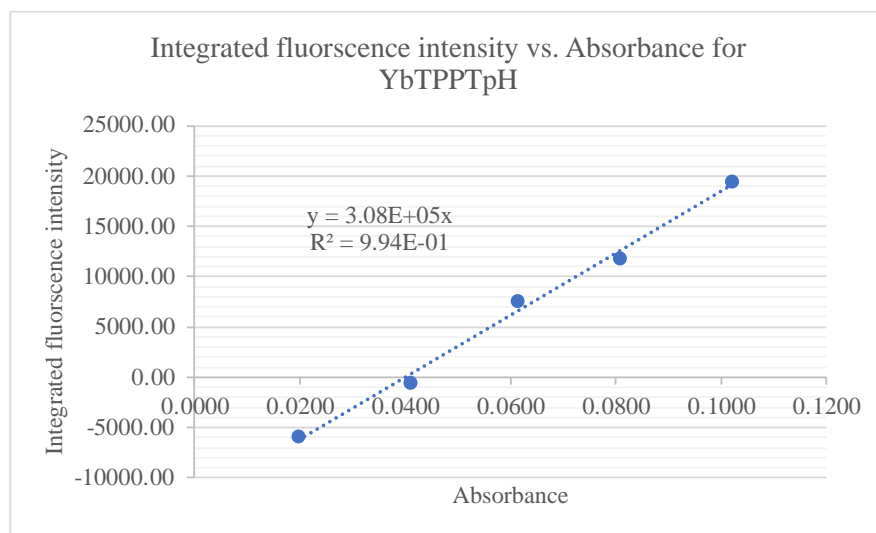


Figure 3.24. Integrated fluorescence vs. absorbance graph for YbTPPTpH quantum yield determination.

YbDMP-BDP complex:

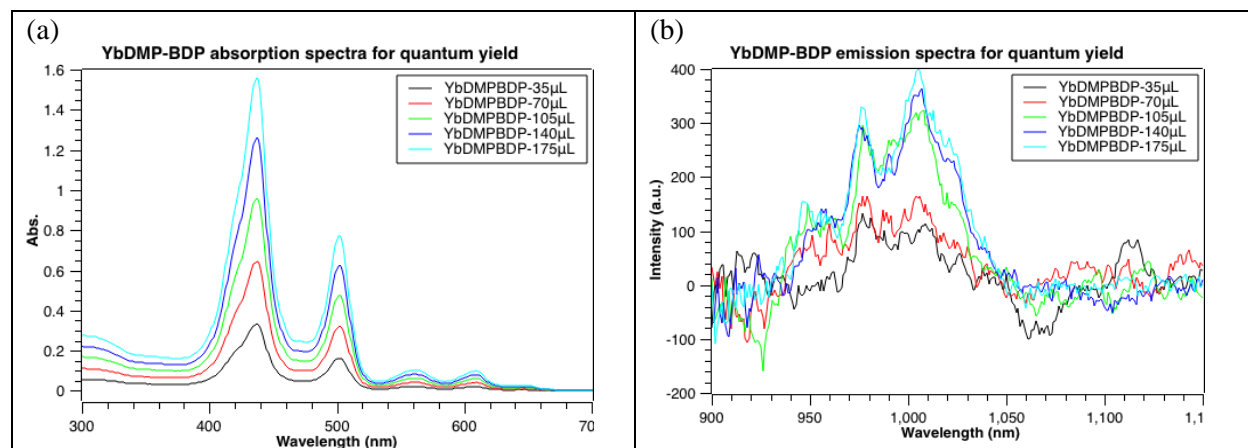


Figure 3.25. Absorption spectra for YbDMP-BDP with gradient concentrations (a) and emission spectra for

YbDMP-BDP with gradient concentrations ( $\lambda_{\text{ex}} = 556 \text{ nm}$ ) (b) in DCM at room temperature with a stock solution concentration (YbDMP-BDP) of  $2.20 \times 10^{-5} \text{ M}$ .

Table 3.8. Absorbance and integrated fluorescence of YbDMP-BDP with gradient concentrations.

	Absorbance at 556 nm	Integration
YbDMPBDP-35 $\mu$ L, DCM-2.5 mL	0.0200	4724.93
YbDMPBDP-70 $\mu$ L, DCM-2.5 mL	0.0397	9280.80
YbDMPBDP-105 $\mu$ L, DCM-2.5 mL	0.0594	14474.70
YbDMPBDP-140 $\mu$ L, DCM-2.5 mL	0.0787	17601.10
YbDMPBDP-175 $\mu$ L, DCM-2.5 mL	0.0977	20456.70

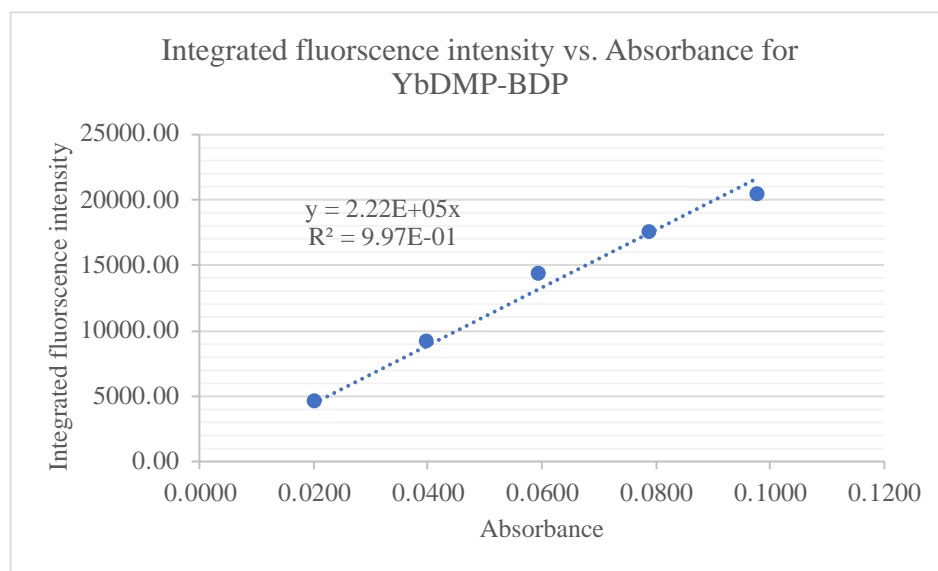


Figure 3.26. Integrated fluorescence vs. absorbance graph for YbDMP-BDP quantum yield determination.

Following the equation  $\Phi_X = \Phi_{ST} \left( \frac{\text{Grad}_X}{\text{Grad}_{ST}} \right) \left( \frac{\eta_X^2}{\eta_{ST}^2} \right)$ , the quantum yield of YbDMP-BDP in DCM is calculated,  $\Phi_{\text{YbDMP-BDP}} = 0.032 \times \left( \frac{2.22 \times 10^5}{3.08 \times 10^5} \right) \times 1 = 0.023$ . Also, the quantum yield of YbDMP-COOH have been calculated and reported as 0.023.<sup>79</sup> Both quantum yields of two complexes are slightly higher than that of YbDMP, which is 0.021.<sup>79</sup>

## Chapter 4 Conclusion

In this research, two ytterbium porphyrin complexes with absorption in far-red region and fluorescence emission in near-infrared region were synthesized. The DMPH<sub>2</sub>-BDP ligand and YbDMP-BDP complex were synthesized by appending the 8-(4-ethynylphenyl)-1,3,5,7-tetramethyl-BODIPY to one *meso*-position of porphyrin. The DMPH<sub>2</sub>-BDP ligand and YbDMP-BDP complex were synthesized by functionized one *meso*-position of porphyrin with 4-ethynylbenzoic acid. Both YbDMP-BDP and Yb-COOH complexes have absorption at 611 nm and 615 nm, respectively, which red-shift to longer wavelength in red region compared to YbDMP complex. The YbDMP-BDP complex has a strong absorption peak centered at 502 nm, which compensates for the weak absorption of YbDMP-COOH in the 480-520 nm region. The two complexes also show intense fluorescence emission in near-infrared region with various excitation wavelengths. With the excitation at 556 nm, the YbDMP-BDP and Yb-COOH both have quantum yield of 0.023. In general, the photophysical characteristics of these two sets of ligands and complexes demonstrate their low energy and safety potential applications in medical diagnostic.

Beside the functionization on one *meso*-position of porphyrin, 5,10,15,20-tetraphenylporpholactone (TPLH<sub>2</sub>) was synthesized by acetylacetonation on one  $\beta$ -position of inner porphyrin ring. The absorption of TPLH<sub>2</sub> ligand in Q-band region is red-shifted upon 645 nm, and TPLH<sub>2</sub> ligand has higher emission intensity in visible region ( $\Phi_{\text{TPLH}_2}=0.89$ ) compared with 5,10,15,20-tetraphenylporphyrin (TPPH<sub>2</sub>). The research of porpholactone ligand provides a new direction for the modification of porphyrin-based chromophores of lanthanide metals.

## References

1. Karasev, M. M.; Stepanenko, O. V.; Rumyantsev, K. A.; Turoverov, K. K.; Verkhusha, V. V., Near-Infrared Fluorescent Proteins and Their Applications. *Biochemistry (Mosc)* **2019**, *84* (Suppl 1), S32-S50.
2. Bünzli, J.-C. G.; Piguet, C., Taking advantage of luminescent lanthanide ions. *Chemical Society Reviews* **2005**, *34* (12), 1048-1077.
3. Eliseeva, S. V.; Bünzli, J.-C. G., Rare earths: jewels for functional materials of the future. *New Journal of Chemistry* **2011**, *35* (6), 1165-1176.
4. Zhang, T.; Chan, C. F.; Lan, R.; Wong, W. K.; Wong, K. L., Highly selective and responsive visible to near-IR ytterbium emissive probe for monitoring mercury(II). *Chemistry* **2014**, *20* (4), 970-3.
5. Zhu, X.; Wong, W.-K.; Wong, W.-Y.; Yang, X., Design and Synthesis of Near-Infrared Emissive Lanthanide Complexes Based on Macrocyclic Ligands. *European Journal of Inorganic Chemistry* **2011**, *2011* (30), 4651-4674.
6. Ke, X.-S.; Yang, B.-Y.; Cheng, X.; Chan, S. L.-F.; Zhang, J.-L., Ytterbium(III) Porpholactones:  $\beta$ -Lactonization of Porphyrin Ligands Enhances Sensitization Efficiency of Lanthanide Near-Infrared Luminescence. *Chemistry – A European Journal* **2014**, *20* (15), 4324-4333.
7. Crossley, M. J.; Burn, P. L., An approach to porphyrin-based molecular wires: synthesis of a bis(porphyrin)tetraone and its conversion to a linearly conjugated tetrakisporphyrin system. *Journal of the Chemical Society, Chemical Communications* **1991**, (21), 1569-1571.
8. Ethirajan, M.; Chen, Y.; Joshi, P.; Pandey, R. K., The role of porphyrin chemistry in tumor imaging and photodynamic therapy. *Chemical Society Reviews* **2011**, *40* (1), 340-362.
9. Borovkov, V., Supramolecular Chirality in Porphyrin Chemistry. *Symmetry* **2014**, *6* (2), 256-294.
10. Sun, B.; Ou, Z.; Yang, S.; Meng, D.; Lu, G.; Fang, Y.; Kadish, K. M., Synthesis and electrochemistry of  $\beta$ -pyrrole nitro-substituted cobalt(II) porphyrins. The effect of the NO<sub>2</sub> group on redox potentials, the electron transfer mechanism and catalytic reduction of molecular oxygen in acidic media. *Dalton Transactions* **2014**, *43* (28), 10809-10815.
11. Yorimitsu, H.; Osuka, A., Organometallic Approaches for Direct Modification of Peripheral C—H Bonds in Porphyrin Cores. *Asian Journal of Organic Chemistry* **2013**, *2* (5), 356-373.
12. Pomogaev, V. A.; Avramov, P. V.; Kuzubov, A. A.; Artyukhov, V. Y., Structure and electronic properties of hollow-caged C<sub>60</sub> fullerene-derived (MN<sub>4</sub>)<sub>n</sub>C<sub>6(10-n)</sub> (M = Zn, Mg, Fe, n = 1–6) complexes. *International Journal of Quantum Chemistry* **2015**, *115* (4), 239-244.
13. Wang, A.; Long, L.; Zhao, W.; Song, Y.; Humphrey, M. G.; Cifuentes, M. P.; Wu, X.; Fu, Y.; Zhang, D.; Li, X.; Zhang, C., Increased optical nonlinearities of graphene nanohybrids covalently functionalized by axially-coordinated porphyrins. *Carbon* **2013**, *53*, 327-338.

14. Angaridis, P. A.; Lazarides, T.; Coutsolelos, A. C., Functionalized porphyrin derivatives for solar energy conversion. *Polyhedron* **2014**, *82*, 19-32.
15. Mink, L. M.; Neitzel, M. L.; Bellomy, L. M.; Falvo, R. E.; Boggess, R. K.; Trainum, B. T.; Yeaman, P., Platinum(II) and platinum(IV) porphyrin complexes: synthesis, characterization, and electrochemistry. *Polyhedron* **1997**, *16* (16), 2809-2817.
16. Rothmund, P., A New Porphyrin Synthesis. The Synthesis of Porphin1. *Journal of the American Chemical Society* **1936**, *58* (4), 625-627.
17. Adler, A. D.; Longo, F. R.; Finarelli, J. D.; Goldmacher, J.; Assour, J.; Korsakoff, L., A simplified synthesis for *meso*-tetraphenylporphine. *The Journal of Organic Chemistry* **1967**, *32* (2), 476.
18. Sun, Z.; She, Y.; Cao, M.; Zhou, Q.; Lu, X.; Zhang, S., Synthesis of substituted *meso*-tetraphenylporphyrins in mixed solvent systems. *ARKIVOC* **2013**, *2013* (3), 389-400.
19. Senge, M. O., Stirring the porphyrin alphabet soup—functionalization reactions for porphyrins. *Chemical Communications* **2011**, *47* (7), 1943-1960.
20. Adler, A. D.; Longo, F. R.; Shergalis, W., Mechanistic Investigations of Porphyrin Syntheses. I. Preliminary Studies on *ms*-Tetraphenylporphin. *Journal of the American Chemical Society* **1964**, *86* (15), 3145-3149.
21. Lindsey, J. S.; Schreiman, I. C.; Hsu, H. C.; Kearney, P. C.; Marguerettaz, A. M., Rothmund and Adler-Longo reactions revisited: synthesis of tetraphenylporphyrins under equilibrium conditions. *The Journal of Organic Chemistry* **1987**, *52* (5), 827-836.
22. Guo, C.-C.; Tong, R.-B.; Li, K.-L., Chloroalkyl piperazine and nitrogen mustard porphyrins: Synthesis and anticancer activity. *Bioorganic & Medicinal Chemistry* **2004**, *12*, 2469-2475.
23. Liu, Q.; Gong, Y.-Z.; Gong, C.-J.; Li, Q.-H.; Guo, C.-C., A new one-pot synthesis of  $\mu$ -oxo dimeric iron(III) porphyrins from *meso*-tetraarylporphyrins. *Journal of Porphyrins and Phthalocyanines* **2009**, *13* (08n09), 854-858.
24. Li, C.; Wang, Q.; Shen, B.; Xiong, Z.; Chen, C., Solubilities of 5,10,15,20-Tetrakis(p-chlorophenyl)porphyrin in Binary Propionic Acid + Water Solvent Mixtures at (293.2 to 353.2) K. *Journal of Chemical & Engineering Data* **2014**, *59* (12), 3953-3959.
25. You, C.-C.; Würthner, F., Self-Assembly of Ferrocene-Functionalized Perylene Bisimide Bridging Ligands with Pt(II) Corner to Electrochemically Active Molecular Squares. *Journal of the American Chemical Society* **2003**, *125* (32), 9716-9725.
26. Taniguchi, S.; Hasegawa, H.; Yanagiya, S.; Tabeta, Y.; Nakano, Y.; Takahashi, M., The first isolation of unsubstituted porphyrinogen and unsubstituted 21-oxaporphyrinogen by the '3+1' approach from 2,5-bis(hydroxymethyl)pyrrole and tripyrrane derivatives. *Tetrahedron* **2001**, *57* (11), 2103-2108.
27. Beyzavi, M. H.; Nietzold, C.; Reissig, H.-U.; Wiehe, A., Synthesis of Functionalized trans-A2B2-Porphyrins Using Donor–Acceptor Cyclopropane-Derived Dipyrromethanes. *Advanced Synthesis & Catalysis* **2013**, *355* (7), 1409-1422.

28. Dogutan, D. K.; Zaidi, S. H.; Thamyongkit, P.; Lindsey, J. S., New route to ABCD-porphyrins via bilanes. *The Journal of Organic Chemistry* **2007**, *72* (20), 7701-7714.
29. Dogutan, D. K.; Lindsey, J. S., Investigation of the Scope of a New Route to ABCD-Bilanes and ABCD-Porphyrins. *The Journal of Organic Chemistry* **2008**, *73* (17), 6728-6742.
30. Koszarna, B.; Gryko, D. T., Efficient Synthesis of *meso*-Substituted Corroles in a H<sub>2</sub>O–MeOH Mixture. *The Journal of Organic Chemistry* **2006**, *71* (10), 3707-3717.
31. Mondal, S.; Pain, T.; Sahu, K.; Kar, S., Large-Scale Green Synthesis of Porphyrins. *ACS Omega* **2021**, *6* (35), 22922-22936.
32. Guo, L.; Yan, B., Near-infrared luminescent hybrid materials using modified functional lanthanide (Nd<sup>3+</sup>, Yb<sup>3+</sup>) porphyrins complexes chemical bonded with silica. *Inorganic Chemistry Communications* **2011**, *14* (11), 1833-1837.
33. Yan, B.; Li, Y.-Y.; Qiao, X.-F., Photofunctional metalloporphyrins functionalized mesoporous hybrids phen-Ln(LSi)-SBA-15 (Ln=Nd, Yb, L=porphyrin derivatives). *Microporous and Mesoporous Materials* **2012**, *158*, 129-136.
34. Eckes, F.; Bulach, V.; Guenet, A.; Strassert, C. A.; Cola, L. D.; Hosseini, M. W., Sensitization of the NIR emission of Nd(III) by the  $\alpha$ 4 atropoisomer of a *meso*-tetraphenyl porphyrin bearing four 8-hydroxyquinolinylamide chelates. *Chemical Communications* **2010**, *46* (4), 619-621.
35. Zhang, T.; Zhu, X.; Cheng, C. C. W.; Kwok, W.-M.; Tam, H.-L.; Hao, J.; Kwong, D. W. J.; Wong, W.-K.; Wong, K.-L., Water-Soluble Mitochondria-Specific Ytterbium Complex with Impressive NIR Emission. *Journal of the American Chemical Society* **2011**, *133* (50), 20120-20122.
36. Zhang, T.; Chan, C.-F.; Hao, J.; Law, G.-L.; Wong, W.-K.; Wong, K.-L., Fast uptake, water-soluble, mitochondria-specific erbium complex for a dual function molecular probe – imaging and photodynamic therapy. *RSC Advances* **2013**, *3* (2), 382-385.
37. Zhang, T.; Chan, C.-F.; Lan, R.; Li, H.; Mak, N.-K.; Wong, W.-K.; Wong, K.-L., Porphyrin-based ytterbium complexes targeting anionic phospholipid membranes as selective biomarkers for cancer cell imaging. *Chemical Communications* **2013**, *49* (65), 7252-7254.
38. Zhang, T.; Lan, R.; Chan, C.-F.; Law, G.-L.; Wong, W.-K.; Wong, K.-L., *In vivo* selective cancer-tracking gadolinium eradicator as new-generation photodynamic therapy agent. *Proceedings of the National Academy of Sciences* **2014**, *111* (51), E5492-E5497.
39. Zhang, X.; Xiao, Y.; Qian, X., A ratiometric fluorescent probe based on FRET for imaging Hg<sup>2+</sup> ions in living cells. *Angewandte Chemie International Edition* **2008**, *47* (42), 8025-9.
40. Hu, J.-Y.; Ning, Y.; Meng, Y.-S.; Zhang, J.; Wu, Z.-Y.; Gao, S.; Zhang, J.-L., Highly near-IR emissive ytterbium(III) complexes with unprecedented quantum yields. *Chemical Science* **2017**, *8* (4), 2702-2709.
41. Doffek, C.; Seitz, M., The Radiative Lifetime in Near-IR-Luminescent Ytterbium Cryptates: The Key to Extremely High Quantum Yields. *Angewandte Chemie International Edition* **2015**, *54* (33), 9719-9721.

42. Ning, Y.; Tang, J.; Liu, Y.-W.; Jing, J.; Sun, Y.; Zhang, J.-L., Highly luminescent, biocompatible ytterbium(III) complexes as near-infrared fluorophores for living cell imaging. *Chemical Science* **2018**, *9* (15), 3742-3753.
43. Ning, Y.; Cheng, S.; Wang, J.-X.; Liu, Y.-W.; Feng, W.; Li, F.; Zhang, J.-L., Fluorescence lifetime imaging of upper gastrointestinal pH *in vivo* with a lanthanide based near-infrared  $\tau$  probe. *Chemical Science* **2019**, *10* (15), 4227-4235.
44. Zhang, T.; Zhu, X.; Wong, W.-K.; Tam, H.-L.; Wong, W.-Y., Light-Harvesting Ytterbium(III)–Porphyrinate–BODIPY Conjugates: Synthesis, Excitation-Energy Transfer, and Two-Photon-Induced Near-Infrared-Emission Studies. *Chemistry – A European Journal* **2013**, *19* (2), 739-748.
45. He, H.; Bosonetta, J. D.; Wheeler, K. A.; May, S. P., Sisters together: co-sensitization of near-infrared emission of ytterbium(III) by BODIPY and porphyrin dyes. *Chemistry Communications* **2017**, *53* (73), 10120-10123.
46. Wang, C.-L.; Hu, J.-Y.; Wu, C.-H.; Kuo, H.-H.; Chang, Y.-C.; Lan, Z.-J.; Wu, H.-P.; Wei-Guang Diao, E.; Lin, C.-Y., Highly efficient porphyrin-sensitized solar cells with enhanced light harvesting ability beyond 800 nm and efficiency exceeding 10%. *Energy & Environmental Science* **2014**, *7* (4), 1392-1396.
47. Cai, H.; Fujimoto, K.; Lim, J. M.; Wang, C.; Huang, W.; Rao, Y.; Zhang, S.; Shi, H.; Yin, B.; Chen, B.; Ma, M.; Song, J.; Kim, D.; Osuka, A., Synthesis of direct  $\beta$ -to- $\beta$  linked porphyrin arrays with large electronic interactions: branched and cyclic oligomers. *Angewandte Chemie International Edition* **2014**, *53* (41), 11088-91.
48. Ke, H.; Ma, W.; Wang, H.; Cheng, G.; Yuan, H.; Wong, W.-K.; Kwong, D. W. J.; Tam, H.-L.; Cheah, K.-W.; Chan, C.-F.; Wong, K.-L., Synthesis, singlet-oxygen photogeneration, two-photon absorption, photo-induced DNA cleavage and cytotoxic properties of an amphiphilic  $\beta$ -Schiff-base linked Ru(II) polypyridyl–porphyrin conjugate. *Journal of Luminescence* **2014**, *154*, 356-361.
49. Ning, Y.; Ke, X.-S.; Hu, J.-Y.; Liu, Y.-W.; Ma, F.; Sun, H.-L.; Zhang, J.-L., Bioinspired Orientation of  $\beta$ -Substituents on Porphyrin Antenna Ligands Switches Ytterbium(III) NIR Emission with Thermosensitivity. *Inorganic Chemistry* **2017**, *56* (4), 1897-1905.
50. Ning, Y.; Liu, Y. W.; Meng, Y. S.; Zhang, J. L., Design of Near-Infrared Luminescent Lanthanide Complexes Sensitive to Environmental Stimulus through Rationally Tuning the Secondary Coordination Sphere. *Inorganic Chemistry* **2018**, *57* (3), 1332-1341.
51. Zhu, M.; Zhang, H.; Ran, G.; Mangel, D. N.; Yao, Y.; Zhang, R.; Tan, J.; Zhang, W.; Song, J.; Sessler, J. L.; Zhang, J.-L., Metal Modulation: An Easy-to-Implement Tactic for Tuning Lanthanide Phototheranostics. *Journal of the American Chemical Society* **2021**, *143* (19), 7541-7552.
52. Maas, H.; Currao, A.; Calzaferri, G., Encapsulated Lanthanides as Luminescent Materials. *Angewandte Chemie International Edition* **2002**, *41*, 2495-7.



53. Ma, Y.; Yang, X.; Niu, M.; Hao, W.; Shi, D.; Schipper, D., High-Nuclearity Cd(II)–Nd(III) Nanowheel with NIR Emission Sensing of Metal Cations and Nitro-Based Explosives. *Crystal Growth & Design* **2021**, *21* (5), 2821-2827.
54. Hayes, A. V.; Drickamer, H. G., High pressure luminescence studies of energy transfer in rare earth chelates. *The Journal of Chemical Physics* **1982**, *76* (1), 114-125.
55. Crosby, G. A.; Whan, R. E.; Freeman, J. J., Spectroscopic Studies of Rare Earth Chelates. *The Journal of Physical Chemistry* **1962**, *66* (12), 2493-2499.
56. Whan, R. E.; Crosby, G. A., Luminescence studies of rare earth complexes: Benzoylacetate and dibenzoylmethide chelates. *Journal of Molecular Spectroscopy* **1962**, *8* (1), 315-327.
57. Shavaleev, N. M.; Scopelliti, R.; Gumy, F.; Bünzli, J.-C. G., Near-Infrared Luminescence of Nine-Coordinate Neodymium Complexes with Benzimidazole-Substituted 8-Hydroxyquinolines. *Inorganic Chemistry* **2008**, *47* (19), 9055-9068.
58. Hebbink, Gerald A.; Reinhoudt, David N.; van Veggel, Frank C. J. M., Increased Luminescent Lifetimes of Ln<sup>3+</sup> Complexes Emitting in the Near-Infrared as a Result of Deuteration. *European Journal of Organic Chemistry* **2001**, *2001* (21), 4101-4106.
59. Glover, P. B.; Bassett, A. P.; Nockemann, P.; Kariuki, B. M.; Van Deun, R.; Pikramenou, Z., Fully Fluorinated Imidodiphosphinate Shells for Visible- and NIR-Emitting Lanthanides: Hitherto Unexpected Effects of Sensitizer Fluorination on Lanthanide Emission Properties. *Chemistry – A European Journal* **2007**, *13* (22), 6308-6320.
60. Romanelli, M.; Kumar, G. A.; Emge, T. J.; Riman, R. E.; Brennan, J. G., Intense Near-IR Emission from Nanoscale Lanthanoid Fluoride Clusters. *Angewandte Chemie International Edition* **2008**, *47* (32), 6049-6051.
61. Williams, A. T. R.; Winfield, S. A.; Miller, J. N., Relative fluorescence quantum yields using a computer-controlled luminescence spectrometer. *Analyst* **1983**, *108* (1290), 1067-1071.
62. Würth, C.; Grabolle, M.; Pauli, J.; Spieles, M.; Resch-Genger, U., Relative and absolute determination of fluorescence quantum yields of transparent samples. *Nature Protocols* **2013**, *8* (8), 1535-1550.
63. Rangasamy, S.; Ju, H.; Um, S.; Oh, D.-C.; Song, J. M., Mitochondria and DNA Targeting of 5,10,15,20-Tetrakis(7-sulfonatobenzo[b]thiophene) Porphyrin-Induced Photodynamic Therapy via Intrinsic and Extrinsic Apoptotic Cell Death. *Journal of Medicinal Chemistry* **2015**, *58* (17), 6864-6874.
64. Que, Y.; Liu, Y.; Tan, W.; Feng, C.; Shi, P.; Li, Y.; Xiaoyu, H., Enhancing Photodynamic Therapy Efficacy by Using Fluorinated Nanoplatfrom. *ACS Macro Letters* **2016**, *5* (2), 168-173.
65. Kan, J.-L.; Jiang, Y.; Xue, A.; Yu, Y.-H.; Wang, Q.; Zhou, Y.; Dong, Y.-B., Surface Decorated Porphyrinic Nanoscale Metal–Organic Framework for Photodynamic Therapy. *Inorganic Chemistry* **2018**, *57* (9), 5420-5428.

66. Jin, C. S.; Lovell, J. F.; Chen, J.; Zheng, G., Ablation of Hypoxic Tumors with Dose-Equivalent Photothermal, but Not Photodynamic, Therapy Using a Nanostructured Porphyrin Assembly. *ACS Nano* **2013**, *7* (3), 2541-2550.
67. Lu, K.; He, C.; Lin, W., Nanoscale Metal–Organic Framework for Highly Effective Photodynamic Therapy of Resistant Head and Neck Cancer. *Journal of the American Chemical Society* **2014**, *136* (48), 16712-16715.
68. Lu, K.; He, C.; Lin, W., A Chlorin-Based Nanoscale Metal–Organic Framework for Photodynamic Therapy of Colon Cancers. *Journal of the American Chemical Society* **2015**, *137* (24), 7600-7603.
69. Han, Y.; Wu, Y.; Lai, W.; Cao, R., Electrocatalytic Water Oxidation by a Water-Soluble Nickel Porphyrin Complex at Neutral pH with Low Overpotential. *Inorganic Chemistry* **2015**, *54* (11), 5604-5613.
70. Liu, Y.; Han, Y.; Zhang, Z.; Zhang, W.; Lai, W.; Wang, Y.; Cao, R., Low overpotential water oxidation at neutral pH catalyzed by a copper(II) porphyrin. *Chemical Science* **2019**, *10* (9), 2613-2622.
71. Zhou, Y.; Xing, Y.-F.; Wen, J.; Ma, H.-B.; Wang, F.-B.; Xia, X.-H., Axial ligands tailoring the ORR activity of cobalt porphyrin. *Science Bulletin* **2019**, *64* (16), 1158-1166.
72. Liu, Y.; Zhou, G.; Zhang, Z.; Lei, H.; Yao, Z.; Li, J.; Lin, J.; Cao, R., Significantly improved electrocatalytic oxygen reduction by an asymmetrical Pacman dinuclear cobalt(II) porphyrin–porphyrin dyad. *Chemical Science* **2020**, *11* (1), 87-96.
73. Yadav, R. K.; Baeg, J.-O.; Oh, G. H.; Park, N.-J.; Kong, K.-j.; Kim, J.; Hwang, D. W.; Biswas, S. K., A Photocatalyst–Enzyme Coupled Artificial Photosynthesis System for Solar Energy in Production of Formic Acid from CO<sub>2</sub>. *Journal of the American Chemical Society* **2012**, *134* (28), 11455-11461.
74. Cheng, M.-J.; Kwon, Y.; Head-Gordon, M.; Bell, A. T., Tailoring Metal-Porphyrin-Like Active Sites on Graphene to Improve the Efficiency and Selectivity of Electrochemical CO<sub>2</sub> Reduction. *The Journal of Physical Chemistry C* **2015**, *119* (37), 21345-21352.
75. Fang, Z.; Wang, L.; Mu, X.; Chen, B.; Xiong, Q.; Wang, W. D.; Ding, J.; Gao, P.; Wu, Y.; Cao, J., Grain Boundary Engineering with Self-Assembled Porphyrin Supramolecules for Highly Efficient Large-Area Perovskite Photovoltaics. *Journal of the American Chemical Society* **2021**, *143* (45), 18989-18996.
76. Chen, E.-X.; Qiu, M.; Zhang, Y.-F.; He, L.; Sun, Y.-Y.; Zheng, H.-L.; Wu, X.; Zhang, J.; Lin, Q., Energy Band Alignment and Redox-active Sites in Metalloporphyrin-Spaced Metal-Catechol Frameworks for Enhanced CO<sub>2</sub> Photoreduction. *Angewandte Chemie International Edition* **2021**, *61* (1), e202111622.
77. Grover, N.; Emandi, G.; Twamley, B.; Khurana, B.; Sol, V.; Senge, M. O., Synthesis and Structure of *meso*-Substituted Dibenzihomoporphyrins. *European Journal of Organic Chemistry* **2020**, *2020* (41), 6489-6496.

78. Foley, T. J.; Harrison, B. S.; Knefely, A. S.; Abboud, K. A.; Reynolds, J. R.; Schanze, K. S.; Boncella, J. M., Facile preparation and photophysics of near-infrared luminescent lanthanide(III) monoporphyrinate complexes. *Inorganic Chemistry* **2003**, *42* (16), 5023-5032.
79. Balasooriya, D.; Liu, B.; He, H.; Sykes, A.; May, P. S., A conjugated porphyrin as a red-light sensitizer for near-infrared emission of ytterbium(III) ion. *New Journal of Chemistry* **2020**, *44* (43), 18756-18762.